Matthias J. Almer, BSc

Time-of-Flight 3D-Camera Performance Modeling

MASTER'S THESIS

to achieve the university degree of
Diplom-Ingenieur

Master's degree programme: Information and Computer Engineering

submitted to

Graz University of Technology

Supervisor

Ass. Prof. Dipl.-Ing. Dr.techn. Christian Steger

Institute for Technical Informatics

Advisor: Ass. Prof. Dipl.-Ing. Dr.techn. Christian Steger
Dipl.-Ing. Dr.techn. Markus Dielacher (Infineon Technologies Austria AG)

Graz, May 2018

Affidavit

I declare that I have authored this thesis independently, that I have not used other than the declared sources/resources, and that I have explicitly indicated all material which has been quoted either literally or by content from the sources used. The text document uploaded to TUGRAZonline is identical to the present master's thesis.

Date

Signature

Kurzfassung

Time-of-Flight (ToF) Three-Dimensional (3-D) imaging hat in den letzten Jahren an Bedeutung gewonnen und ist ein aktuelles Forschungsgebiet der Computer Vision. Neben anderen 3-D imaging Techniken, wie structured light, kann ToF durch Ansätze wie von PMD Technologies AG, einer Hintergrundlichtunterdrückung, punkten. Weiters kann ein Tiefenbild und ein Graubild berechnet werden. Ein Tiefenbild entsteht, indem die Distanz der Kamera innerhalb des Field of Views (FoVs) zu einem Objekt berechnet wird. Die Anwendungen reichen vom Objektscannen bis zur Gestenerkennung sowie Gesichtserkennung inklusive Verifizierung. Die zugehörigen Sensoren unterliegen einer Miniaturisierung, um sie in elektronischen Geräten, wie einem Smartphone, platzsparend unterzubringen. Doch nicht nur die Größe des Chips trägt zur Entwicklung einer neuen Sensorgeneration bei. Eine wesentliche Rolle spielt dabei die Sensorperformance, welche durch internes Sensorrauschen stark beeinträchtigt wird. Als ToF Kamera versteht man den Sensor inklusive Linse und Beleuchtungseinheit. Ohne letztere wäre ein Betrieb nicht möglich. Diese verursacht jedoch eine Abhängigkeit in Bezug auf die Performance.

Diese Masterarbeit konzentriert sich auf die Modellierung eines ToF Kamera Komplettsystems. Mit Verwendung der Programmierumgebung Matlab wird eine numerische Simulation durchgeführt. Eine wesentlicher Ansatz besteht in der Berücksichtigung des optischen Pfades. Dieser stellt die ausgestrahlte optische Leistung der Beleuchtungseinheit auf ein Objekt dar sowie die Reflexion am Objekt und der Einfall der optischen Leistung auf ein Pixel. Das Modell beschränkt sich auf die Auswertung eines einzelnen Center-Pixels, anstatt eine komplette Szene zu modellieren. Ein weiterer Bestandteil ist die Auswirkung des Hintergrundlichtes, welches durch verschiedene Lichtquellen simuliert wird. Die Hintergrundlichtunterdrückung ist in einem eigenen Modul modelliert. Das Hauptaugenmerk liegt jedoch in der Modellierung des internen Sensorverhaltens. Die prägnanten Rauschquellen des Sensors, *read noise* und *photon shot noise* werden berücksichtigt. *Read noise* besteht aus mehreren Rauschquellen. Das Modell kann mit einer Vielzahl an Parametern konfiguriert werden. Es bietet eine grafische Benutzeroberfläche, um Parameter zu konfigurieren, die Art der Berechnung festzulegen und die Ergebnisse zu betrachten. Verifiziert ist das Modell mithilfe einer ToF Kamera von Infineon Technologies AG, welche zusammen mit PMD Technologies AG entwickelt wurde. Es wird ein 4-Phasenalgorithmus verwendet, um drei Simulationsarten zu verifizieren. Diese bestehen aus einer Veränderung der Distanz, Integrationszeit und Beleuchtungsstärke des Hintergrundlichtes. Die Ergebnisse zeigen eine sehr gute Übereinstimmung der Amplitudenwerte und der Kurvenform des Distanzrauschens. Sensor interne Signalauswertungen werden generiert, um Sensoreigenschaften zu untersuchen.

Abstract

Time-of-Flight (ToF) Three-Dimensional (3-D) imaging has gained importance in recent years and is a current field of research in computer vision. Among other 3-D imaging techniques such as structured light, ToF has benefits of its approaches like Suppression of Background Illumination (SBI) from PMD Technologies AG. Furthermore, not only a depth image but also a grey image can be calculated. A depth image results by calculating the distance from the camera within its Field of View (FoV) to the object. The applications range from object scanning to gesture control, face detection and recognition. The associated sensors underlie a miniaturization to place them into electronics, like a smart phone, to save space. Not only does the size of the chip contribute to the development of a new sensor generation, the sensor performance also has an essential role, which is strongly affected by internal sensor noise. A ToF camera consists of the sensor, a lens and an illumination unit. Without the latter, operation is not possible. However, this causes a dependency in terms of performance.

This master thesis focuses on modeling of a complete ToF camera system. Using the programming environment Matlab a numerical simulation is performed. An essential approach is the consideration of the optical path. It represents the radiated optical power of the illumination unit on an object, the reflection from the object and the incidence of optical power on a pixel. The model is limited to the evaluation of a centre pixel instead of modeling a whole scene. Another feature is the effect of the background light which is simulated by different light sources. The SBI is modeled in a separate module. The main focus, however, lies in modeling the internal sensor behavior. The pragmatic noise sources of the sensor, *read noise* and *photon shot noise* are taken into account. Read noise is a collection for several noise sources. The model can be configured with a variety of parameters. It also offers a graphical user interface to configure parameters, determine the type of simulation and visualize results.

The model is verified using a ToF camera from Infineon Technologies, which was developed together with PMD Technologies AG. A 4-phase algorithm is used to verify three different types of simulations. They consist of a variation in distance, integration time and illuminance of the background light. The results show a very good match of the amplitude values and the waveform of the distance noise. Internal sensor evaluations are generated in order to examine sensor performance.

Acknowledgements

I would like to thank my thesis advisor Ass. Prof. Dipl.-Ing. Dr.techn. Christian Steger of the Institute for Technical Informatics at Graz University of Technology. His support and helpful notes increased this work significantly. Especially, I am grateful for the efforts and assistance of Dipl.-Ing. Dr.techn. Markus Dielacher at Infineon Technologies Austria AG who attracted me working on this thesis. The successful completeness of this work would not have been possible without his continuous support. He also steered me in the right direction which I really appreciate.

Furthermore, I would like to thank all my colleagues at Infineon Technologies Austria AG, especially Dipl.-Ing. Krum Beshinski and Dipl.-Ing. Wolfgang Schickbichler.

Heartfelt thanks go to my parents, grandparents and friends, which tirelessly have encouraged and supported me during the process of writing this thesis and throughout my academic studies. Without them, all this would not have been possible.

Thank you.

Graz, May 2018 Matthias Almer

Contents

List of Figures

List of Tables

Chapter 1

Introduction

Three-Dimensional (3-D) imaging is becoming more and more popular nowadays. There are already a lot of applications where 3-D depth sensing is used. Many localization, reorganization and industrial measurement applications are based on the knowledge of 3-D depth data in addition to 2D data [Lua06, p. 1]. Furthermore, it can be used for 3-D object scanning, in car driver monitoring or gesture control. In smartphones, face detection and recognition is currently used.

There are different ways how 3-D measurements are implemented. One is triangulation which special case is called stereo vision which builds on the depth perception of a human being. Here, two image sensors are displaced to each other, like the eyes of a human. Other implementations are interferometry and Time-of-Flight (ToF). Interferometry uses a superposition of two waves, which results in a wave with different amplitude and phase. ToF can be further split into direct and indirect (Continuous Wave (CW)) modulation [Lan06, pp. 9–25]. This thesis concentrates on CW ToF imaging. With a ToF sensor one obtains a depth and amplitude image. Latter is a grey image of the scene, generated only with active illumination. This technique needs to send out an optical signal to obtain depth data. Therefore, it needs an illumination unit that typically acts in the infrared spectrum being invisible for human eyes [RS13, p. 3]. Using infrared illumination, ToF can also be used in dark conditions. As only the illuminated wave length is interesting for the camera the receiving spectrum can be restricted to it. This means ignoring a lot of the sun's light spectrum. An internal circuit, namely Suppression of Background Illumination (SBI), gives a ToF sensor the ability to work in bright conditions [Ska+16, p. 189].

1.1 Motivation

This thesis concentrates on the error sources of a ToF sensor, on its internal behaviour. A model of a CW modulated ToF sensor is implemented. It is parameterizable in order to investigate environmental and sensor related parameter effects. A performance analysis is then possible to measure the depth precision and accuracy of a sensor. It can be used to determine whether a specific performance is possible in certain use cases or not. Current ToF sensors can be validated against their performance with different parameters, so that the changes that have to be made for a next sensor generation to increase efficiency can be detected. That can mean to reduce the amount of optical power so that the sensor needs less energy. Furthermore, this thesis gives information about the physical setup of a ToF sensor. The thesis was done with cooperation between the Institute for Technical Informatics at Graz University of Technology and Infineon Technologies Austria AG, department Contactless and RF Exploration.

1.2 Objectives

The aim of this thesis is to develop a simulation environment for a ToF camera to evaluate performance data like depth precision range and sunlight robustness. Furthermore, it should be examined how the ToF sensor reacts in different environmental conditions. The focus lies on the indirect instead of the direct ToF approach. As the underlying physics of both approaches is similar, the optical path should also apply to direct ToF. Matlab is used for the creation of a model. The verification is done with real ToF data which can be generated via measurement campaigns.

The following tasks should be carried out during this thesis:

- Literature research in the field of ToF 3D imaging and modeling
- Getting familiar with Infineon's ToF cameras
- Modeling of a ToF system with Matlab
- The model should include
    - Parameterizability
    - Optical path including filters and lenses
    - Background light (e.g. sun light)
    - Noise sources of the sensor
    - Analog sensor performance
    - Digital signal processing of raw data
- Evaluation and verification of the model against real data
- Outline of challenges

1.3 Structuring

This thesis is structured in the following way: An introduction to ToF 3D imaging which forms a theoretical basis for this work, is given in Chapter 2. The theoretical research contains the working principle of a ToF sensor and some challenges. The internal behavior of the sensor, the Photonic Mixing Device (PMD), is examined in a detailed way. Furthermore, some characteristics of a PMD image sensor are outlined as well as systematic and statistical error sources shown. Chapter 2 concludes with state-of-the-art topics that relate to this thesis. It builds a basis for the design in Chapter 3. This chapter shows the derivation of necessary modules and functions to get a complete ToF model. The implementation is described in Chapter 4. It shows the used programming and verification environment. Additionally, tables with a specification of the specific functions of the model and their descriptions are shown. Sometimes figures are applied to describe the behavior in a more detailed way. The implemented Graphical User Interface (GUI) is also described. Chapter 5 shows the results of the implemented model and the verification against real data. This thesis is concluded with a summary and future work in Chapter 6.

Chapter 2

Related Work

This chapter outlines literature that forms a basis for this thesis and summarizes scientific papers showing similar solutions for ToF models. To build up sufficient understanding of ToF the introductory Section 2.1 provides an overview of ToF 3D imaging whereby Subsection 2.1.1 describes the functional principle of a ToF sensor.

2.1 Time-of-Flight

In this section, an overview of the working principle of a ToF camera is given. ToF is a technology for 3D imaging. A ToF camera produces images with distance information, so-called *depth images* [Han+13, p. 1].

2.1.1 Functional Overview

For each pixel the distance from the camera to the corresponding point in the scene has to be calculated in order to obtain a depth image. To make this possible, a ToF camera primarily sends out a modulated Infrared (IR) light signal [Lin+10, p. 1318]. Basically, the modulation can be done in two different ways:

- Direct ToF

  The depth is determined by directly measuring the runtime an emitted light pulse needs to be reflected by an object in the scene and gets received afterwards by the ToF camera [Chi+09, p. 10081].

- Indirect ToF with CW modulation

  The modulation of the emitted signal is not pulsed but continuously modulated. Latter does not depend on fast fall and rise times. Therefore there are more kinds of light sources available. In order to determine a depth, the reflected light and a reference signal are used. The phase difference between these two signals is measured, which directly correlates to the depth [Lan06, p. 18]. This thesis will have its focus on CW modulation.

The following explanations are based on the use of CW modulation. An overview of the functional principle can be seen in Figure 2.1. The modulation block generates a periodic electrical square-wave signal both for the IR emitter and the ToF pixels. The ideal shapes would be sine-shaped, however in practice this is not the case. The IR emitter, which can either consist of a Vertical Cavity Surface-Emitting Laser (VCSEL) or a Light Emitting Diode (LED) illumination unit, is driven by the electrical illumination signal to emit an optical signal. In order to control the illumination intensity a the emitted signal's duty cycle can be varied or the current through the illumination unit monitored. Tyhe emitted optical signal is reflected somewhere by an object in the scene and hits phase-delayed on a pixel matrix which is a part of the ToF sensor [Pla+17, p. 1]. Each ToF pixel performs a cross correlation between the reference signal $r(t)$ and the reflected signal $s(t+\tau)$ according to Equation 2.1 where τ represents a phase delay. Typically, the cross correlation function is sampled four times using a different phase delay. This is done by modulating four electrical illumination signals, one after another-with the corresponding phases 0°, 90°, 180° and 270° [Lin+10, p. 1318].

$$c(\tau) = \lim_{T\to\infty} \int_{-T/2}^{T/2} r(t) \cdot s(t+\tau)dt \tag{2.1}$$

Some post processing algorithm uses the output of the ToF pixels, the raw data, and calculates the depth. The principle of the post processing steps to calculate the depth is described below.

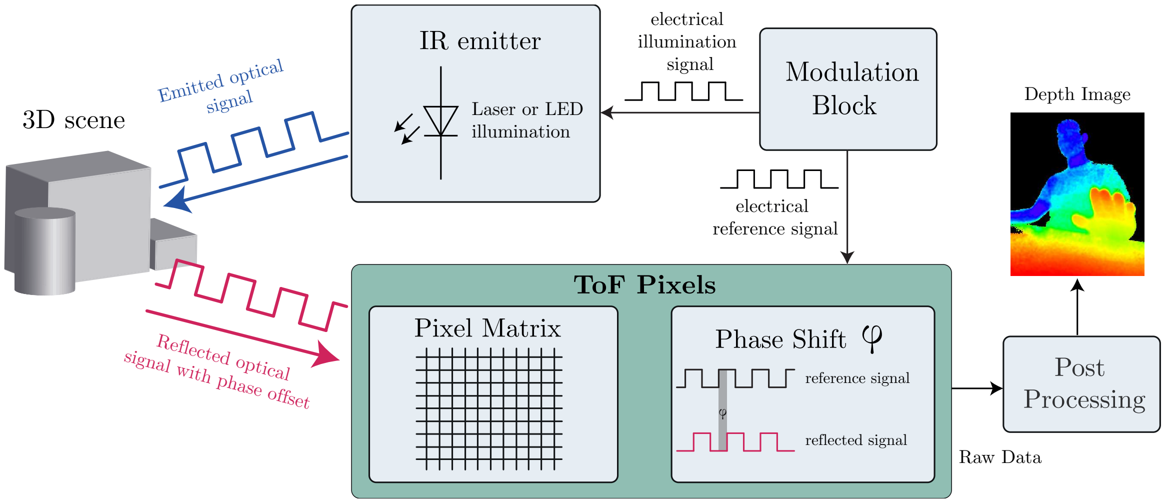

Figure 2.1: Basic functional principle of a ToF imaging system. Obtained with changes from [Dru+15, p. 1432].

2.1.1.1 Depth Calculation

Basically, the depth has to be calculated for each pixel of the ToF sensor to get a depth image. This is why the calculation steps from Equation 2.2 to Equation 2.6 have to be implemented for each pixel.

In Figure 2.2 the principle of a phase shift measurement is sketched as the phase shift is necessary to calculate some depth data. The amplitude of the received square-wave signal is labeled with A, the mean intensity with I. The latter is an offset, which has its origin in the background light of the environment. The amplitude of the sent signal is labeled with E. The periodic time T of the emitted signal is equal to the periodic time of the received signal. In this way they have the same frequency $f = 1/T$ but the phase of the received signal has an offset. The phase shift φ between these two signals is the time difference between the time points of the zero-crossings of the signals [Chi+09, pp. 10081–10083].

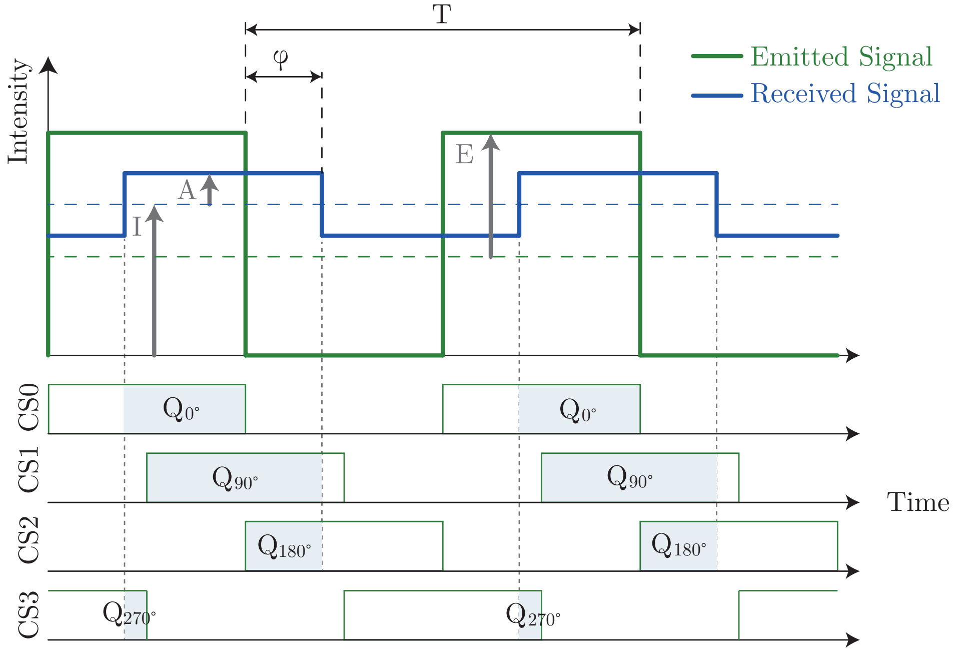

Figure 2.2: Measurement of the phase shift between the emitted and received signal. Obtained with changes from [Chi+09, p. 10082; Han+13, p. 3].

To calculate the phase a so-called *four-bucket* algorithm is commonly used. Four different samples are required to implement this algorithm. The illumination signal is sent out four times with a different phase delay for a specific amount of time which is either called exposure or integration time. The phase delay can be split in a delay which is artificial, for illumination and a delay according to distance. The time is responsible for how long the scene is illuminated by IR light. Basically, it is the time the particular pixels of the sensor are able to collect photons. As a consequence, a long integration time leads to high amplitudes but pixels can saturate when it is too high and then the measurements are wrong [FAT11, p. 1921]. To get a phase-delayed signal the reference signal is shifted with a phase angle of $90^\circ \cdot (i-1)$ where $i \in 1..4$ is the current number of the outgoing signal, the subframe. The sensor internally collects electric charges that are given with Q_1 to Q_4 in Figure 2.2. The detailed explanation of the internal behavior is stated in Section 2.3. CS0 to CS3 are the control signals representing the green emitted signal with the corresponding phase shift [Han+13, pp. 2–3].

With the knowledge of four samples not only the phase shift φ, but also the amplitude A and the mean intensity I can be determined as follows [Lef+13, p. 5]:

$$\varphi = \arctan\left(\frac{Q_{270^\circ} - Q_{90^\circ}}{Q_{0^\circ} - Q_{180^\circ}}\right) \tag{2.2}$$

$$I = \frac{Q_{0^\circ} + Q_{90^\circ} + Q_{180^\circ} + Q_{270^\circ}}{4} \tag{2.3}$$

$$A = \frac{\sqrt{(Q_{270^\circ} - Q_{90^\circ})^2 + (Q_{0^\circ} - Q_{180^\circ})^2}}{2} \tag{2.4}$$

Due to optical losses, like environmental influences or light absorbing surfaces, the amplitude A is smaller than the amplitude of the emitted signal. The amplitude gives information about the Signal-to-Noise Ratio (SNR). The amplitude A can either be used to evaluate the quality of the depth measurement, or to produce an image with gray scales, a so-called amplitude image [Chi+09, p. 10083; Büt+05, p. 3].

As periodic signals are used, the calculated depth will repeat after a certain distance. The unambiguity range d_u is determined by Equation 2.5 using f_{mod} as the modulation frequency and c as the speed of light [FAT11, p. 1918]. The constant factor of 1/2 is needed as the emitted modulated signal travels to an object in the scene and the way back to the camera [Han+13, pp. 2–3; Lef+13, pp. 4–6].

$$d_u = \frac{c}{2 \cdot f_{mod}} \tag{2.5}$$

Finally the distance d can be calculated as given in Equation 2.6 using φ as the calculated phase shift.

$$d = d_u \cdot \frac{\varphi}{2\pi} \tag{2.6}$$

2.2 Range extension

When choosing the modulation frequency, it is important to note that the depth precision and the unambiguity range directly relates to it. This means when using a high modulation frequency the depth precision is high but the unambiguity range is low. In common ToF cameras range extension methods are applied to extend the maximum measureable depth of the unambiguity range. One approach is called dual frequency modulation. Two different modulation frequencies are used which means that the whole capturing of a depth image has to be done twice. When using the 4-bucket algorithm, 8 measurements have to be done. Figure 2.3 illustrates the behavior. In this example the modulation frequencies f_a = 80 MHz and f_b = 60 MHz are chosen. The higher frequency f_a has a unambiguity range of 1.875 m and the low frequency of 2.5 m. The unambiguity range equals 360° when speaking of phases. The object to capture is at a

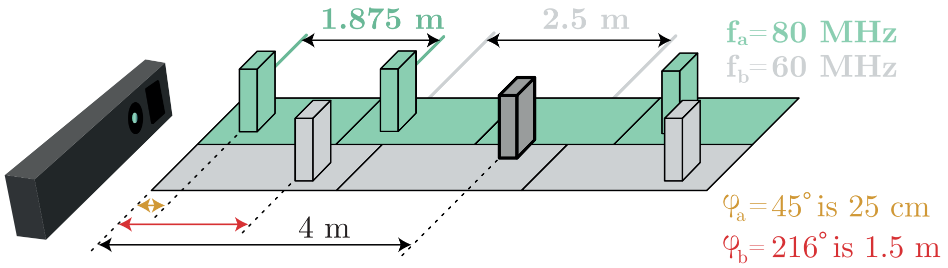

Figure 2.3: On the left a pico flexx ToF camera is shown. The green areas show the unambiguity range of 80 MHz, the blue ones of 60 MHz modulation frequencies. Obtained with changes from [Jon+12, p. 27; Jon+10, p. 1578; 18b; Pay+09, p. 142].

real distance range of 4 meters. This means that the high frequency measures the object at 45° or 25 centimeters while the object pops up at 216° or 1.5 meters using the low frequency. The distance where the two measurements are in agreement lead to the real object distance [Jon+12, pp. 26–27; Jon+10, pp. 1576–1578]. Equation 2.7 shows the extended unambiguity range resulting from the two chosen frequencies and the speed of light [Jon+10, p. 1578].

$$d_u = \frac{c}{2} \cdot \frac{1}{|f_{modHigh} - f_{modLow}|} \tag{2.7}$$

However, when looking back at Section 2.1.1, especially Equation 2.2 to Equation 2.4 for the two frequencies three unknowns are determined, the amplitude, the offset and the phase shift. The approach of using two frequencies is not very efficient as the offset is measured twice and only five variables are gathered with eight phase images [Pay+09, p. 142].

Another approach to solve the unambiguity problem is the usage of several frequencies which are measured simultaneously. This can be achieved by a superposition of two different frequencies. The step size of the phase for the two frequencies has to be different. The DC component can be gathered using a discrete fourier transformation and the phase shift and amplitude can also be determined as they fall into different frequency regions for the two frequencies. A five-phase measurement setup can be used for example, resulting in a reduction in readout time and illumination power. Another benefit to the standard 4-bucket algorithm is the usage of capturing five phase images, resulting in a higher amplitude and therefore better precision [Pay+09, pp. 142–143].

2.3 Photonic mixing device

The PMD is the core part of the ToF sensor. It is a photo detector and opto-electronic mixer simultaneously. The functional principle is explained with Figure 2.4.

With the photo detector light energy, or more precisely photons are converted into electron-hole pairs. In the figure light energy is labeled with P_{opt}, which is electromagnetic radiation compounded of different wavelengths. The internal photoelectric effect which was detected in 1905 by Albert Einstein, shows that electrons could be excited when photons hit a metal [Bas+94, p. 16.2]. Figure 2.4(b) shows the equivalent electrical symbol which consists of two reversed photo diodes sharing the same light receiving area. The outer connections are outputs.

The second mechanism that a PMD handles is the opto-electronic mixing. It mixes an externally applied push-pull modulated signal which refers to *Mod-A* and *Mod-B* respectively, with the photo current (photo carriers). The modulation signals are Mod-A $= U_0 + u_m(t)$ and Mod-B $= U_0 - u_m(t)$ where U_0 is a constant voltage and $u_m(t)$ a modulated one. Generated charge carriers which are in the depletion region are either transported to the left or right side dependent on the sign of the modulation voltage $u_m(t)$ [Zha06, pp. 42, 43]. The behavior is shown with a black and a gray arrow in the figure. This causes a current flow of Read-A / Read-B. The illustrated PMD has a 2-tap pixel architecture. The benefit in comparison to a 1-tap (which per pixel has only one storage for electric charges) is that all generated electrons are dumped and half of the duration for sampling is required [Kau+04]. The illustration 2.4(a) shows that

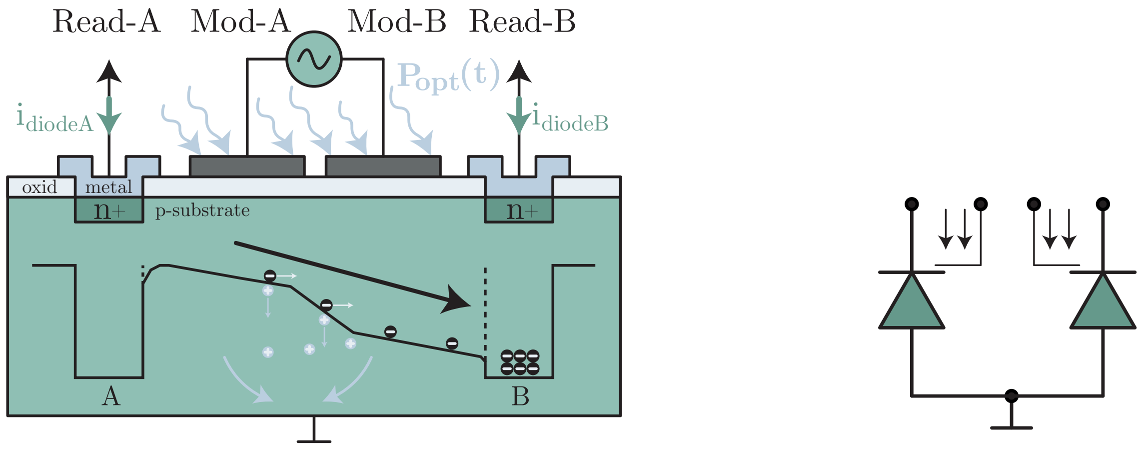

(a)

(b)

Figure 2.4: (a) Profile and functional principle of a 2-tap PMD. Obtained with changes from [Alb07, p. 9; Kra07, p. 17; Zha06, p. 53; Bux+12, p. 193]. The electrical symbol is shown in (b). Obtained with changes from [Lua06, p. 23; Zha06, p. 53].

there is a drift of electrons in the direction of A or B resulting in a current flow i_{diodeA} / i_{diodeB}. The electric charges are then stored in a capacitor to convert a current into a voltage [Zha06, p. 43]. Figure 2.5(a) shows the 4-transistor pixel architecture having the current i_{diodeA} as input. The same schematic is needed for i_{diodeB}.

The typical behavior of a 4-transistor pixel can be divided into three major phases which is explained with Figure 2.5:

1. **Reset Phase**
   Hold and reset transistor are closed here. The capacitor $C_{integration}$ is charged to the voltage V_{reset} and therefore the output voltage is also V_{reset} to get an initial voltage level before starting to integrate [Cho17, pp. 16, 21].

2. **Illumination/Exposure Phase**
   In this phase the reset transistor disconnects $C_{integration}$ from the reset voltage V_{reset}. A photocurrent is generated due to the incoming light and the capacitor gets discharged [Cho17, p. 21]. A negative integration of the output voltage can be seen in Figure 2.5(b). With increasing illumination intensity the negative integration slope is also increasing. When the illumination is too high the capacitor is discharged until $V_{saturated}$. At this voltage level one speaks of saturation.

3. **Readout Phase**
   The readout or hold phase is the last phase in which the hold transistor is opened and no current is flowing. A source follower acts as buffer. When closing the select transistor, which is a row select, the current voltage of the capacitor is output to an Analog Digital Converter (ADC) and sampled [Jai16, p. 15]. The voltage level in the capacitor is held until the next reset phase which is only once at the beginning of the integration time.

The discussed behavior is performed for both taps A and B of the PMD. Figure 2.6(a) gives a more detailed view on the integration of tap A and B. The modulation

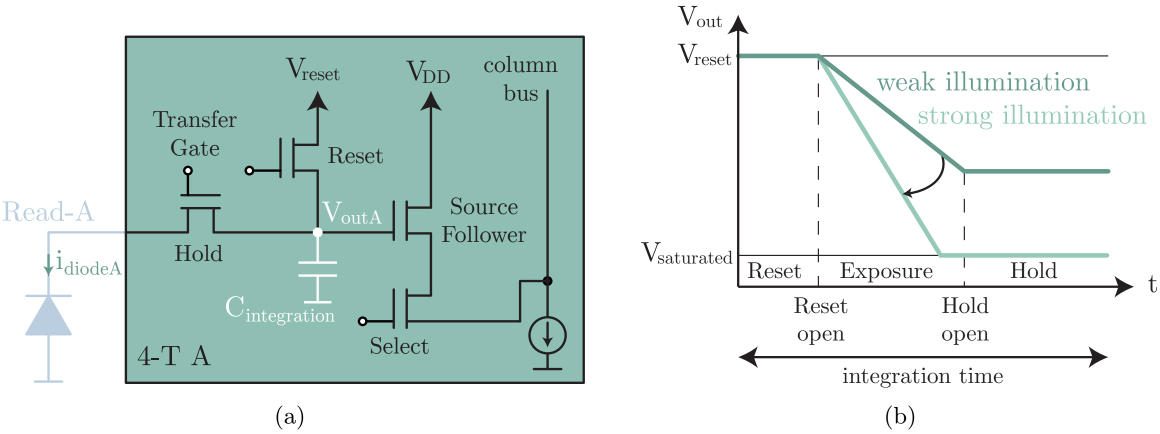

Figure 2.5: (a) 4-transistor pixel architecture for one half of the PMD. The connection Read-A relates to Figure 2.4(b). Obtained with changes from [Ill+15, p. 354; Dec+98, p. 2081; Jai16, p. 15]. The corresponding voltage levels are shown in (b). Obtained with changes from [Tem+06, p. 118; Chi10].

signal is constant and responsible for the distribution of electrons in A and B. It is simplified to be high when generated electrons of the received signal $r(t)$ move to A and low when there are electrons available, drift to B. When the received signal is totally in phase with the modulation signal all electrons are moved to one side. When having a phase shift of 90° between the two signals the charges are equally distributed [Alb07, p. 9]. Received constant light is separated equally in A and B [Lin10, p. 10], which is background light. The figure shows a small snippet of the whole integration process visible in Figure 2.5(b) but without the hold phase and having a phase offset of φ. The pixel information lies in the difference of the two voltages of V_A and V_B.

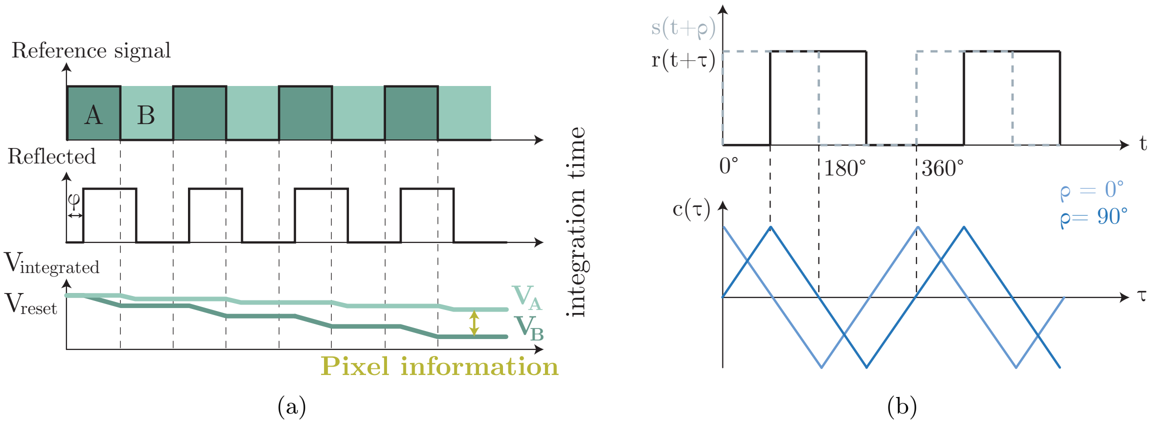

Figure 2.6: Negative integration inside a PMD (a). Obtained with changes from [Cho17, p. 82; Lin10, p. 11]. Cross correlation curves for 0° and 90° phase shift. (b) Obtained with changes from [Zha06, p. 51; Kra07, p. 22].

The final correlation between sent and received signal is shown in Figure 2.6(b). $s(t+\rho)$ represents the sent signal with an offset of ρ. It is only drawn once with 0°

offset and $r(t+\tau)$ is the received signal. One receives the correlation curve in blue when holding the sent signal constant and varying the received signal in τ starting at 0°. For $\tau = 0°$ the maximum of the light blue curve is where both are in phase. According to [Lin10, p. 10] the correlation function is mostly sampled four times in PMD cameras which means two additional curves to apply in Figure 2.6(b), for 180° and 270°. The result of the cross correlation is represented by the voltage level in the integration capacitor which gives four voltages for each phase. The four voltages are then put into Equation 2.2 instead of using charge carriers to calculate depth data.

2.3.1 Suppression of Background Illumination

In a ToF image sensor with PMD technology typically there exist a circuit internally to suppress background illumination to a certain extent. With background illumination unmodulated IR light is meant, resulting in a common mode in both channels A and B, which can lead to pixel saturation. There are also other sources leading to such a behavior like surfaces with a huge reflectivity or long integration times. For the latter, there already exists an automatic setting for the integration time to avoid such phenomena [HA11].

Figure 2.7 shows how background light suppression works. The integration capacitors are here illustrated to be located outside the 2-tap PMD. The symmetric structure is a fundamental prerequisite to obtain working background illumination suppression. Charges that have their origin in unmodulated light are distributed equally in A and B. This effect is known as common mode and can lead to saturation of the integration capacitors. There are two identical current sources controlled by the same voltage which are responsible for the compensation of the common mode. The voltage levels at the integration capacitors are monitored during the integration process. With these two voltage levels V_{outA} and V_{outB} the correlation current is calculated having the direction from the diode to the specific capacitor. To compensate the lower correlation current, a current is fed into the circuit via the current sources that is directed against it. This

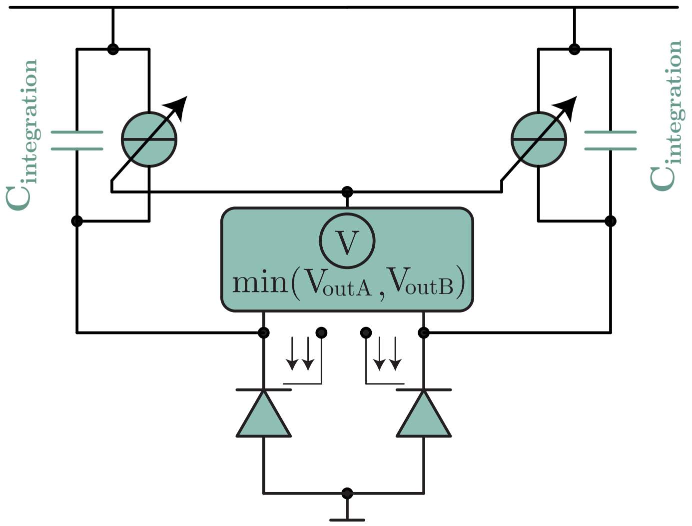

Figure 2.7: Circuit of SBI that is connected to the 2-tap PMD. Obtained with changes from [Sch05, p. 40]

leads to a removal of the common mode of the background light [Sch05, p. 40; Zan+16, pp. 102–103].

2.3.2 Characteristics of a Photonic mixing device image sensor

In this section parameters that have a fundamental impact on the design and behavior of a PMD image sensor are outlined.

2.3.2.1 Fill factor

Looking at one PMD pixel the whole pixel area can be divided into a light sensitive area and an area where the readout electronics like the transistors are located. The fill factor is described as the ratio of light sensitive area divided by the whole pixel area. A value between 30% to 100% is common. A way of having a large fill factor is to have a shared readout logic (the transistors) between pixels. Another way is to put the light sensitive area on the backside of the chip known as backside illumination. Here, circuits on the front-side of the chip do not influence the fill factor. A third solution to increase the fill factor can be to use microlenses as illustrated in Figure 2.8(a). For each pixel a microlens is positioned on the surface of the pixel itself, focusing incoming light to the light sensitive area. With their use a fill factor of about 70% can be achieved [Bat+10, p. 11; Cho17, p. 26].

2.3.2.2 Quantum Efficiency

Equation 2.8 [JHG99, p. 119] denotes the quantum efficiency. The number of generated electron-hole pair's n_0 is divided by the number of all photons hitting the light sensitive area of a pixel (the detector). The ratio is always below 1 where 1 means that all photons generate an electron-hole pair. Effects like scattering and reflectance, relating to a loss in photons, cause quantum efficiency to decrease [JHG99, pp. 119–120; 87h]. Another limitation that leads to smaller quantum efficiency is that not all generated electron-hole pairs are collected. The reason is that photons with a larger wavelength cause a generation of electron-hole pairs deep inside the PMD, outside the depletion region [Jai16, p. 23], see Figure 2.8(c). A typical behavior of quantum efficiency of photo diodes depended on the wavelength λ that is shown for two different materials in Figure 2.8(b).

$$\eta(\lambda) = \frac{n_0}{n_p} \tag{2.8}$$

2.3.2.3 Spectral responsivity

A PMD can be characterized to be a detector which converts optical power into an electrical signal. The relation between electrical output Y and incoming optical power X is defined as spectral responsivity. The incoming optical power can be written as P_{opt} while the electrical output is the resulting photo current i_{photo} as in Equation 2.9. [HBG14, p. 337; Alb07, pp. 52, 53; Zha06, p. 9].

$$S(\lambda) = R_s(\lambda)\ \left[\frac{A}{W}\right] = \frac{Y}{X} = \frac{i_{photo}(\lambda)}{P_{opt}(\lambda)} \tag{2.9}$$

There exists a relation between quantum efficiency and spectral responsivity that can be combined with the given Equation 2.10 [HBG14, p. 343; Zha06, p. 9].

$$R_s(\lambda) = \eta(\lambda) \cdot \frac{e \cdot \lambda}{h \cdot c} \tag{2.10}$$

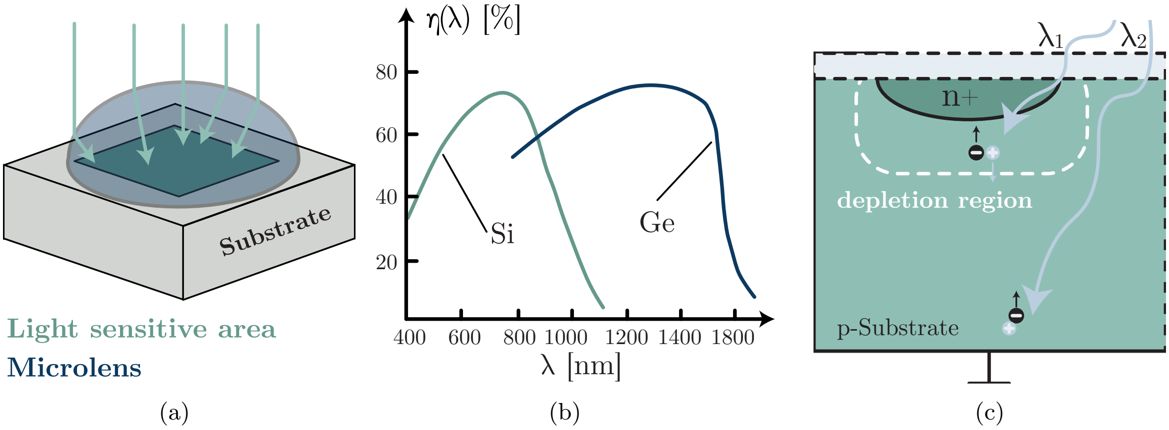

(a) (b) (c)

Figure 2.8: Increased fill factor of one pixel with the use of a micro lens (a). Obtained with changes from [17b]. Behavior of quantum efficiency $\eta(\lambda)$ of photo diodes (b) showing two different materials. Obtained with changes from [HBG14, p. 343]. (c) Absorption of radiation with different wavelengths $\lambda_1 < \lambda_2$. Obtained with changes from [Jai16, p. 22; Cho17, p. 15; HBG14, p. 342].

2.3.2.4 Demodulation Contrast

As already discussed the principle of a PMD relies on the separation of generated charges according to the modulation signals. The characteristic that charges are separated phase correct is named demodulation contrast K. The contrast is given as a percentage where for instance 40% means that 40% of the generated charges are separated to A and B according to their phase and 60% of them are separated equally [Kra07, pp. 22–23]. Therefore the demodulation contrast is a value to describe the efficiency of the mixing process [Alb07, p. 61].

$$K = \frac{U_{max} - U_{min}}{U_{max} + U_{min}} \tag{2.11}$$

2.4 Error sources

For this thesis the error sources of a ToF camera are essential for the creation of a model. That is why systematic and non-systematic errors are introduced in this section. The latter are called statistical errors, further on as they relate to noise.

2.4.1 Systematic errors

When the reconstruction formulas do not cover all properties of a real ToF imager systematic errors appear [Grz+13, p. 7]. In the following a set of selected systematic errors are outlined.

2.4.1.1 Wiggling

A fundamental and well-understood systematic error is the wiggling error or also called circular error. As described in Section 2.3 the cross correlation function is commonly sampled four times having an equidistant phase distance to each other to obtain depth information. In real life applications the assumption that the illumination signal is sinusoidal shaped is not true. The signal shape depends on the illumination source like an LED or VCSEL. The illumination signal has harmonics with a high order, which lead to an oscillating error in the measured depth around the expectation value of the depth [Lin+10, pp. 1319, 1320; Grz+13, p. 7]. The error usually has the form of a sine [FAT11, pp. 1919–1920] shown in Figure 2.10.

Correction There are various ways to counter the error like saving the depth error data in a Look-up Table (LUT) or using B-splines [FAT11, p. 1920].

Streeter and Dorrington provide a way to correct, respectively cancel out a harmonic error [SD15], which leads to a reduction in the wiggling error.

Another approach is presented by Lindner, Kolb, and Ringbeck, who introduced a new demodulation approach. The approach of a reference signal with a rectangular shape is combined with a sinusoidal shaped one [LKR08].

Besides these correction mechanisms one can switch from 4-phase measurements to 3 phase measurements. Using an odd number of phases leads to an decrease in the wiggling error's magnitude [Grü13; Fre13, p. 10].

2.4.1.2 Amplitude related error

The amplitude related error is also called intensity related error [Grü13, p. 2]. It is a systematic error that depends on the amount of light hitting the sensor in total. The ToF camera emits light, which hits an object.

The amount of light hitting an object can be divided into three major categories: Reflection, absorption and transmission. For specific materials the amounts depend on the wavelength of the light source. A completely black surface absorbs the amount of hitting light while a white surface does not absorb but reflects the amount of light. This holds for IR radiation with wavelengths within 800 nm to 800 μm [Kas08, pp. 259–261].

Typically a checkerboard pattern (black / white) is used to show the presence of this error as some parts reflect better than others. The measured depth appears to be nearer to the ToF sensor than it really is when the object has a low reflectivity [Grz+13, p. 8], like a black surface. Figure 2.9 shows the explained behavior. On the other side pixels can saturate due to a high reflective object like glasses [Ebe12, p. 14].

The source of this error cannot completely be explained yet, May et al. states that it is caused by pixel's electronic non-linearities [May+09, p. 939]. These non-linearities should appear in the read out phase of the sensor [Für+16, p. 29]. Multi path problems like reflections that occur in the ToF sensor can be another cause [Grz+13, p. 8]. A countermeasure to this error is a calibration process [Lin10, pp. 16, 44–52].

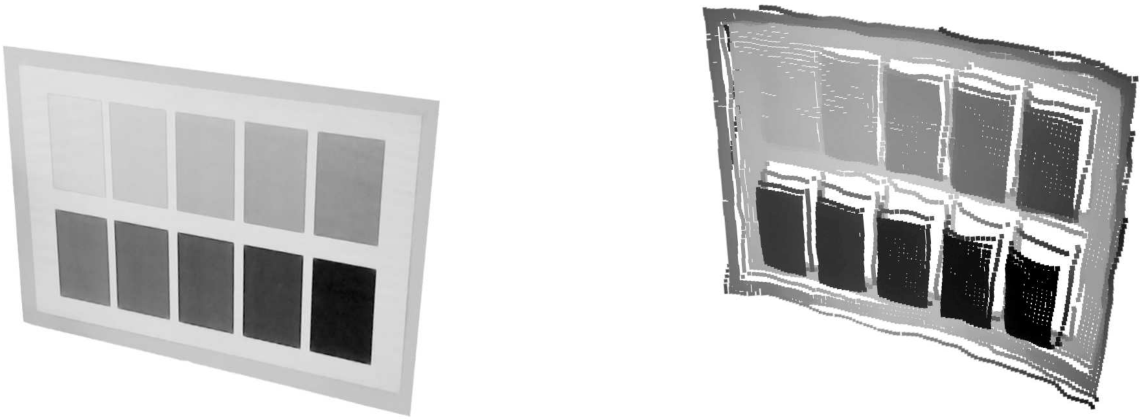

(a) (b)

Figure 2.9: The pattern of a test object having bars from light grey to black is illustrated in (a). The depth image can be seen in (b). Here, lighter colors reflect better than darker ones. Latter seem to be nearer to the ToF camera. Both images obtained from [Lin10, p. 17].

2.4.1.3 Integration time related error

The integration time is the time span where on the one hand a scene is illuminated with light and on the other hand a number of photons hit the light-sensitive part of a ToF camera. Using photon detection depth images are calculated [Für+16, p. 28]. The SNR can be improved by increasing the integration time. However, the measured depth has an offset applied which relates to the integration time [Grü13, p. 8]. In Figure 2.10 the depth error is plotted over real depth for various integration times. It shows a constant offset. The relation between offset and integration time is non-linear [Rap07, p. 47].

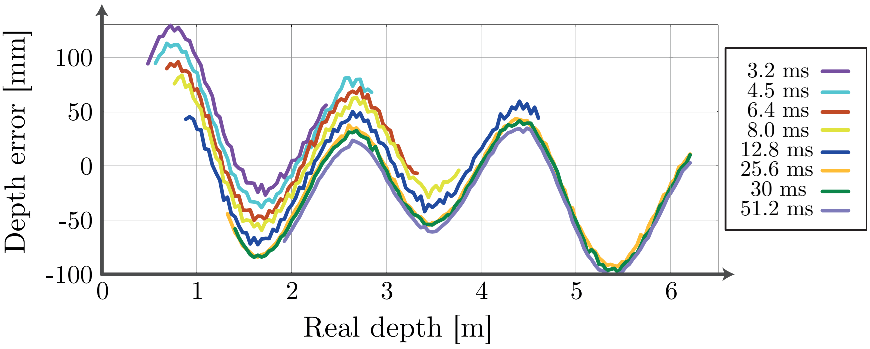

Figure 2.10: The depth error over the real depth of the ToF sensor SwissRanger SR-3000. Each curve represents a different integration time. Obtained with changes from [Rap07, p. 47].

2.4.1.4 Temperature related error

First of all, the temperature effects have to be split up into internal and external temperature effect. The first one relates to the sensor's internal heating where the camera's characteristics change. The increase in temperature is because of the current consumption of the illumination unit and the heating up of the sensor while processing. Warm up effects can be compensated [KRI06, p. 138; Für+16, p. 28].

The external temperature effect belongs to the ambient temperature. Kahlmann, Remondino, and Ingensand provided a measurement of the SwissRanger ToF camera, where the measured depth varies about 8 mm per °C. The effect can be removed in the calibration process [KRI06, p. 138].

2.4.1.5 Fixed pattern noise

Fixed Pattern Noise (FPN) is a disturbance in the measured picture which stays constant for fixed environmental conditions. As it is not a real noise source it then relates to a statistical error. It can be differentiated between pixel individual FPN which is additive and a pixel response non-uniformity having a multiplicative characteristic [Alb07, p. 124].

FPN is caused by a ToF device's implementation of the hardware modules like amplifiers and signal generators. Furthermore, effects like shading and vignetting count to this error source. The name comes from the fact that the error behaves constant but distributes over all pixels which is recognized as a pattern. When analyzing a grey image of a camera FPN can usually be seen either row-wise or column-wise, where the columns or rows vary in the brightness to each other [GBG16, p. 811; Jan07, pp. 30–33].

2.4.2 Statistical errors

Before noise sources can be discussed some statistic basics have to be introduced.

In the context of noise, random noise is meant which is uncontrollable by definition. It means that the full characterization of a noise source is not specified in a precise way either because the precision is not essential or having lack of knowledge. As a consequence, statistics should be used to describe such noise sources. A random variable is used to model noise samples which is described by its Probability Density Function (PDF) [vExt, p. 9; Tia00, pp. 10–13].

The function f(x) is the PDF of the random variable X in Equation 2.12. When integrating between ±∞ the result of the PDF is equal to 1, the complete area between the PDF and the x-axis [Fah+16, pp. 253–254].

$$P(a \leqslant X \leqslant b) = \int_a^b f(x)dx \tag{2.12}$$

For noise analysis important values that can be calculated with the use of the PDF are the mean, Equation 2.13 and variance, Equation 2.14 [Fah+16, p. 267].

$$\mu = E(X) = \int_{-\infty}^{\infty} x \cdot f(x)dx \tag{2.13}$$

$$\sigma^2 = Var(X) = \int_{-\infty}^{\infty} (x-\mu)^2 \cdot f(x)dx \tag{2.14}$$

The standard deviation, Equation 2.16 can then be derived from the variance [Fah+16, p. 267]. It is a value that states how much the signal varies from the mean and can be used to represent noise. When this applies, the quotient of mean and standard deviation gives the signal to noise ratio [Smi97, pp. 14, 17]. A set of independent noise sources must be summed up quadratically to get the total noise [Alb07, p. 16], Equation 2.15. The power of the individual noise sources must be used instead of the amplitude [Smi97, p. 14].

$$\sigma_{total} = \sqrt{\sum_{i=1}^{N} \sigma_i^2} \tag{2.15}$$

$$\sigma = \sqrt{Var(X)} \tag{2.16}$$

Noise power is often estimated using the variance. For the random variable itself a Gaussian is commonly used [Tia00, p. 11]. The formula can be seen in Equation [Fah+16, p. 272]. It is either called Gaussian or normal distribution. Figure 2.11 shows the distribution function.

$$f(x) = \frac{1}{\sqrt{2\cdot\pi}\cdot\sigma} \cdot e^{-\frac{(x-\mu)^2}{2\cdot\sigma^2}} \qquad x \in \mathbb{R} \tag{2.17}$$

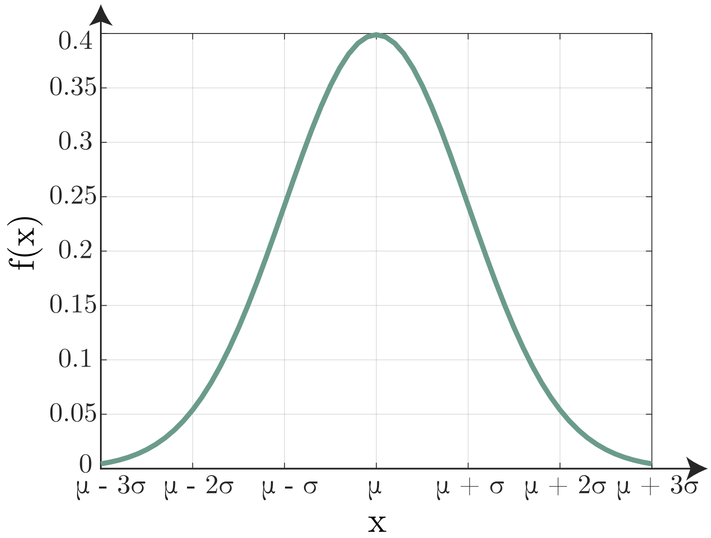

Figure 2.11: The Gaussian distribution function with a mean of $\mu = 0$ and variance $\sigma^2 = 1$.

From the gaussian distribution function the following distribution can be derived: 68% of the observations lie in the interval $\mu \pm \sigma$, 95% in $\mu \pm 2\sigma$ and 99.7% in $\mu \pm 3\sigma$ [Fah+16, p. 86]. When calculating the standard deviation to get a noise value, in relation to the mean, 68% of observations are covered.

2.4.2.1 Thermal noise

A fundamental noise source in electronic devices is thermal noise, also called Johnson noise referring to the discoverer. It is white noise and originates from Brownian motion where free electrons in a conductor move randomly dependent on the temperature. The random movement is equally likely in all directions. Examples where thermal noise appears are resistors and transistors. A Gaussian PDF can be used to model thermal noise having a mean of zero. The effective noise voltage V_N is given in Equation 2.18 understanding R as resistance, the temperature T, the Boltzmann constant k and Δf as the bandwidth [ZZN15, pp. 2–3; Tia00, p. 17; Ett05, p. 130; vExt, pp. 21–23; Cal05, pp. 23–24; Vas08, pp. 41–42].

$$V_{N,thermal}{}^2 = \sigma_{thermal}^2 = 4 \cdot k \cdot T \cdot R \cdot \Delta f \tag{2.18}$$

Having $P = \frac{U^2}{R}$ the noise power evaluates at impedance matching to [ZZN15, pp. 2–3]:

$$P_{N,thermal} = k \cdot T \cdot \Delta f = \frac{V_{N,thermal}{}^2}{2 \cdot R} \frac{1}{2} \tag{2.19}$$

2.4.2.2 Reset noise

Reset noise is explained with Figure 2.13. It shows a part of the 4-transistor circuit of Figure 2.5(a) where the reset transistor works as a switch. When the switch is closed the capacitor is charged via the resistor towards the reset voltage V_{reset}. But as the transistor causes thermal noise the voltage V_C will fluctuate around the reset voltage. Opening the switch establishes a constant voltage value that is the reset voltage applied with thermal noise. Equation 2.18 is the starting point of the reset noise deviation. The bandwidth of the RC network which builds a low pass filter is explained with Figure 2.12, which shows its transfer curve. The cut-off frequency is the frequency where the response characteristics of the low pass filter is attenuated by 3 dB. Noise is not really cut off at this frequency and that is why an equivalent noise bandwidth is important. The area of an ideal filter (black dotted line) with its corresponding bandwidth of f_{enb} has the same area as the green curve of the real filter [Vas05, pp. 80–81]. The equivalent noise bandwidth f_{enb} is used as Δf. It is stated in Equation 2.20 according to [Vas05, pp. 80–81] including the cut-off frequency f_c [Ber08, p. 196]. The final reset noise is formulated in Equation 2.22 [Ana+10, p. 2163] from which the synonym kTC noise originates.

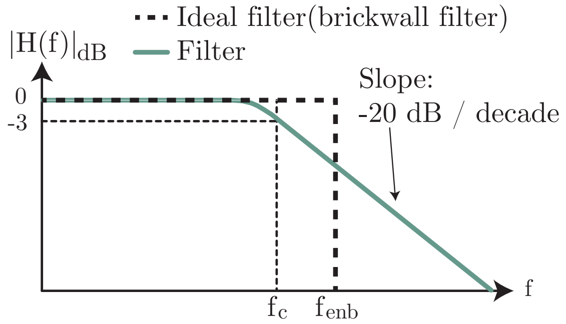

Figure 2.12: Transfer curve of a low pass filter. Obtained with changes from [Bur05].

$$f_{enb} = \frac{\pi}{2} \cdot f_c \qquad \text{with } f_c = \frac{1}{2\pi RC} \tag{2.20}$$

$$\sigma_{reset}^2 = 4 \cdot k \cdot T \cdot R \cdot f_{enb} = \cancel{4} \cdot k \cdot T \cdot \cancel{R} \cdot \frac{\cancel{\pi}}{\cancel{2}} \cdot \frac{1}{\cancel{2\pi R}C} = \frac{kT}{C} \tag{2.21}$$

$$\sigma_{reset}\ [V] = \sqrt{\frac{k \cdot T}{C}} \tag{2.22}$$

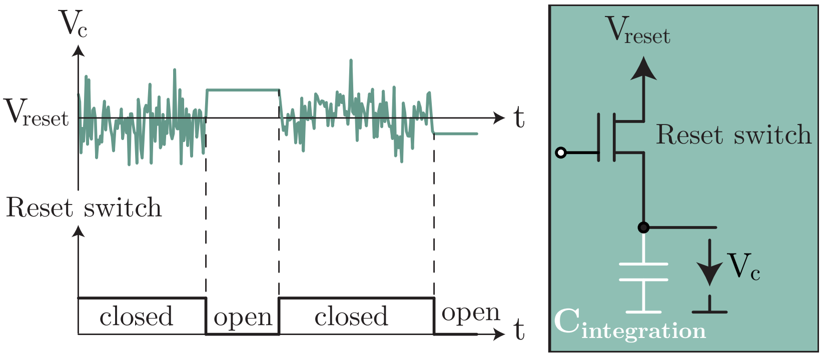

Figure 2.13: Reset noise in a transistor / capacitor network (here low pass filter) letting the transistor work as a switch.

2.4.2.3 Photon shot noise

A ToF sensor is a photo detector converting light energy, or more precisely, photons, into a number of electrons that refer to a voltage using a capacitor. The arrival of photons in the imager happens randomly and this uncertainty is known as photon shot noise [Has14, p. 608; Gra+10, p. 3]. Random means that the arrival time as well as the number of incident photons is random.

The noise can be modeled with a Poisson distribution having a white spectrum [Vas08, pp. 42–43]. Using this distribution the mean equals its variance [HK94, p. 268]. The discreet probability distribution can be seen in Equation 2.23. The number of measured photons is stated with N, the number of expected photons λ and t is the time of interval. The number of expected photons is the factor λt. [Ett05, pp. 193–194; Has14, p. 608].

$$P(N = k) = \frac{e^{-\lambda t}\,(\lambda t)^k}{k!} \qquad k \geq 0 \tag{2.23}$$

A Gaussian distribution can be used to approximate a Poisson distribution where the expected number of photons is used as the variance:

$$E(N) = \lambda t = Var(N) \tag{2.24}$$

The number of incoming photons on each pixel should be large to get a good approximation. On the other hand when the number of photons is small, other noise sources typically outweigh photon shot noise [Jan07, p. 24; Has14, p. 608; Sch05, p. 26].

Equation 2.25 shows the standard deviation, photon shot noise, which only depends on the number of incoming photons [You16, pp. 107, 108].

$$\sigma_{photonShot} = \sqrt{N} \tag{2.25}$$

2.4.2.4 Dark current and dark current shot noise

Dark current is the generation of electrons in a photo detector without relating to incoming photons, so no illumination happens at that point. This leads to a current to flow. As this effect relies on thermal energy it strongly depends on the temperature. A Poisson distribution is used to model the generation of electrons which is then known as dark current shot noise [97, p. 428; Gra+10], similar to photon shot noise.

Illade-Quinteiro et al. provided an overview of dark current source generators dealing with a pinned 4-transistor pixel. They list thermal, surface, band-to-band tunneling, trap assisted tunneling and others as a dark current source [Ill+14]. Impurities or defects can be perpetrators [Cal05, pp. 22–23].

2.4.2.5 Quantization noise

The voltage stored in the capacitance of the PMD has to be converted into a digital number to apply post processing steps. Therefore, the time and value continuous signal gets converted to a time and value discreet signal with the help of an sample and hold unit and an ADC. The number of different values to which the incoming voltage can be quantized is limited by the resolution N in number of bits and is 2^N. The incoming voltage results in output values between 0 and 2^{N-1}. One quantization interval q of the input voltage is formulated in Equation 2.26. The quantization error is then $\pm q/2$ that can be modeled as quantization noise superposing the input signal [KE05, pp. 244–274; Müh14, pp. 73–75].

$$q = \frac{V_{max}}{2^{N-1}} \tag{2.26}$$

Frank et al. investigated in an error analysis. One outcome was that when quantizing a signal having low amplitudes, either in a large depth or at pixels that are overexposed, the measured depth error is large [Fra+09].

2.4.2.6 Photon Transfer Curve

Figure 2.14 shows different noise sources and their influence on the SNR. With a small amount of light intensity and even in completely dark conditions read noise takes into effect. It consists of several noise sources like reset noise and dark current and its shot noise. Photon shot noise takes into effect with respect to intensity. It has a slope of 0.5 when using a log-log illustration while the signal (which is light intensity) itself has a slope of 1 putting it on x- and y-axes [Jan07, p. 50].

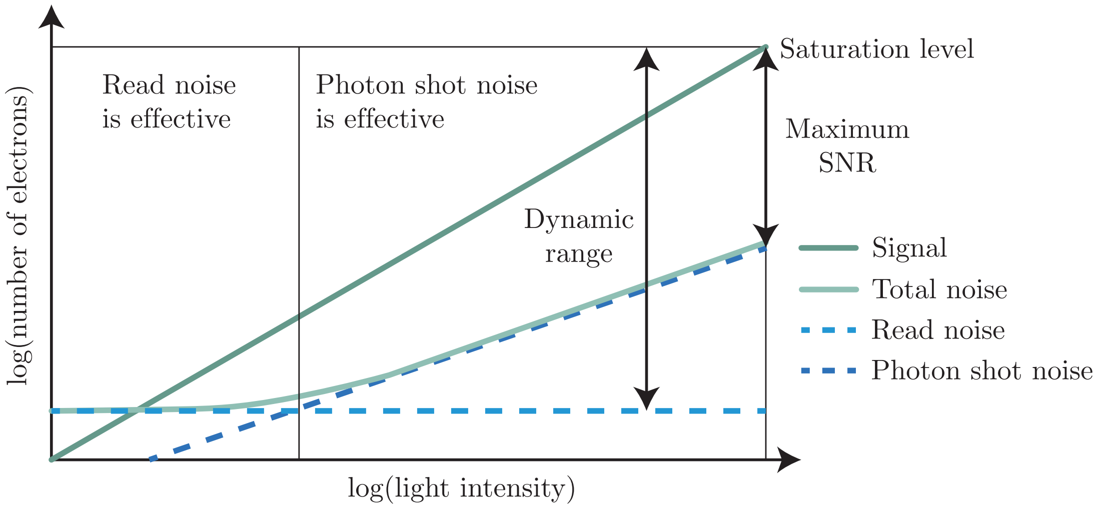

Figure 2.14: Various imager noise sources and the signal itself plotted over the light intensity to show their specific impact [Jan07, p. 49; Lan06, p. 71; Mur09, p. 50; Cho17, p. 33].

For all photo detectors a noise source that cannot be eliminated is photon shot noise which is therefore a limiting factor for the SNR [Lan06, p. 71]. Nevertheless, the greater slope of the signal over photon shot noise results in a high SNR. The full-well capacity of the imager that is a kind of saturation level directly corresponds to the maximum SNR. It is a factor of how much light, respectively charges, the sensor is able to measure. The difference between the minimum number of charges where a signal can be detected and the maximum number of electrons before saturation is reached (maximum level of the signal) is the dynamic range. Dynamic range and maximum SNR are typically claimed in decibel [Cho17, p. 32]. The SNR is stated in Equation 2.27, speaking of voltage output swing [Lua06, p. 52].

$$SNR = 20 \cdot \log_{10}\left(\frac{\Delta V_{signal}}{\Delta V_{noise}}\right) \tag{2.27}$$

The dynamic range DR is stated in Equation 2.28. Instead of using ΔV_{signal}, compared to the SNR, the maximum output voltage swing is used. Another definition uses minimum noise floor for the denominator according to [Lua06, p. 52].

$$DR = 20 \cdot \log_{10}\left(\frac{\Delta V_{max}}{\Delta V_{noise}}\right) \tag{2.28}$$

2.5 State-of-the-Art

This section provides an overview of recent literature which concentrates on the same goal, to model a ToF sensor or have similar background.

2.5.1 Photonic mixing device system

Schneider modeled a complete PMD system using Matlab / Simulink. The system is divided into four parts: Performance balance of the phase delay process, the opto-electric correlation process, signal processing and evaluation. The first process belongs to the optical part relating to the illumination unit, background light and the receiving unit. The optical power at the output of the sender and following the irradiance at an object using polar coordinates is calculated. With a remission factor the scene irradiance is calculated back to a specific PMD pixel. For the receiving unit a filter and a lens are incorporated. In the model the background light is constant at any distance and the signal power is proportional to $1/r^2$. The opto-electric correlation process deals with charge generation of the photoelectric effect inside the PMD pixel and the signal mixing via the cross correlation function. A sum over multiple modulation periods of the resulting correlation signals leads to a voltage stored in a capacitor where saturation is applied. Noise effects are modeled in the signal processing part where photon shot noise and quantization are considered. The last process consists of the implementation of different phase algorithms and the alternative use of pseudo-noise sequences instead of using harmonic signal modulation [Sch05].

2.5.2 Physical model

Schmidt has a different approach of modeling a ToF sensor. The model is oriented on the specific ToF camera PMD CamCube ToF. Reflectivity and depth maps are used as input while the quality of depth images generated is examined. The model approach consists of five processes: Excitation, light source, target response, sampling and analysis. The internal behavior of the PMD pixel is modeled for a 2-tap sensor where each tap is considered separately. A SBI circuit is included to incorporate background light suppression [Sch11].

Chapter 3

Design

When designing a physical model for a ToF camera the whole ToF system has to be modeled in order to investigate common errors and precision. A generic design approach is used so the model does not only hold for a specific ToF camera but it is restricted to a CW modulation based setup only. Figure 3.1 illustrates an overview of the model that is split up in different modules to provide high flexibility. That is why the model can be extended in an efficient way or used for other physical models. It includes

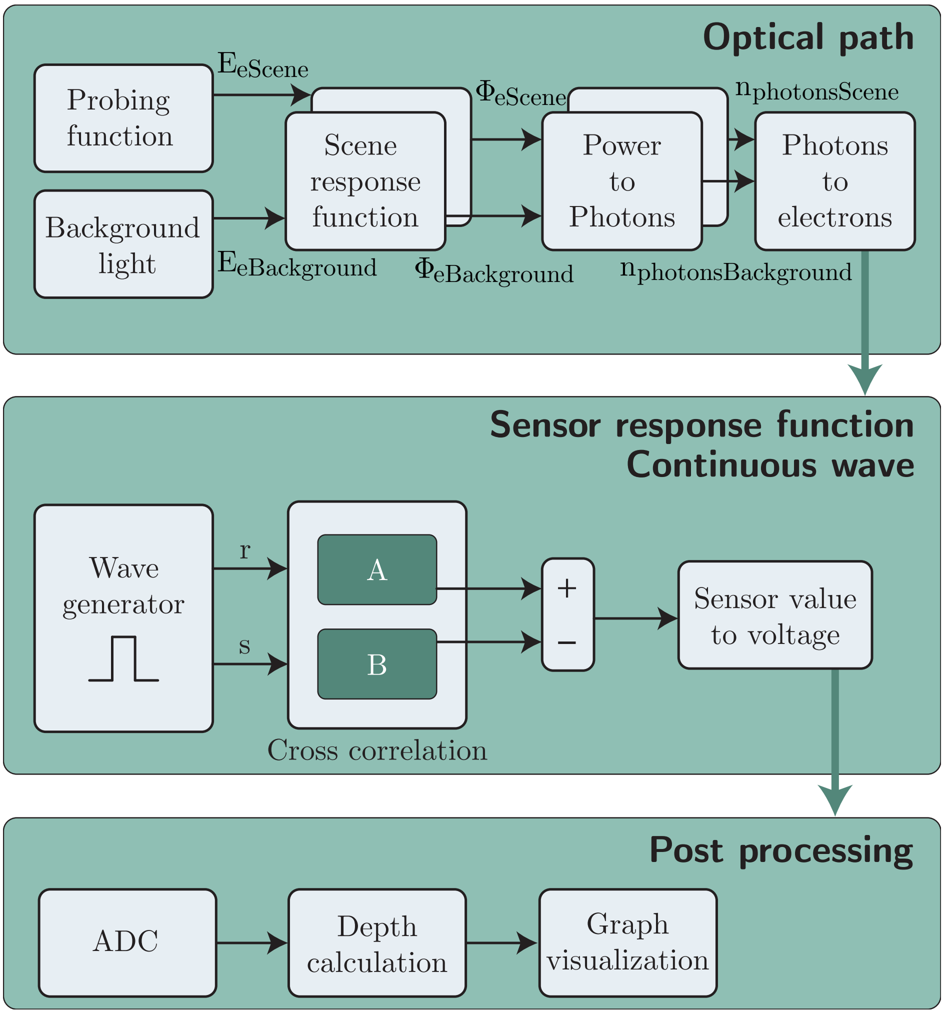

Figure 3.1: The physical model containing an optical path, a sensor response function and a post-processing unit.

an optical path with a modulated light source and disturbing background light. It is assumed, that the light source is placed at exactly the same position as the camera. Furthermore, a point light source is used. The sensor response function models the internal behavior of the ToF sensor using CW modulation while the last module provides post-processing steps. The modules consist of smaller units to encapsulate different functions which are explained in this section. Each processing unit can be parameterized to obtain a powerful model.

3.1 Optical path

The optical path is chosen to be the entry point of the model. It consists of a *probing function* that represents the generation of a modulated light signal and a *background illumination* unit. Both units provide a signal that hits an object in a scene. The shape of the light source is essential, however influences such as multi reflection, interferences and position of the background light are neglected. Both signals are then reflected back to the sensor (which consists of one PMD pixel only). The reflection is modeled with the *scene response function*. The output of this module is a number of electrons, produced in the ToF sensor due to the photoelectric effect.

3.1.1 Probing function

The probing function includes parameters of the light source and calculates how much emitted power an object area receives. The specified input parameters are d, Field of View (FoV) and Φ_{eIllu}. Its output parameter is E_{eScene}.

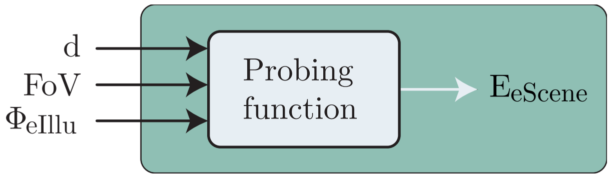

Figure 3.2: Input and output parameters of the probing block.

A VCSEL or an IR LED is commonly used for the illumination unit. The exact characteristics of such a hardware element are not modeled. A point light source is assumed instead of an area one, illustrated in Figure 3.3. The power of the emitting light source will be modeled in radiant flux Φ_{eIllu} that is a given parameter and is defined in [87c].

A cone is used as unit of volume where the illumination unit emits Φ_{eIllu} in an equal distribution within a given FoV. A right circular cone is used as radiation area. When radiant flux hits an object in the scene one speaks of irradiance E_{eScene}, which is radiant flux in respect to an area. Latter is a planar circular area A_{Scene}. Heredia Conde uses a spherical sector but the area can be simplified to a planar circular area as only one pixel of the ToF camera will be modeled [Her17, p. 403]. When modeling multiple pixels a planar area can also be used but one has to be aware that in the scene response function when power is reflected, center pixels will receive a different power value than pixels on an edge.

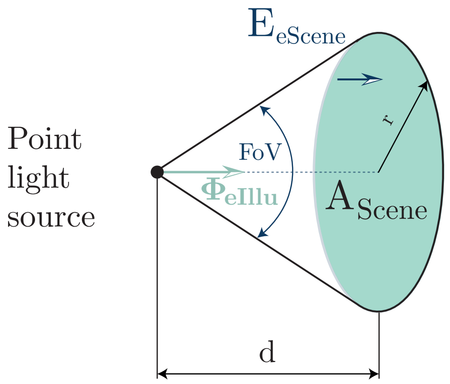

Figure 3.3: A point light source projects its emitting radiant flux Φ_{eIllu} into an even circular shaped area in a scene. Irradiance E_{eScene} is the whole electromagnetical power that hits the area A_{Scene}.

The calculation of the circular area A_{Scene} is done with Equation 3.1. The radius is gathered with geometry of a rectangular triangle $\tan\left(\frac{FoV}{2}\right) = \frac{r}{d}$ using the distance d as adjacent and radius r as opposite.

$$A_{scene}\ [m^2] = r^2 \cdot \pi = \left(\tan\left(\frac{FoV}{2}\right) \cdot d\right)^2 \cdot \pi \tag{3.1}$$

The irradiance follows from [87e] in Equation 3.2.

$$E_{eScene}\left[\frac{W}{m^2}\right] = \frac{\Phi_{eIllu}}{A_{Scene}} \tag{3.2}$$

3.1.2 Background light

For a more realistic model background light has to be considered in the optical path. It can be the sun, a halogen lamp, an incandescent light bulb or others. The illuminance E_v of the light source is a given parameter.

The specified input parameters are λ, sel, K_m, $filter$ and E_v. Latter is defined in [87f]. Its output parameter is $E_{eBackground}$. The parameter sel stands for the selection of the light source, λ is the wavelength of the illumination unit and $filter$ is related to lambda to define the optical filter of the camera. The other parameters are now described.

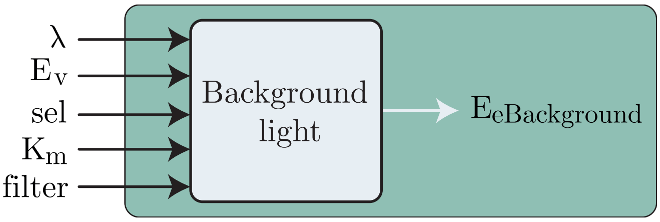

Figure 3.4: Input and output parameters of the background light block.

In this model $\frac{W}{m^2}$ is taken as power unit. Illuminance has to be converted into this unit first. In order to achieve this conversion the luminous flux Φ_v has to be determined with the given Equation 3.3 [87d]. It describes the radiation that a light source emits in form of visible light that corresponds to the human eye.

$$\Phi_v\ [lm] = K_m \cdot \int_0^{\infty} V(\lambda) \cdot \frac{d\Phi_e(\lambda)}{d\lambda} d\lambda \tag{3.3}$$

To examine this formula more closely the light sensitivity of the human eye is explained. The range of wavelengths λ from about 400 nm to 700 nm of the electromagnetic radiation spectrum causes a perception of light in the human eye which is recognized as visible light [Uda14, pp. 67–68]. Different wavelengths do not result in the same brightness sensitivity. The luminosity curve relates to the brightness sensitivity of the human eye and is standardized to 1, which stands for the maximum sensitivity at about 555 nm. The multiplication factor K_m is the luminous efficacy of radiation [87g] with value 683 $\frac{lm}{W}$ and corresponds to the maximum of the curve. $\Phi_e(\lambda)$ denotes the radiant flux.

$$E_{eBackground} \left[\frac{W}{m^2}\right] = \frac{E_v}{\Phi_v} \cdot \Phi_e; \tag{3.4}$$

The background irradiance can now be calculated with Equation 3.4 using Φ_e as radiant flux.

3.1.3 Scene response function

The probing function block produces an irradiance E_e on the area A_{Scene}. This irradiance will be reflected and brought back to a center pixel of the ToF sensor. The irradiance can either originates from the probing function as illumination of the sensor or background irradiance. Figure 3.5 shows input and output parameters of the scene response function block and Figure 3.6 illustrates the behavior that is now explained in detail. This block is designed to be executed twice for the probing function and the background light block.

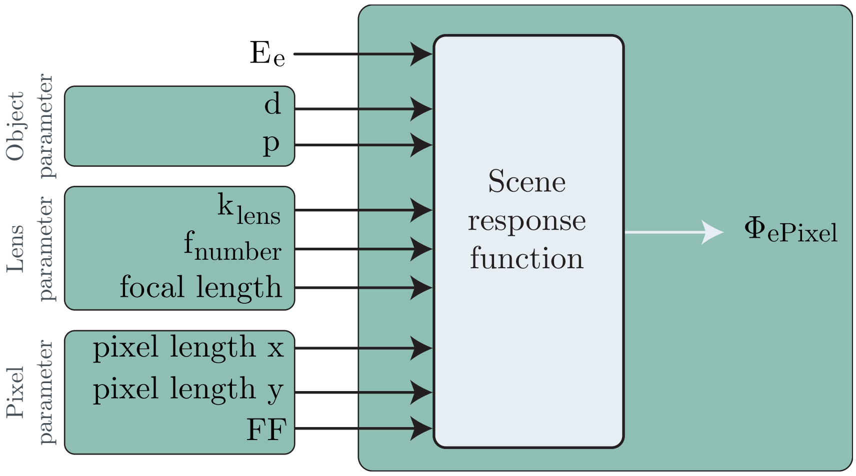

Figure 3.5: Input and output parameters of the scene response function block.

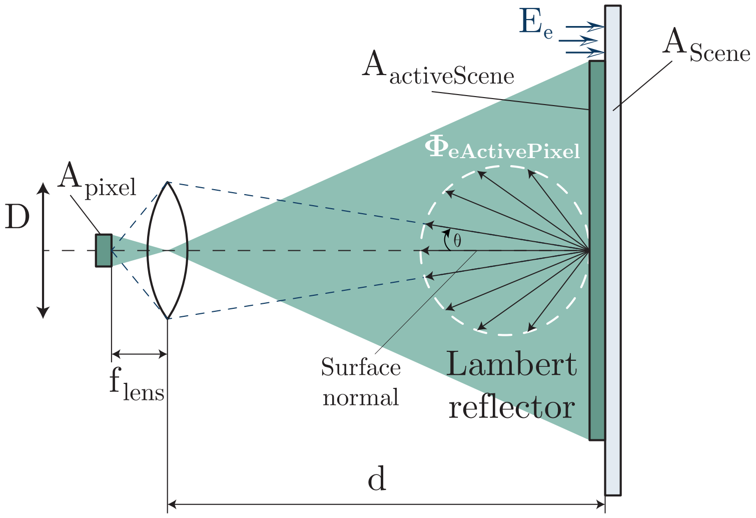

Figure 3.6: A known irradiance E_e is converted into radiant flux $\Phi_{eActivePixel}$ with Equation 3.7 reflected by a lambertian surface. It is assumed that the illumination unit (the light source of either an LED or a VCSEL) is placed at the same position as the center pixel of the pixel array.

The derivation of the radiant flux Φ_{ePixel} of one pixel is shown with Equation 3.11 having the output of the probing function block as input parameter.

Not the whole area of a PMD pixel is sensitive to light and therefore the area in the scene which relates to a pixel is not A_{Scene} but a smaller area $A_{activeScene}$. According to [Her17, pp. 402–405] the area relating to the active pixel area of the sensor can be formulated as

$$A_{activeScene}\ [m^2] = \left(\frac{d}{f_{lens}}\right)^2 \cdot A_{PixelActive} \tag{3.5}$$

The distance between the sensor and the lens is approximately the focal length f_{lens} of the lens. The space between the lens and $A_{activeScene}$ is d. Equation 3.6 gives the active area of a pixel dependent on a pixel's vertical and horizontal length and the Fill Factor (FF). The fill factor is the ration between the active and blind area of the pixel.

$$A_{PixelActive}\ [m^2] = \text{pixelLengthX} \cdot \text{pixelLengthY} \cdot FF \tag{3.6}$$

The irradiance that will be reflected with the reflection factor p is

$$\Phi_{eActivePixel}\ [W] = p \cdot E_e \cdot A_{activeScene} \tag{3.7}$$

[Lan06, pp. 85–86] showed the derivation of the relation factor between the power in front of the lens and the power at the reflection area which is

$$\Phi_{eLens}\ [W] = \Phi_{eActivePixel} \cdot \left(\frac{D}{2 \cdot d}\right)^2 \tag{3.8}$$

The derivation relies on a lambertian reflection. It is a reflectance model of a Bidirectional Reflectance Distribution Function (BRDF) and declares how much the radiant intensity decreases with a declining radiation angle θ. The factor which describes the decrease in radiant intensity is $\cos(\theta)$, measured between the surface normal and the direction. The final radiant flux that enters one pixel is determined by the radiant flux of the lens, damped by a factor k_{lens} that models the losses of the lens and their filters.

$$\Phi_{ePixel}\ [W] = \Phi_{eLens} \cdot k_{lens} \tag{3.9}$$

The f-number of a lens is the ratio between the focal length and the effective aperture diameter [Lan00, p. 43]:

$$f_{number} = \frac{f_{lens}}{D} \tag{3.10}$$

Combining above equations including the formula of the probing function Equation 3.2 leads to a complete formula for the received radiant flux Φ_{ePixel} of a center pixel.

$$\begin{aligned}
\Phi_{ePixel}\ [W] &= \Phi_{eActivePixel} \cdot \left(\frac{D}{2 \cdot d}\right)^2 \cdot k_{lens} \\
&= p \cdot E_e \cdot A_{activeScene} \cdot \left(\frac{D}{2 \cdot d}\right)^2 \cdot k_{lens} \cdot p \\
&= \frac{\Phi_{eIllu}}{A_{scene}} \cdot A_{activeScene} \cdot \left(\frac{D}{2 \cdot d}\right) \cdot k_{lens} \cdot p \\
&= \frac{\Phi_{eIllu}}{A_{scene}} \cdot \left(\frac{d}{f_{lens}}\right)^2 \cdot A_{PixelActive} \cdot \left(\frac{D}{2 \cdot d}\right)^2 \cdot k_{lens} \cdot p \qquad (3.11) \\
&= \frac{\Phi_{eIllu}}{\left(\tan\left(\frac{FoV}{2}\right) \cdot d\right)^2 \cdot \pi} \cdot \frac{\cancel{d^2}}{f_{lens}^2} \cdot A_{PixelActive} \cdot \frac{D^2}{4 \cdot \cancel{d^2}} \cdot k_{lens} \cdot p
\end{aligned}$$

with the use of Equation 3.10 the formula evaluates to

$$= \underline{\frac{\Phi_{eIllu} \cdot k_{lens} \cdot p \cdot FF}{f_{number}^2} \cdot \frac{pixelLengthX \cdot pixelLengthY}{4\pi \cdot \left(\tan\left(\frac{FoV}{2}\right) \cdot d\right)^2}}$$

3.1.4 Power to photons

The radiant flux Φ_{ePixel} is converted into photons with this block. With a known wavelength λ and the speed of light c (which is the phase velocity for electromagnetic radiation in vacuum) the frequency can be calculated:

$$\lambda\ [m] = \frac{c}{f} \rightarrow f\ [Hz] = \frac{c}{\lambda} \tag{3.12}$$

The Planck constant h gives the relation between the energy of a photon and an electromagnetic radiation frequency [11a]:

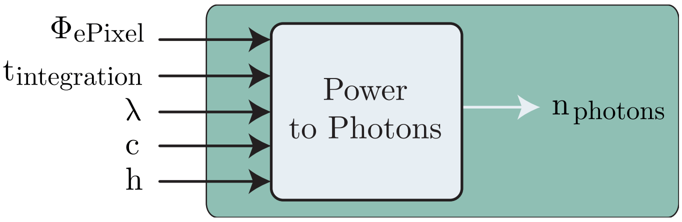

Figure 3.7: Input and output parameters of the power to photons block.

$$E_{Photon}\ [J] = h \cdot f = h \cdot \frac{c}{\lambda} \tag{3.13}$$

To get the energy one pixel receives within the integration time, respectively illumination time, the radiant flux Φ_{ePixel} has to be multiplied by the integration time.

$$E_{Pixel}\ [J] = \Phi_{ePixel} \cdot t_{integration} \tag{3.14}$$

With the knowledge of the energy of one photon and the received energy the number of photons can be calculated:

$$n_{photons}\ [1] = \frac{E_{Pixel}}{E_{Photon}} \tag{3.15}$$

3.1.5 Photons to electrons

This block covers the optical to electrical transition of the ToF sensor where photons are converted to electrons.

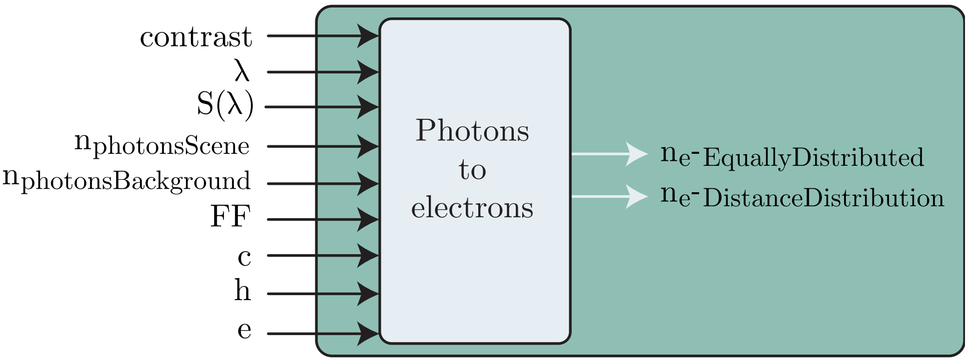

Figure 3.8: Input and output parameters of the photons to electrons block.

Not every photon that hits the ToF sensor generates an electron-hole pair. The factor that describes this issue is characterized as quantum efficiency $\eta(\lambda)$ that is ≤ 1 and depends on the wavelength, Equation 3.16 [HBG14, p. 343]. This relation does not hold for a single photon avalanche diode. The symbol e is the elementary charge [11b].

$$\eta(\lambda) = \frac{S\,(\lambda)}{\lambda} \cdot \frac{h \cdot c}{e} \tag{3.16}$$

In Equation 3.17 $S(\lambda)$ denotes the spectral sensivity / responsivity [87g] where photo current I_{ph} is the electrical output and Φ_e the received radiant energy [HBG14, p. 343]. This value can usually be taken from the data sheet of the corresponding ToF sensor.

$$S(\lambda)\left[\frac{A}{W}\right]=\frac{I_{ph}}{\Phi_e} \tag{3.17}$$

Knowing the quantum efficiency and the number of photons leads to a number of generated electrons in the sensor:

$$\begin{aligned} n_{e^-} &= n_{photonsScene}\cdot\eta(\lambda) \\ n_{e^-Background} &= n_{photonsBackground}\cdot\eta(\lambda) \end{aligned} \tag{3.18}$$

The total number of electrons n_{e^-} is not equally distributed in channel A and B of the smart pixel. $n_{e^-DistanceDistribution}$ electrons are distributed with respect to the distance and $n_{e^-EquallyDistributedContrast}$ are equally distributed to A and B, Equation 3.19 and 3.20. The factor contrast(contrast ≤ 1) denotes the demodulation contrast and is a factor of performance performing demodulation inside a single pixel [Her17, pp. 62–63].

An example: Let $n_{e^-} = 100$ and having a demodulation contrast of 60%. This means that 60 electrons are distributed in A and B with respect to the distance and 20 electrons between A and B.

$$n_{e^-EquallyDistributedContrast} = n_{e^-}\cdot(1-\text{contrast})\cdot 0.5 \tag{3.19}$$

$$n_{e^-DistanceDistribution} = n_{e^-}\cdot\text{contrast} \tag{3.20}$$

Additionally, the electrons that have their origin in the background light are added to the equal distribution

$$n_{e^-EquallyDistributed} = n_{e^-EquallyDistributedContrast} + n_{e^-Background} \tag{3.21}$$

3.2 Sensor response function

The sensor response function describes the internal behavior of the ToF sensor and how the PMD pixel works. The behavior is explained with Figure 3.9. Before the principle of the PMD pixel can be explained two waveforms have to be generated.

3.2.1 Waveform generation

A reference pulse is generated, labeled with $r(t)$. In literature a cosine-shaped signal is preferred as optimal signal [Lef+13, p. 5; Lin+10, p. 1319], $r(t) = A\cdot cos(2\pi\cdot f_{mod}\cdot t + \varphi) + K$ with amplitude A, modulation frequency f_{mod}, time value t, phase offset φ and offset K. In this model other waveforms can be generated, like a square wave. For the sensor response function only one period of the signal is examined as the other periods do not reveal new information.

The second pulse $s(t)$ models the reflected signal of an emitted light pulse with phase offset φ_{phase}, which is reflected in a scene. Due to the time-of-flight of the emitted light pulse $\varphi_{reflected}$ is added as phase shift. The final phase offset is called φ, see Equation

3.23. $\varphi_{reflected}$ is determined by converting a given distance d to a phase according to Equation 3.22 [Lef+13, p. 5].

$$\varphi_{reflected}\,[rad] = d \cdot \frac{4 \cdot \pi \cdot f_{mod}}{c} \tag{3.22}$$

$$\varphi = \varphi_{phase} + \varphi_{reflected} \tag{3.23}$$

All other wave parameters are identical with the one of the reference pulse. The duty cycle of both waves can be adjusted with *dutyCycleR* for the reference signal and *dutyCycleS* for the received signal. Usually the reference signal has a duty cycle of 50% while the reflected signal can have a duty cycle of less than 50%.

3.2.2 Smart pixel

The functional principle of the PMD pixel has already been discussed in Section 2.3. A cross correlation of the reference and the received signal is performed which is defined in Equation 3.24 [97, p. 144]. A 2-tap PMD pixel is considered in the model. Therefore, the cross correlation has to be performed twice, for tap A and B.

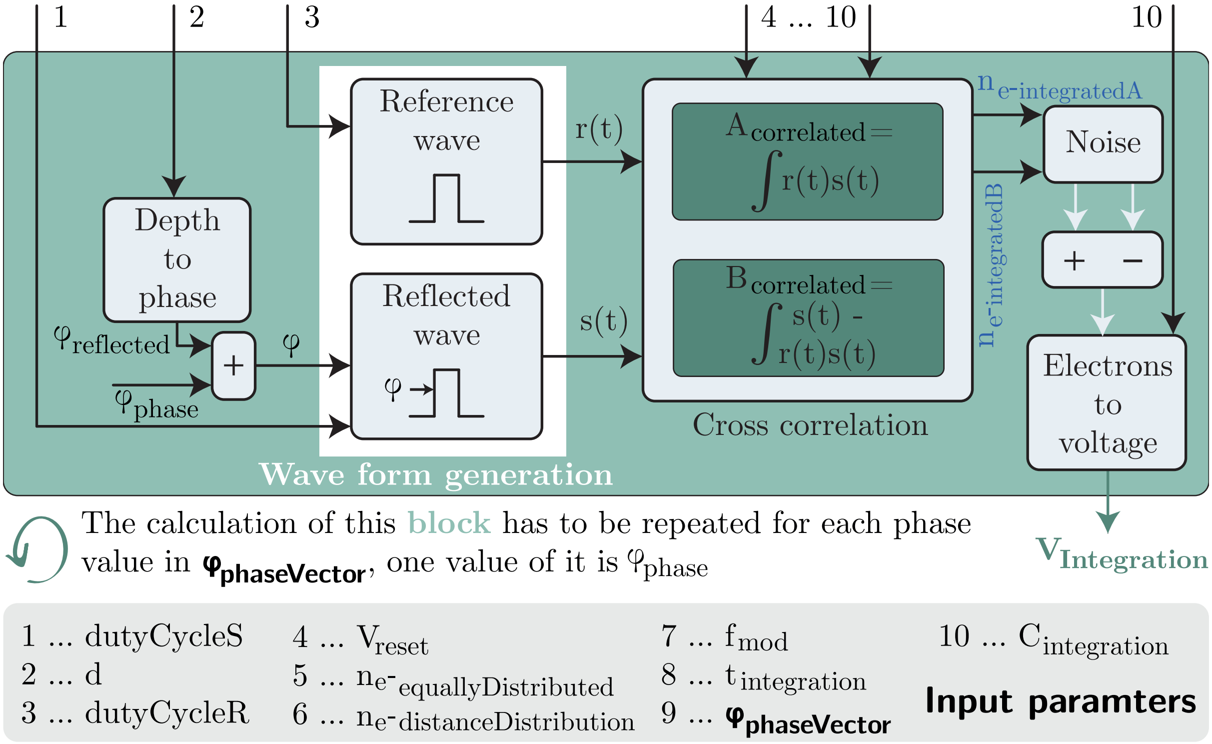

Figure 3.9: Overview of the smart pixel principle.

$$R_{xy}(\tau) = \lim_{T \to \infty} \int_0^T r(t) \cdot s(t + \tau)dt \tag{3.24}$$

Figure 3.10 shows the principle of the correlation with sample values using a rectangular wave shape. In contrast to literature, the reference signal is characterized by the symbol

r and the received signal with s. The latter, $s(t)$ is phase shifted by $\varphi = +70°$ to $r(t)$ in this example. One period of the signals is plotted to explain the behavior.

Starting with tap A the two signals are multiplied $r(t) \cdot s(t)$. The result is a square wave with amplitude unequal to zero only in the green marked range $\mathbf{A_{correlated}}$ else zero. To receive the square wave for tap B the following calculation has to be done: $s(t) - r(t) \cdot s(t)$.

According to Section 2.3 at the beginning of the reset phase the capacitor $C_{integration}$ is connected to V_{reset}. At this point the model does not process voltage but electrons. That is why Equation 3.25 transforms V_{reset} to a number of electrons n_{e^-reset}.

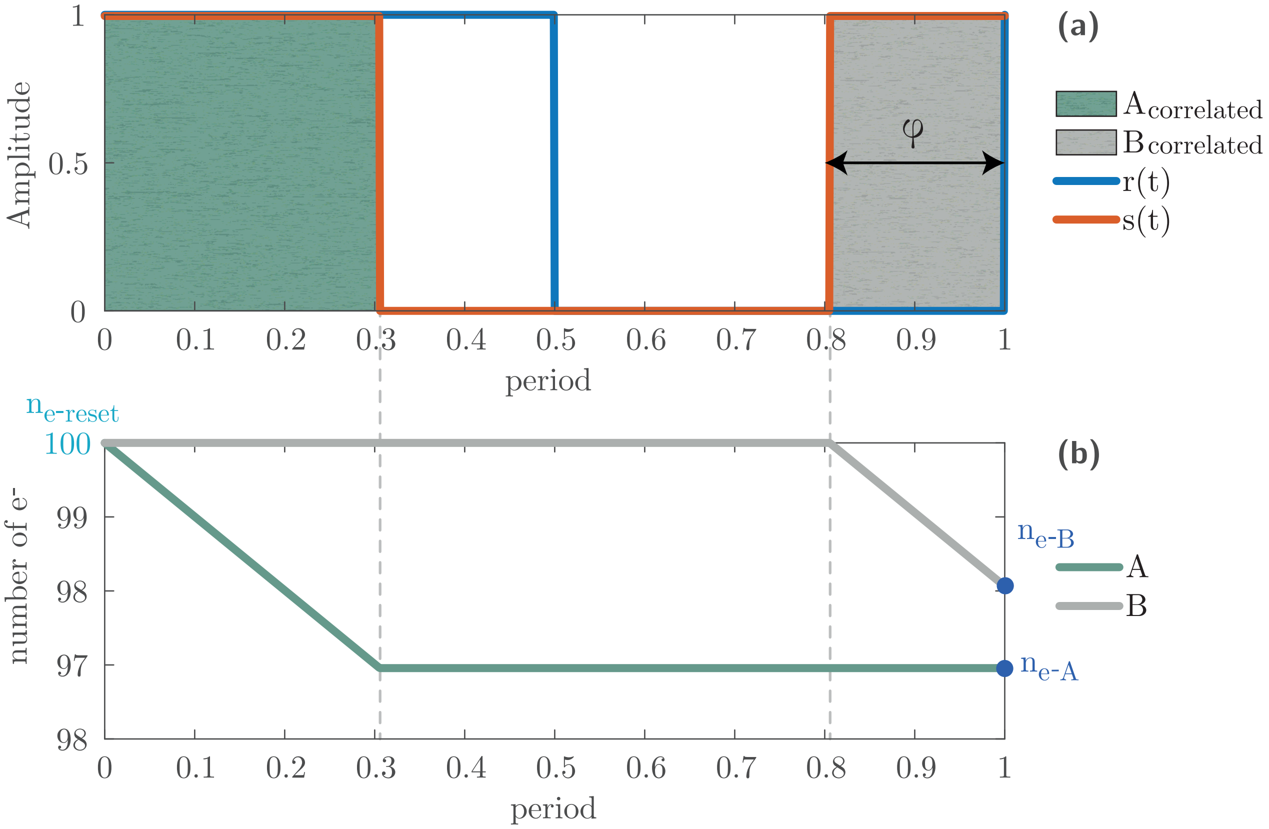

Figure 3.10: Reference and received signal (a) having a phase shift to each other. (b) shows how the integration is performed for tap A and B.

$$n_{e^-reset}\ [1] = \frac{V_{reset} \cdot C_{integration}}{e} \tag{3.25}$$

The values of Figure 3.10 are taken randomly. In the exposure phase the capacitor is disconnected from V_{reset}. The discharge of the capacitor is modeled with the down-integration of the square wave $A_{correlated}$, respectively $B_{correlated}$ over one period, which results in the two signals in Figure 3.10(b). The amount of integration is calculated with Equation 3.26, dividing the whole number of electrons to distribute over a given distance by the number of periods.

$$n_{e^-perPeriod}\ [1] = \frac{n_{e^-distanceDistribution}}{n_{periods}} \tag{3.26}$$

Two extreme cases exist. When $r(t)$ and $s(t)$ are in phase all electrons move to tap A. When they are completely out of phase ($s(t)$ has a phase offset of 180°) all electrons move to tap B. When modulating the two signals with a modulation frequency of f_{mod} and integrating over the time $t_{integration}$ the number of periods can be determined with Equation 3.27. The described behavior has to be applied for all periods of time. As the behavior stays the same for all periods, one period can be determined and then multiplied by $n_{periods}$.

$$n_{periods}\ [1] = t_{integration} \cdot f_{mod} \tag{3.27}$$

Integrated electrons for one period are expanded to all periods and the number of electrons that are equally distributed in A and B contribute to the integrated electrons:

$$n_{e^-integratedA}\ [1] = n_{e^-reset} - n_{e^-A} \cdot n_{periods} + n_{e^-equallyDistributed} \tag{3.28}$$

3.2.3 Noise

The noise sources explained in Section 2.4 are considered in the following way. All noise sources are summed up quadratically. For the SBI noise thermal noise of the channel resistance is considered.

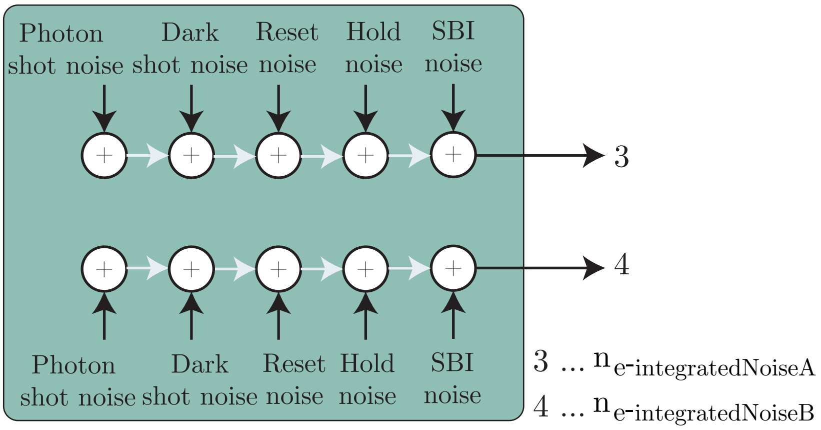

Figure 3.11: Considered noise sources.

$$n_{e^-noiseA} = \sqrt{n_{e^-ResetNoiseA}{}^2 + n_{e^-HoldNoiseA}{}^2 + n_{e^-PhotonShotNoiseA}{}^2 + n_{e^-DarkShotNoiseA}{}^2} \tag{3.29}$$

The pixel information lies in the difference between A and B. That is why Equation 3.30 generates the total number of integrated electrons.

$$n_{e^-integrated}\ [1] = n_{e^-integratedNoiseA} - n_{e^-integratedNoiseB} \tag{3.30}$$

Equation 3.31 converts the previously gathered electrons into a voltage.

$$V_{integrated}\ [V] = \frac{n_{e^-integrated} \cdot e}{C_{integration}} \tag{3.31}$$

3.2.4 Pixel saturation

Pixel saturation is explained with Figure 3.12. A pixel is saturated when the capacitor of either A or B is integrated from n_{e^-Reset} down to the lower bound of electrons, $n_{e^-Saturated}$. Below the saturation level the PMD diodes show an unexpected behavior compared to the explanations of Section 2.3. Figure 3.12(a) shows pixel saturation at strong background light. Both channels are saturated very fast while a weak background light in Figure 3.12(b) ends up in a slower saturation.

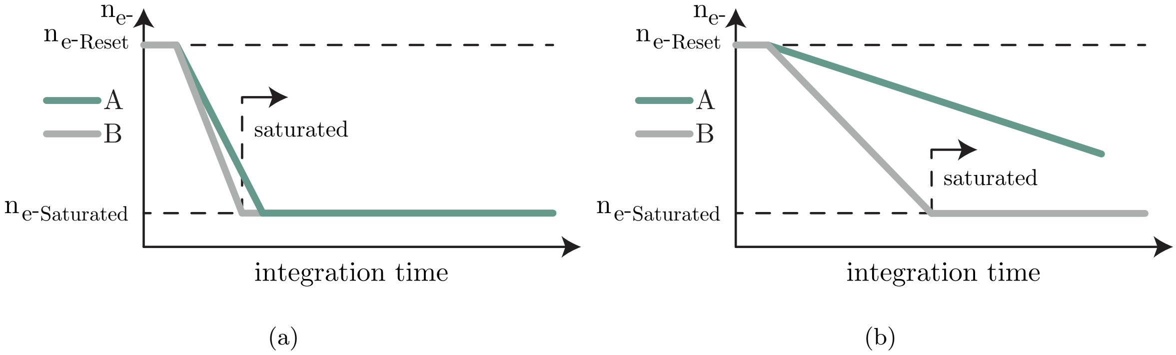

(a) (b)

Figure 3.12: Behavior of pixel saturation without SBI. Strong background light is shown in (a), weak background light in (b).

3.2.5 Suppression of background illumination

The dynamic range can be improved when using an SBI circuit which is implemented inside the ToF sensor, see Section 3.2.5. Figure 3.13 shows the enhanced behavior. When the first channel (here B) is saturated the other channel is integrated in positive direction from this point on but with a different slope $k = \frac{dy}{dx}$. This results in the use of the full voltage swing. Saturation takes places much later compared without SBI.

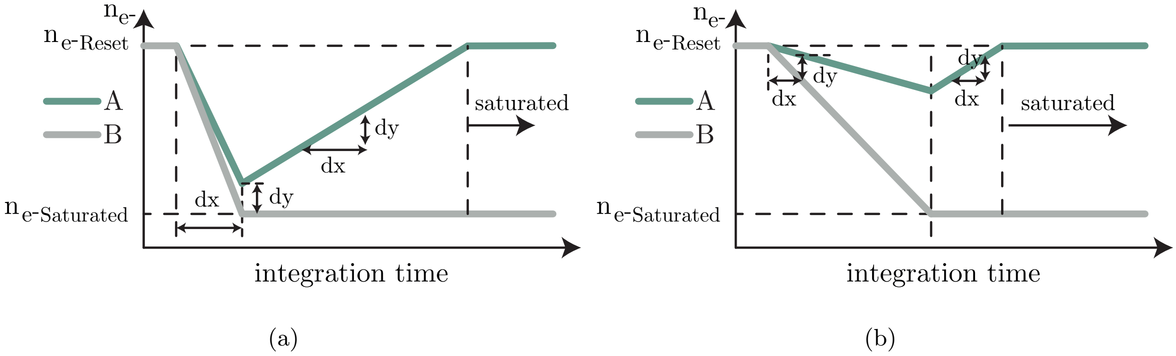

(a) (b)

Figure 3.13: Behavior of pixel saturation including SBI. Strong background light is shown in (a), weak background light in (b).

The SBI will be applied after the cross correlation but before noise is added.

3.3 Post processing

In this design phase an ADC converts integration voltages of the PMD to raw data, saturation will be applied and then a depth can be calculated from that. The last step is the visualization of the results.

3.3.1 Analog to digital converter

The ADC quantizes analogue input voltages to time and value-discreet raw data which are digital numbers. Basically, the quantization characteristic curve is modeled instead of choosing a concrete ADC implementation like successive approximation or sigma-delta.

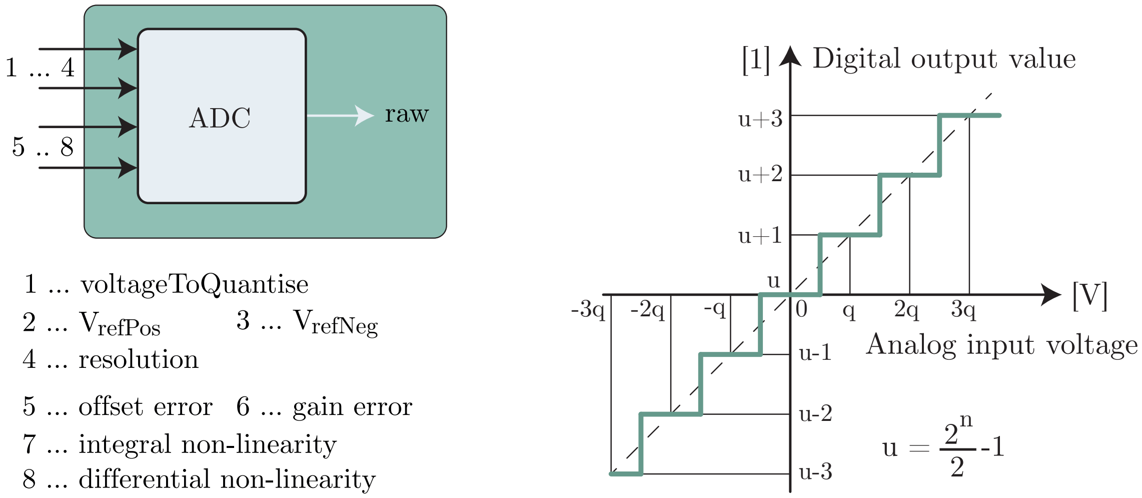

(a)

(b)

Figure 3.14: Input and output parameters of the ADC block (a). An extract of the quantization characteristic curve is illustrated in (b).

There are several input values that are discussed in more detail. Figure 3.14(a) gives an overview of selected parameters.

- voltageToQuantize

  This voltage belongs to the integration voltage of the PMD. When using the four-bucket algorithm to calculate some depth data, see Section 2.1.1.1, four measurements are needed which results in four voltages to be digitized. The value of the voltage may exceed or fall below the ADC's input voltage range resulting in the minimum or maximum digital output value of the ADC.

- V_{refPos}/V_{refNeg}

  The reference voltage V_{ref} of the ADC is defined to be half of the Full Scale Range (FSR). Its value is:

  $$V_{ref} = V_{refPos} - V_{refNeg} \tag{3.32}$$

  The resulting FSR results to:

  $$FSR = 2 \cdot V_{ref} \tag{3.33}$$

The ADC is then able to process input voltages from $-V_{ref}$ to V_{ref} and outputs a digital number between 0 and $2^{resolution} - 1$.

- resolution

  The resolution is given in number of bits. Therefore one quantization interval or more precisely one step of the quantization characteristic curve is recognized as q, see Equation 3.34.

$$q = \frac{FSR}{2^{resolution}} \tag{3.34}$$

The designed curve can be seen in Figure 3.14(b). It shows an extract of the full curve. The lower bound of analogue input voltage is $-V_{ref}$ that relates to the digital number of 0 while the maximum positive voltage relates to $2^{resolution} - 1$. The figure shows values around 0 V input voltage to give a better understanding how the ADC quantization works. The quantization characteristic curve is modeled to have a zero offset of -0.5 Least Significant Bits (LSBs). For better understanding a dotted line connects the middle of each step together and goes through the origin.

The following input parameters model ADC errors where each error is considered individually. For simplicity reasons negative input voltages are not shown.

- Offset error

  Figure 3.15(a) illustrates a positive offset error. The line that connects the middle of each stair does not go through the origin. The curve is moved prior the positive or negative side of the x axis. In data sheets the offset value is often declared in number of LSBs.

- Gain error

  The gain error is a deviation of the ideal slope of 1. This error leads to a changed stair width through the whole curve. The value of the error will be given in a percentage of FSR.

- Integral non-linearity

  The deviation of the ideal transfer function which is a line is described by this error. The ideal line goes through the origin; the middle of all stairs therefore connects minimum and maximum output value. The error is modeled in a way that the ideal line is replaced by a polynomial function. The value of this error is given in number of LSBs.

- Differential non-linearity

  Ideally all stair widths are equal. The differential non-linearity error is an absolute value given in percentage of one LSB and describes the deviation of the nominal value of one LSB. This leads to unequal stair widths.

3.3.2 Analog digital converter saturation

A raw value is defined to be saturated when all raw values of a phase measurement (e.g. four) are either minimum or maximum of the ADC's raw output value. Such values are set to zero as they do not include correct distance information.

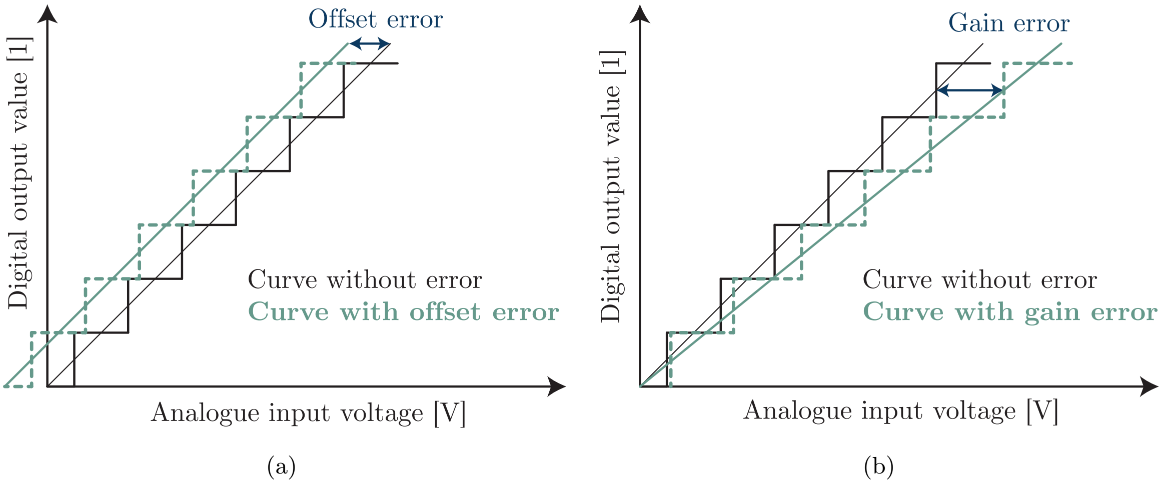

(a) (b)

Figure 3.15: Offset (a) and gain (b) error.

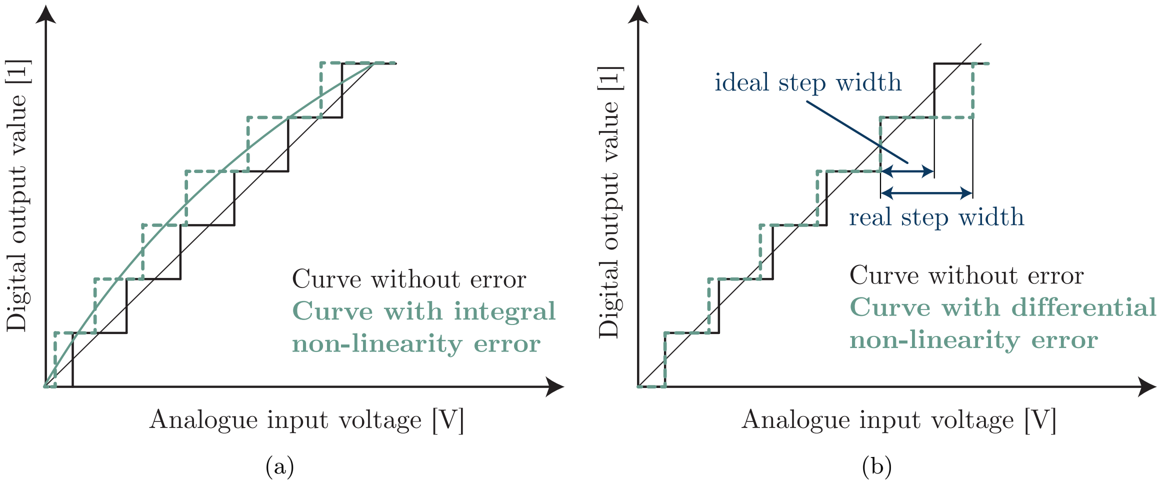

(a) (b)

Figure 3.16: Integral (a) and differential non-linearity error (b).

3.3.3 Depth calculation

In this step, depth information is calculated which is a synonym to a distance. It has to be considered to use the correct algorithm for distance calculation because it depends on the number of emitted phases (subframes).

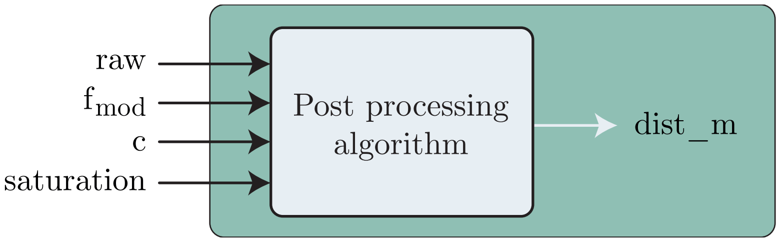

Figure 3.17: Input and output parameters of the distance calculation function.

The parameter *raw* belongs to the output of the ADC, f_{mod} is the modulation frequency, c is the speed of light and saturation is a factor which says whether the specific raw data contains valid data or not.

3.3.4 Result presentation

Results of the model should be made visible with various figures. The following major plots are defined so as to be generated:

- Distance noise versus real distance
- Calculated distance versus real distance including the unambiguity range
- Distance noise versus ambient light
- Distance noise versus integration time
- Cross correlation showing integrated voltages

3.4 Graphical user interface

For a better handling of the model a GUI is implemented. The sense behind this is that a user has to adjust a given set of parameters and select a way the result should be presented without dealing with the source code. Matlab App Designer is used to implement a GUI. The old version of Matlab GUI design was GUIDE which stands for GUI development environment. The major difference between the two is the coding of callbacks and graphics support as well as the new version is able to create an app that is able to be installed in Matlab [18a].

The following tasks should be implemented:

- Segmentation of input parameters
- Graphical representation of illumination and reference signal
- Graphical representation of the FoV
- Overview page to choose a sweep scenario
- Result presentation with selectable figures

3.5 Verification

The model is verified against real data with a ToF platform in a laboratory. This section starts with an introduction of a selected ToF platform used to verify the results of the model. It continues in the test setup and the software to read out data of the ToF sensor.

3.5.1 Linear Translation Stage

Figure 3.18 illustrates the laboratory setup to measure data with a ToF platform. The laboratory is a elongated room where the walls are lined with a black IR absorbing material so that multi reflections or interferences do not influence the measurement. At one end of the room a target material is assembled which has a defined IR reflection factor of 90%. A linear translation stage is shown in the figure which can be controlled via software to move towards the target or backwards. The precision of the movement of the stage is very high which is necessary to compare the results with the model. The maximum distance to the target is 4.5 meters. The ToF hardware is mounted on a board with fixed height focusing the target. Both the Linear Translation Stage (LTS) and the ToF hardware are connected via Universal Serial Bus (USB) interface. The idea is to measure distances in equidistant intervals over the whole range of 4.5 meters for a sweep over distance.

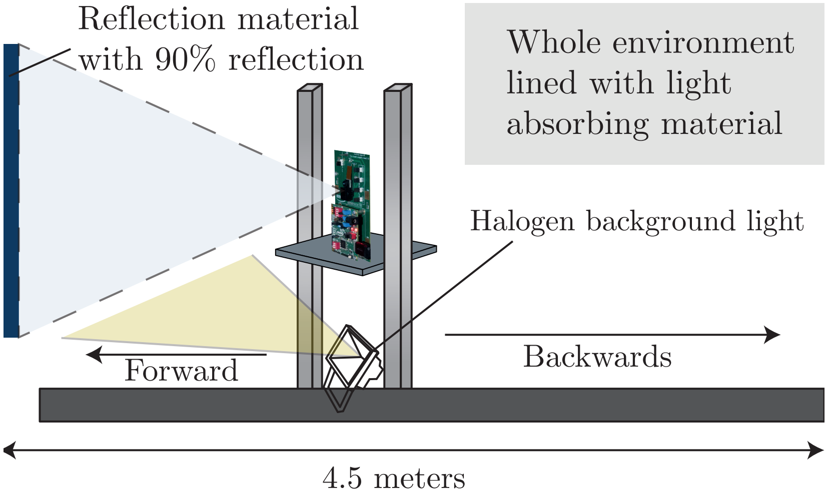

Figure 3.18: The ToF platform mounted on the LTS to obtain comparable measurements.

3.5.2 Gathering data

A given Python project is used as starting point which is able to gather raw images from the ToF sensor and calculate some depth data. Figure 3.19 shows a class diagram of the project. The main class is Wiggling. It uses *Animator* Application Programming Interface (API) to establish a connection to the board and transfer data. Furthermore, it is used to send register settings to the imager like the integration time or number of phases.

Another API used is *IQDrive* that controls the LTS. It offers functions to get the current position of the mounted ToF camera, set the velocity, to move forward or backward and others.

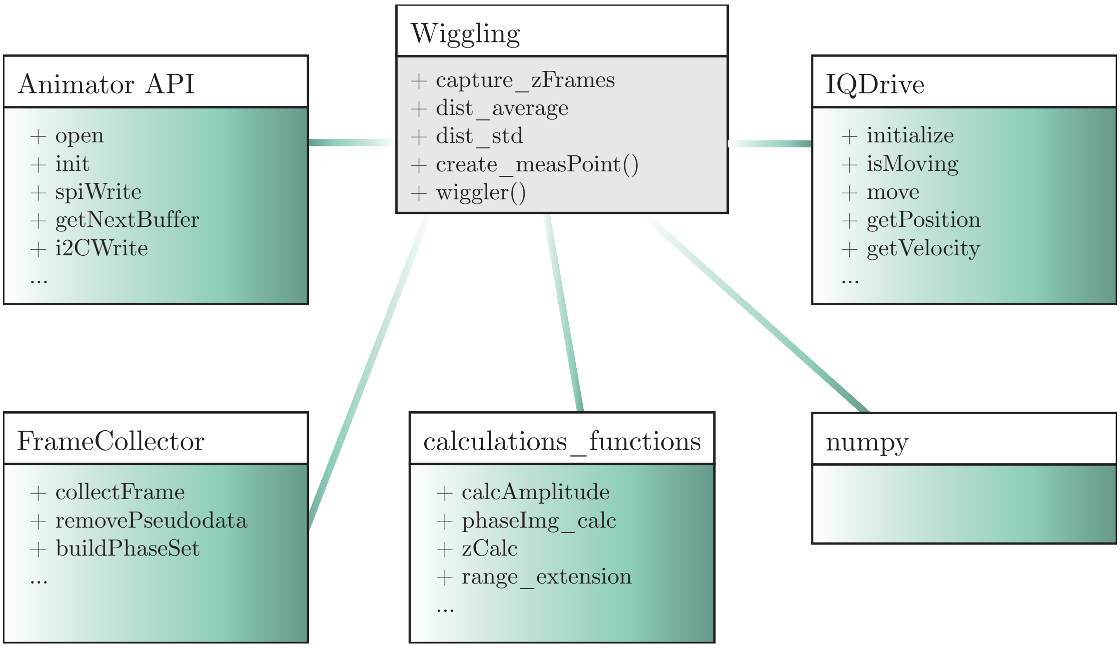

Figure 3.19: Class diagram of the of the software framework to gather depth data.

The class *FrameCollector* contains functions to collect a frame and put it into a buffer. A set of frames needs to be checked in order to confirm that they belong together. When this occurs they are packed into a list. Four phases are then used to calculate a phase image which gets further processed to obtain a depth image. The appropriate functions are located in *calculations_functions*. *NumPy* is used for calculations. The function *wiggler* in the Wiggling class uses a two-frequency measurement including a range extension to extend the unambiguity range. This algorithm will not be used, only the measurement of the 80 MHz setup. The file is called Wiggling as this error is not corrected in the functions.

The project has to be extended to use CSV export of results instead of binary data. This makes post processing in Matlab more convenient. Depth measurements of a sweep over the distance should be packed and stored in one file as well as direct computation of the average and standard deviation. Furthermore, the project has to be extended that a sweep over the integration time and background illuminance is possible. Therefore, necessary functions have to be introduced. One function to implement is the one to change the integration time of the sensor. Appropriate register values have to be calculated.

Chapter 4

Implementation

This chapter begins with an explanation of the used hardware and software environment. It continues with a description how the model is implemented in software, and how real distance data is gathered from a given ToF platform. The chapter ends with an explanation to verify the model against real data.

4.1 Environment

Before implementation can begin, necessary software and hardware platforms need to be specified. This section gives an overview of used resources.

4.1.1 Matlab

In the beginning Matlab Simulink was tested whether there would be any advantage to its use, however it was decided to use the program Matlab on its own to model a ToF camera. Matlab is a program from MathWorks that allows vectored, respectively matrices operations with large data. The language is able to structure code in functions and results can be plotted in various ways. The version Matlab 2017b is used for both implementation and verification [17a].

4.1.2 PyCharm

The integrated development environment PyCharm from JetBrains is used to gather real distance data out of a ToF camera using the programming language Phyton. The software version PyCharm 2017.3 is used [17c].

4.1.3 Time-of-Flight imaging platform

The chosen ToF platform from Infineon to verify the model against real data contains the sensor IRS1645C. It features a resolution of 224 x 172 pixels, which sums up in 38 k pixels in total.

Figure 4.1 shows the hardware platform, called Bringup platform. One is the camera adapter board and the other one the CX3 host. On the camera adapter board the sensor is placed behind the lens (blue). Below the lens is the illumination located which is a VCSEL (white). The connection to the PC is performed with the USB 3.0 Micro B interface.

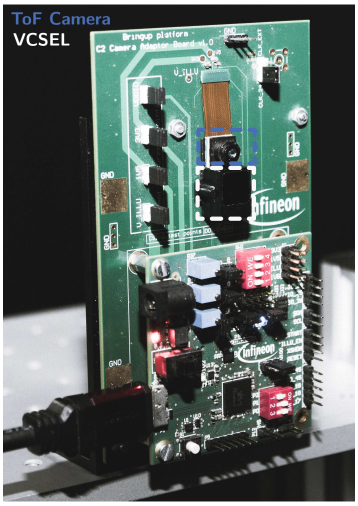

Figure 4.1: The selected ToF hardware platform. The illumination unit is a VCSEL and the blue marked camera shows the lens where the pixel array is located behind it.

4.2 Time-of-Flight model

This section provides a detailed description of all processing units which are characterized as functions and the data container having constants and parameters stored.

4.2.1 Data containers

Variables used as parameters or return values of functions, are grouped into structured arrays to encapsulate them and to get a better overview. Structured arrays contain fields that can be of any data type. In this section constants and parameters are outlined while the upcoming sections show functions with their used parameters and return values either in structured array form or not.

4.2.1.1 Physical constants *pc*

Field	Unit	Description
k	$\frac{J}{K}$	The Boltzmann constant of $1.38 \cdot e^{-23}$ $\frac{J}{K}$.
e	C	The elementary charge of $1.602176565 \cdot e^{-19}$ C.
c	$\frac{m}{s}$	Speed of light in vacuum of 299792458 $\frac{m}{s}$.
K_m	$\frac{lm}{W}$	The luminous efficacy of radiation is a constant of 683 $\frac{lm}{W}$.
h	Js	The Planck constant of $6.62606979 \cdot e^{-34}$ Js.

Table 4.1: The physical constants.

4.2.1.2 Illumination *illu*

Parameters that belong to the illumination unit, like a VCSEL or LED, are shown in Table 4.2.

Field	**Unit**	**Description**
FoV	°	The Field of View of the illumination unit. When providing a scalar value it is interpreted to be the diagonal FoV. The output power is here projected on a circular object shape. Using a row vector with two elements (2x1) the first value is interpreted as horizontal and the second one as vertical FoV resulting in a rectangular object shape.
Φ_{eIllu}	W	Peak output power of the illumination unit.
λ	m	The wavelength that is used by the illumination unit. It is used in this function as one parameter for filtering the background light spectrum.

Table 4.2: The parameters of the illumination unit.

4.2.1.3 Scene parameters *scene*

One major parameter of the scene is the sweep parameter where one specifies the focus of a simulation run. Each sweep configuration has a relating *from* and *to* parameter. A vector with values between these two parameters is generated. When selecting a sweep configuration the nominal values of the other sweep options are taken. The resulting values are stored in the same structure *scene* in *d*, *E_v* and *t_integration*.

Field	**Unit**	**Description**
sweep	–	The following sweep configurations are possible: Distance, Background light, Integration time.
samples	–	The number of samples of either *d*, *E_v* or *t_integration* depending on the sweep configuration.
distanceNominal	m	The target distance is the distance between the illumination unit, which can either be an LED or a VCSEL, and an object. It equals the distance between the camera and the same object. It is only used in the sweep configurations *Background light* and *Integration time*.
distanceFrom	m	The starting distance of *Distance* sweep.

distanceTo	m	The end point distance of *Distance* sweep.
E_vNominal	lx	The nominal background illuminance is only used in the sweep configurations *Distance* and *Integration time*.
E_vFrom	lx	The lowest illuminance of *Background light* sweep.
E_vTo	lx	The maximum illuminance of *Background light* sweep.
t_integrationNominal	s	The integration time is a synonym for the illumination time. The nominal integration time is only used in the sweep configurations *Distance* and *Background light*.
t_integrationFrom	s	The starting integration time of *Integration time* sweep.
t_integrationTo	s	The end integration time of *Integration time* sweep.
backgroundSel	–	The selection of the background light source. The following string values are acceptable: • sunlight[1] • halogen • incandescent • fluorescent
p	–	Reflection factor of the object in the scene. The value can be adjusted between zero and one where zero means total absorption and one total reflection.
filter	nm	The filter parameter acts as lower and upper bound for an optical rectangular band-pass filter. wavelengths which are out of the region $\lambda - filter$ to $\lambda + filter$ are filtered out of the spectrum. The integration in Equation 3.3 is then not performed from 0 to ∞ but using the specified region as limits. The filter can be disabled when setting it to zero.

Table 4.3: Parameters relating to the scene.

---

[1] The sunlight spectrum values are taken from Reference Solar Spectral Irradiance: ASTM G-173 `http://rredc.nrel.gov/solar/spectra/am1.5/ASTMG173/ASTMG173.html` (visited on 08/22/2017) global tilt column of the table.

4.2.1.4 Camera parameters *camera*

Parameters that belong to the camera unit of the ToF sensor are shown in Table 4.4. It contains lens parameters, the FoV, sensor dimension, FF and pixel pitch. Latter is the distance from the center of one pixel to another.

Field	**Unit**	**Description**
k_lens	–	A loss factor of the lens between zero and one. A value of one means no losses, zero total losses.
f_number	–	The f number of the lens.
foV	°	The Field of View of the camera. When providing a scalar value it is interpreted to be the diagonal FoV relating to a circle in the scene. Using a row vector with two elements (2x1) the first value is interpreted as horizontal and the second one as vertical FoV resulting in a rectangular shape.
dimensionOpticalAreaX	m	The horizontal dimension of the optical sensitive part of the sensor.
dimensionOpticalAreaY	m	The vertical dimension of the optical sensitive part of the sensor.
pixel_pitch_x	m	Horizontal pixel pitch.
pixel_pitch_y	m	Vertical pixel pitch.
FF	–	Fill factor with or without micro lenses. The value can be between zero and one where one means that all incoming light reaches the pixel and zero none.

Table 4.4: Parameters relating to the camera.

4.2.1.5 Pixel parameters *pixel*

Table 4.5 shows parameters which belong to the internal PMD pixel.

Field	Unit	Description
iterations	–	The number of iterations relate to the noise model and their calculation. A high number gives a precise result for the standard deviation calculation but increases computation time.
T	°	The ambient temperature. In the model it gets converted into kelvin.
photo_responsivity	$\frac{A}{W}$	Spectral responsivity. It is used to calculate the quantum efficiency to determine how many electron-hole pairs are generated out of the incoming photons.
contrastDemod	%	The value of the demodulation contrast can be between zero and 100%. A value of 100% means that all generated electrons are distributed according to their distance.
C_diode	F	The capacitance of the 4-transistor circuit consisting of the diode's capacitance.
C_sampleAndHold	F	The capacitance of the 4-transistor circuit consisting of the parasitic capacitance.
n_subFrames	–	The number of phases regarding the ToF phase algorithm (default 4).
v_reset	V	The reset voltage level of the 4-transistor circuit. The integration process will start from this voltage.
v_saturated	V	The saturation voltage level which belongs to the SBI threshold voltage. A pixel is saturated when reaching this value (without SBI enabled).
enableSBI	–	A value unequal to zero enables the SBI module.
dark_slope_se_mean	$\frac{mV}{ms}$	The single ended mean value of the dark slope. This value is temperature dependent.
dark_slope_se_sigma	$\frac{mV}{ms}$	One sigma of the single ended dark slope. This value is temperature dependent.

Table 4.5: Parameters relating to the PMD pixel.

4.2.1.6 Parameters of the illuminated waveform with nominal frequency *illuWave*

The parameters shown in Table 4.7 represent the outgoing waveform of the illumination unit. The specification of the illumination unit is described in Section 4.2.1.2.

Field	Unit	Description
waveForm	–	The following waveforms can be generated: • sine • pulse • fourier series (absolute values) • gauss extended • sawtooth • triangle A representation of the waveforms is given in Figure 4.2.
fourierOrder	–	The order of the fourier series whichs results in the first harmonic and *fourierOrder*-1 harmonics.
gaussOrder	–	The order of the extended gauss waveform generation. The higher the order is the more it becomes a square.
dutyCycle	%	The duty cycle of the waveform can be between 0 to 100%. Usually, a value of $\leq 50\%$ is appropriate.
f_mod	Hz	The modulation frequency of the illuminated signal (default 80.32 MHz).
unambiguityRange	m	The maximum distinct distance. It gets calculated in the model and is therefore not modifiable.
enableNoise	–	A value unequal to zero enables noise.

Table 4.6: Parameters of the illuminated waveform.

4.2.1.7 Parameters of the internal reference waveform *refWave*

Field	Unit	Description
waveForm	–	The following waveforms can be generated, Figure 4.2. • sine • pulse • fourier series (absolute values) • gauss extended • sawtooth • triangle
fourierOrder	–	The order of the fourier series whichs results in the first harmonic and *fourierOrder*-1 harmonics.
gaussOrder	–	The order of the extended gauss waveform generation. The higher the order is the more it becomes a square.
dutyCycle	%	The duty cycle of the waveform can be between 0 to 100%. Usually, a value of 50% is appropriate.

Table 4.7: Parameters of the reference waveform.

4.2.1.8 Parameters of the analogue digital converter *adc*

The voltage levels *VrefPos* and *VrefNeg* represent the FSR of the ADC.

Field	Unit	Description
VrefPos	V	Positive reference voltage.
VrefNeg	V	Negative reference voltage.
resolution	bits	The resolution in number of bits.
offset_error	LSB	Offset error.
gain_error_percent	% of FSR	Gain error.
integral_nonlinearity	LSB	Integral non-linearity error.
differential_nonlinearity	% LSB	Differential non-linearity error.

Table 4.8: Parameters of the analog digital converter.

4.2.1.9 Parameters for visualization *plots*

The following Boolean parameters are used to determine which plots should be generated. A value unequal to zero enables a parameter. The parameters *DistUnambiguity*, *DistRealDist* and *Wiggling* are only usable in the sweep configuration *Distance*.

Field	**Description**
CC	The voltages of the cross correlation function are plotted. The x-axis belongs to the sweep configuration. Using a four phase algorithm leads to a plot of four voltages.
PTC	The photon transfer curve including all noise sources is plotted.
SNR	Plots the Signal-to-Noise Ratio in decibel.
Amplitudes	The amplitude is plotted. The x-axis belongs to the sweep configuration.
DistNoise	Plots the distance noise. The x-axis belongs to the sweep configuration.
DistUnambiguity	The calculated distance over the real distance without correction of the unambiguity range is plotted.
DistRealDist	The calculated distance over the real distance is plotted including a phase unwrap to solve the unambiguity problem.
Wiggling	Plots the mean of calculated distance minus real distance which is the absolute error.

Table 4.9: Parameters for visualization.

4.2.2 Probing function

The probing function calculates how much power of the illumination unit is distributed on the area of an object. The object is here characterized to be a planar area.

Input	**Fields**	**Description**
scene	d	See Section 4.2.1.3.
illu	FoV, Φ_{eIllu}	See Section 4.2.1.2.
Output	**Unit**	**Description**
E_{eScene}	$\frac{W}{m^2}$	Irradiance on the object in a scene which is power per area.

Table 4.10: Full description of the probing function.

4.2.3 Generate waveform

This function generates a time-discrete waveform in a defined timing windows of exactly one period. The peak value of the waveform is standardized to one. This does not fully apply when using the fourier series waveform. When using a small value as fourier order a wave with several sine harmonics will appear including a peak above one, using a high value results more in a square wave shape with a peak value of one. For the illumination unit the waveform should be a signal with a sharp edge, emitting the optical power immediately. Ideal would be a pulse shape which means full optical power when the wave is high and no optical power when it is zero. The waveform differs from the optimum due to the driver circuit and the LED or VCSEL itself. Therefore a set of different waveforms can be selected.

Input	**Unit**	**Description**
waveParams	–	Either *illuWave* or *refWave* can be entered here as parameter.
t	–	The time vector t gets multiplied by the percentage of the duty cycle of *waveParams* for the pulse duration and 100 - duty cycle for the pause of the duration. It is an abstract value and not in seconds.
phaseOffset	rad	The phase offset of the resulting waveform.
Output	**Unit**	**Description**
wave	–	The resulting wave in row vector form.

Table 4.11: Full description of the generate waveform function.

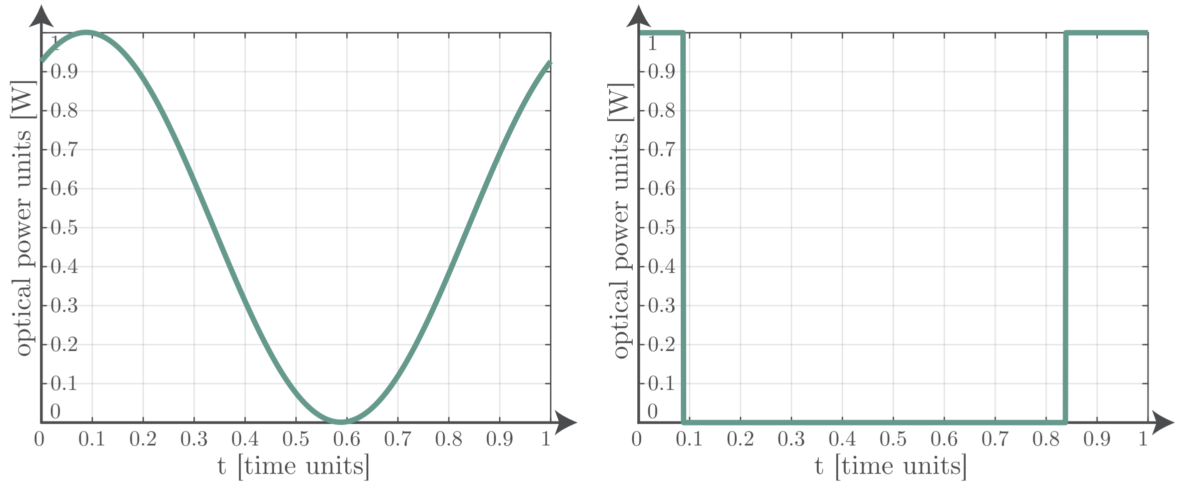

(a) Sine waveform.

(b) Pulse with 25% duty cycle.

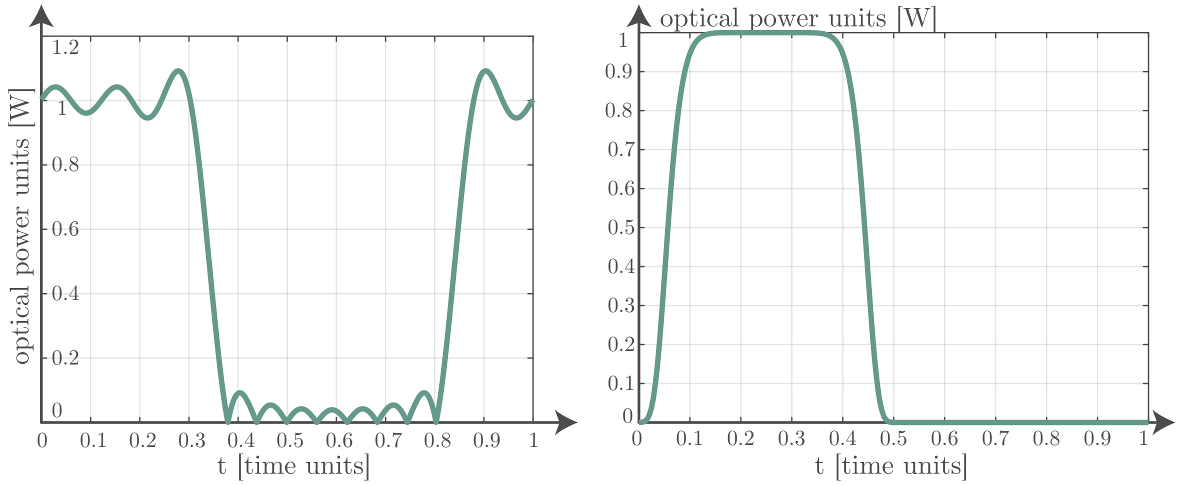

(c) A fourier series wave with absolute values having 4 harmonics.

(d) A Gauss shaped wave with a factor of 5.

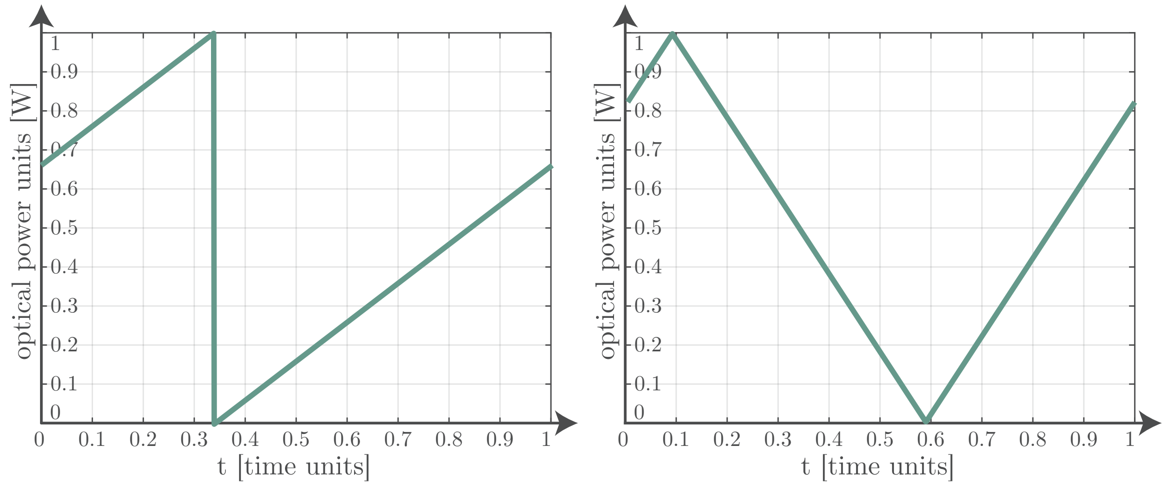

(e) Sawtooth waveform.

(f) Triangle waveform.

Figure 4.2: Generate able waveforms. All waveforms here have a phase shift of 45° except the gauss shaped one. The pulse has a 25% duty cycle. The y-axis belongs to optical power units which means that this value is later multiplied by the peak output power Φ_{eIllu}, which is a parameter of the model. The time units on the x-axis are units of one period in relation to the modulation frequency.

4.2.4 Background light

The background light function uses one of four different light sources, such as sunlight and calculates how much power per unit area falls on an object with a given background illuminance. The luminosity curve and the specific background light spectrum have to be taken into account. The background light spectrum is filtered around the wavelength λ to implement an optical filter of the ToF camera. Table 4.12 shows parameters and return values of the background light function. The implemented luminosity curve and the sunlight spectrum are shown in Figure 4.3.

Input	**Fields**	**Description**
illu	lambda	See Section 4.2.1.2.
scene	backgroundSel, filter, E_v	See Section 4.2.1.3.
pc	K_m	See Section 4.2.1.1.
Output	**Unit**	**Description**
$E_{eBackground}$	$\frac{W}{m^2}$	Irradiance on the object in the scene which is power per area.

Table 4.12: Full description of the background light function.

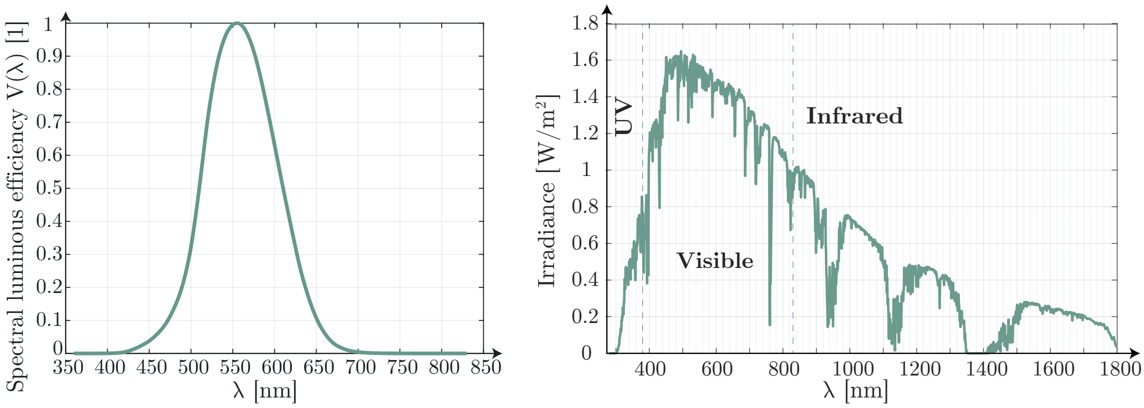

(a) Luminousity curve (photopic)[2]

(b) Sunlight spectrum

Figure 4.3: The spectral luminous efficiency $V(\lambda)$ describes the spectral brightness sensitivity of the human eye at daylight conditions (a) where λ is the wavelength of the electromagnetic radiation. It is the ratio $\frac{\Phi_e(\lambda_m)}{\Phi_e(\lambda)}$ where it equals to the maximum of 1 when $\lambda = \lambda_m$ [87b]. The curve belongs to Commission Internationale de l'Eclairage (CIE). The total power of the sun is spread over a large wavelength range (b) but the maximum irradiance lies in the visible light range.

---

[2] The values of the luminosity function were taken from `http://www.cvrl.org/lumindex.htm` (visited on 08/22/2017) section Other luminous efficiency functions - CIE (1924) Photopic $V(\lambda)$. The download option was "Button Plot lin E".

4.2.5 Calc lens parameters

This function calculates the focal length and lens diameter out of the field of view, sensor dimensions and the lens' f-number. Table 4.14 shows parameters and return values of the calc lens parameters function.

Input	**Fields**	**Description**
camera	foV, dimensionOpticalAreaX, dimensionOpticalAreaY, f_number	See Section 4.2.1.4.
Output	**Fields**	**Description**
lens	focalLength, D	A struct with these two parameters is generated.

Table 4.13: Full description of the calc lens parameters function.

4.2.6 Scene response function

The scene response function calculates the optical power impinging on a center pixel of the ToF camera. The function is called twice both for the emitted and the background irradiance which are outputs of the *probing* and *background light* function. The irradiance is reflected on the surface of an object which is assumed to be a planar area. Reflection is modeled with a lambert reflector. Table 4.14 shows parameters and return values of the scene response function.

Input	**Fields**	**Description**
E_e	–	Irradiance on the object in the scene in W/m^2. E_{eScene} has its origin in the illumination of the ToF camera and $E_{eBackground}$ from the background light.
scene	d, p	See Section 4.2.1.3.
camera	pixel_pitch_x, pixel_pitch_y, FF, k_lens	See Section 4.2.1.4.
lens	focalLength, D	See Section 4.2.5.
Output	**Unit**	**Description**
Φ_e	W	Optical power on one pixel (the center pixel).

Table 4.14: Full description of the scene response function.

4.2.7 Power to photons

This function is called twice both for the radiant flux of the scene which has its origin in emitting an optical signal and the background. Radiant flux is converted into a number of photons that hit the pixel of the camera. Table 4.15 shows parameters and return values of the power to photons function.

Input	**Fields**	**Description**
pc	c, h	See Section 4.2.1.1.
scene	t_integration	See Section 4.2.1.3.
illu	lambda	See Section 4.2.1.2.
Φ_e	-	Optical power in W on one pixel (the center pixel) originated from the illumination unit or the background light.
Output	**Unit**	**Description**
$n_{photons}$	-	The number of photons which hit the pixel according to the optical scene and background power.

Table 4.15: Full description of the power to photons function.

4.2.8 Photons to electrons

Impinging photons generate electron-hole pairs in the light-sensitive part of the PMD. The number of electrons is calculated out of the number of photons. The function stores three fields in the structured array *n_electrons*. Table 4.16 shows parameters and return values of the power to photons function.

Input	**Fields**	**Description**
pc	h, c, e	See Section 4.2.1.1.
camera	FF	See Section 4.2.1.4.
illu	lambda	See Section 4.2.1.2.
pixel	photo_responsivity, contrastDemod	See Section 4.2.1.5.
n_photons	scene, background	See Section 4.2.7.
Output	**Fields**	**Description**
n_electrons	equallyDistributed, distanceDistribution, sum	The number of electrons which are equally distributed on the two taps A and B is *n_electrons.equallyDistributed*. The number refers to one tap and depends on quantum efficiency and background light. Electrons which get distributed according to the corresponding distance are stored in *n_electrons.distanceDistribution* and the sum of electrons produced inside the PMD is *n_electrons.sum*.

Table 4.16: Full description of the photon to electrons function.

4.2.9 Sensor response function

The sensor response function models the major functionality of a PMD, which is the opto-electronic mixing. In this model a reference waveform r is generated by the function *Generate waveform*. It uses the structured array *refWave*. The reference pulse has always a phase offset of zero degrees and does not change over integration time. The distances of the vector *scene.d* are converted into phases that are then internally stored to *phi_reflected*. The resulting phase offset of the reflected wave consists of *phi_reflected*, the current sub frame phase (e.g. 90° of the 4-phase measurement setup) and a phase offset according to the duty cycle. Having a duty cycle of zero would lead to no additional phase shift. When using a duty cycle of 25% the additional phase offset applied is 45° to center the on-time of the reflected waveform in the center of the on-time of the reference wave. When not applying this phase offset a phase shift in the final calculated distance can be observed.

Table 4.17 shows the generation of the reflected signal s and how it is mixed with the reference signal r. The mixing is equivalent to a cross correlation, see Equation 3.24 but is done only for one period. It is not performed for all periods to save computation time. The mixing process has to be applied for both taps A and B. The value n_subframes belongs to the number of emitted phases. In a four-phase measurement it would have the value four. n_distances is the size of the distance vector. The final values for the number of integrated electrons of one period are stored in n_eA and n_eB.

```
for subFrame = 1 : n_subFrames
  for phaseIndex = 1 : n_distances
    %% waveform generation of s
    phaseOffset = - phi_reflected(1, phaseIndex) -  pixel.
   phi_phase_vector(:, subFrame) - phaseShiftCenterSInR;
    s = generate_waveform(emittedSigParams, t_s, phaseOffset);

    %% Tap A
    A = (r .* s );
    A_integ = A .* n_ePerPeriod(:, phaseIndex);
    integ =  cumtrapz(t, A_integ);
    n_eA(subFrame, phaseIndex) = integ(end);

    %% Tap B
    B = s - r .* s;
    B_integ = B .* n_ePerPeriod(:, phaseIndex);
    integ =  cumtrapz(t, B_integ);
    n_eB(subFrame, phaseIndex) = integ(end);
  end
end

```

Table 4.17: The PMD mixing process of the reference and reflected wave.

After the mixing process the SBI behaviour is applied when enabling it with *enableSBI* and pixel saturation is performed.

As a next step the noise model is applied to the integrated number of electrons. In order to do this, the different noise sources that have already have been discussed in Section 3.2.3 are calculated in number of noise electrons and combined with the number of integrated electrons over all periods. This calculation is done *iteration* times and the result is converted from a number of electrons to a voltage in the matrix *V_integrated*.

The function returns the integrated voltages for all sub frames including noise and pixel saturation. Additionally, the number of signal electrons as well as the number of electrons for the noise sources are stored. Table 4.18 shows parameters and return values of the sensor response function.

Input	**Fields**	**Description**
pc	e, c	See Section 4.2.1.1.
pixel	v_reset, v_saturated, C_integration, phi_phase_vector, enableSBI, iterations, C_sampleAndHold, n_subFrames	See Section 4.2.1.5.
scene	t_integration, d, samples	See Section 4.2.1.3.
n_electrons	equallyDistributed, distanceDistribution, sum	See Section 4.2.8.
refSigParams	dutyCycle	See Section 4.2.1.7.
emittedSigParams	f_mod, dutyCycle, enableNoise	See Section 4.2.1.6.
Output	**Fields**	**Description**
$V_{integrated}$	-	The integrated voltage in V including noise when *enableNoise* is enabled.
$pixelSaturationAB$	-	This matrix contains a zero when a pixel is saturated else one.
n_electrons	signal, resetNoise, holdNoise, photonShotNoise, darkShotNoise, readNoise	The number of signal and noise electrons.

Table 4.18: Full description of the sensor response function.

4.2.10 Suppression of background illumination

The function uses the two inputs n_{e-A} and n_{e-B} to calculate whether one of them reaches the saturation level $n_{e-SatThreshold}$ after $n_{periods}$. Figure 3.13 shows the behavior. The one that reaches the level earlier than the other one stays at that level. The time where it reaches that level is calculated. From this point in time the other input is integrated in positive direction with a different slope than the down integration. When the integration goes beyond the reset level $n_{e-Reset}$ it is set to this maximum. When this happens the pixel is saturated as the first level is at the lower bound and the second one at the upper bound. The function *pixel saturation* is used to fulfill this criteria.

The outputs of the function are the adjusted number of electrons $n_{e-A-SBI}$ and $n_{e-B-SBI}$ and the pixel saturation matrix. Table 4.19 shows parameters and return values of the SBI function.

Input	**Description**
$n_{e-Reset}$	The number of electrons according to the reset voltage V_{reset}.
$n_{e-SatThreshold}$	The number of electrons according to the saturation voltage $V_{saturation}$.
$n_{periods}$	The number of periods is gathered by multiplying the modulation frequency f_{mod} with $t_{integration}$.
n_{e-A}	The number of electrons which where integrated in tap A for one period of time.
n_{e-B}	The number of electrons which where integrated in tap B for one period of time.
$n_{e-EquallyDistributedOnePeriod}$	The number of electrons equally distributed in one tap of one period. This value depends on quantum efficiency and background light.
Output	**Description**
$n_{e-A-SBI}$	The adjusted number of electrons of tap A according to the SBI logic.
$n_{e-B-SBI}$	The adjusted number of electrons of tap B according to the SBI logic.
pixelSaturationAB	This matrix contains a zero when a pixel is saturated else one.

Table 4.19: Full description of the SBI function.

4.2.11 Pixel saturation

The pixel saturation differs when *enableSBI* is unequal to zero. The pixel saturation is applied for the number of electrons n_{e-A} and n_{e-B}. The lower number of electrons boundary is $n_{e-SatThreshold}$, the upper one is $n_{e-Reset}$. It outputs the limited number of electrons due to the boundaries in n_{e-ASat} and n_{e-BSat} as well as the pixel saturation matrix. Table 4.20 shows parameters and return values of the pixel saturation function.

When the SBI module is disabled saturation happens only when the electron levels of A / B reach the lower boundary of $n_{e-SatThreshold}$, see Figure 3.12. A different behavior occurs when SBI is enabled, shown in Figure 3.13. Here, a pixel saturates when one electron level is on $n_{e-SatThreshold}$ and the other one at $n_{e-Reset}$.

Input	**Description**
n_{e-A}	The number of electrons integrated over $t_{integration}$ in tap A over all periods.
n_{e-B}	The number of electrons integrated over $t_{integration}$ in tap B over all periods.
$n_{e-Reset}$	The number of electrons according to the reset voltage V_{reset}.
$n_{e-SatThreshold}$	The number of electrons according to the saturation voltage $V_{saturation}$.
enableSBI	A value unequal to zero leads to a different calculation with the SBI of the pixel saturation.
Output	**Description**
n_{e-ASat}	Saturated number of electrons of tap A.
n_{e-BSat}	Saturated number of electrons of tap A.
pixelSaturationAB	This matrix contains a zero when a pixel is saturated else one.

Table 4.20: Full description of the pixel saturation function.

4.2.12 kTC noise

The calculation is performed according to Section 2.4.2.2 using a Gaussian distribution. kTC noise is used to model reset and hold noise. Hold noise occurs in the source follower. Table 4.21 shows parameters and return values of the kTC noise function. The size of the output matrix is ($n_{subFrames}$ x $n_{samples}$ x iterations). Figure 4.4 shows kTC noise at ambient temperature of 25° and a capacitance of 14 fF. The size of the output is here chosen to be (1 x 1000) for one phase. The noise is calculated for each tap of the ToF sensor separately.

Input	**Fields**	**Description**
C	-	The capacitance in F where charges are stored.
scene	samples	See Section 4.2.1.3.
pc	k, e	See Section 4.2.1.1.
pixel	T, iterations	See Section 4.2.1.5.
Output	**Unit**	**Description**
$n_{e^-kTCNoise}$	1	Number of noise electrons.

Table 4.21: Full description of the kTC noise function.

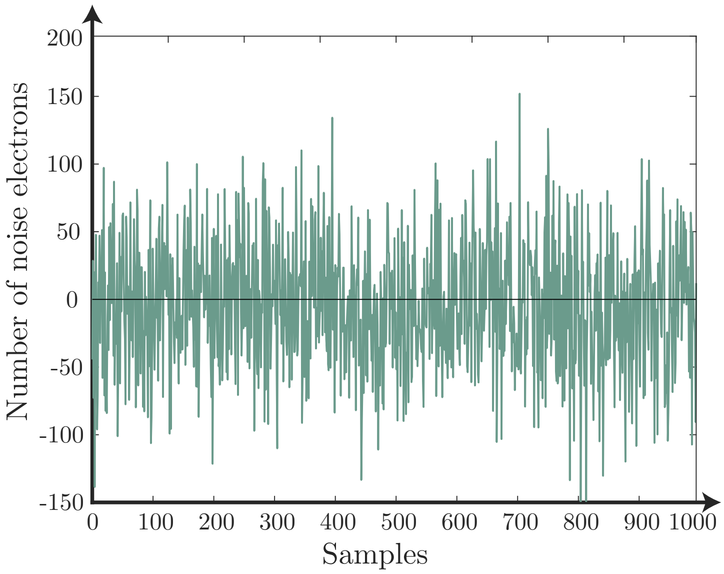

Figure 4.4: The kTC noise generated with a mean of zero (black line).

4.2.13 Photon shot noise

The calculation is performed according to Section 2.4.2.3. Table 4.22 shows parameters and return values of the photon shot noise function. The noise is calculated for each tap of the ToF sensor separately.

Input	**Fields**	**Description**
pixel	iterations, n_subFrames	See Section 4.2.1.5.
$n_{Integrated}$	–	The total number of integrated electrons.
Output		**Description**
$n_{e^-PhotonShotNoise}$	–	The number of photon shot noise electrons.

Table 4.22: Full description of the photon shot noise function.

The number of electrons correlates to the integration of electrons for on tap of the PMD. Photon shot noise can be seen in Figure 4.5. At small distances the noise is high and at large distances the noise is decreasing which has its reason in the square root of the integrated electrons. The mean value of zero is marked with a black line. Photon shot noise is modeled with a Gaussian distribution as it is typically an accurate approximation to a poisson distribution according to [Has14, p. 608]. The variance depends on the number of integrated electrons.

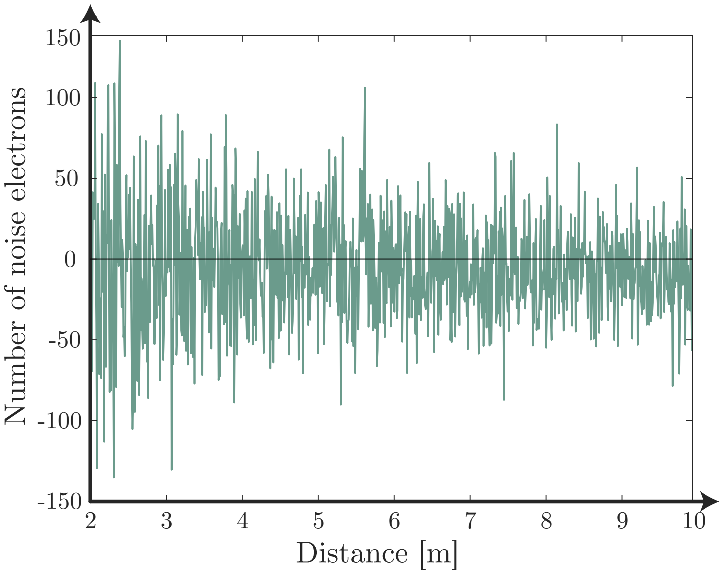

Figure 4.5: Photon shot noise of one tap with a mean of zero and a sigma with the square root of integrated electrons.

4.2.14 Dark current and dark current shot noise

The calculation is performed according to Section 2.4.2.4. Table 4.23 shows parameters and return values of the dark shot noise function. Figure 4.6 shows the behaviour of dark current shot noise modeled using a Gaussian distribution. In comparison to photon shot noise this noise does not depend on a number of electrons but on parameters like the temperature and the capacity of the integration capacitor. Furthermore, the mean is unequal to zero as dark current behaves like an offset. It shifts dark current shot noise, which is a noise source modeled with a mean of zero, towards the positive y-axis of noise electrons.

Input	**Fields**	**Description**
pc	e	See Section 4.2.1.1.
pixel	dark_slope_se_mean, dark_slope_se_sigma, C_integration, n_subFrames, iterations	See Section 4.2.1.5.
scene	t_integration, samples	See Section 4.2.1.3.
Output	**Unit**	**Description**
$n_{e^- DarkShotNoise}$	–	The number of dark shot noise electrons.

Table 4.23: Full description of the dark shot noise function.

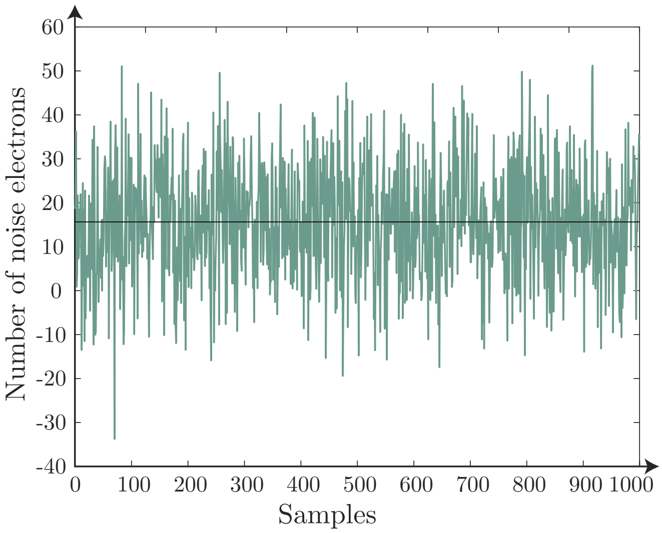

Figure 4.6: Dark current including dark shot noise with a mean of 15.6418 (black line) and a sigma of 13.2198 using a Gaussian distribution.

4.2.15 Analog digital conversion

The implementation of the ADC refers to Section 3.3.1. The input voltage is digitized to a raw value. The FSR is defined with the voltage difference of *VrefPos* and *VrefNeg*. The ADC errors offset, gain, integral non-linearity and differential non-linearity are implemented. ADC saturation is applied to the output *raw* value. The matrix *adcSaturation* contains a zero when all voltage values of a phase measurement have the maximum raw value of the ADC. Table 4.24 shows parameters and return values of the ADC function.

Input	**Fields**	**Description**
voltage	-	The integrated voltage in volts is the input for the ADC which has to be digitized.
adc	VrefPos, VrefNeg, resolution, offset_error, gain_error_percent, integral_nonlinearity, differential_nonlinearity	See Section 4.2.1.8.
Output	**Fields**	**Description**
modeled	raw, adcSaturationMatrix, rawMaxAdc	Three fields are added to the structured array. The parameter *raw* contains the raw values of the ADC, *adcSaturationMatrix* is a boolean matrix to store ADC saturation. The maximum raw value due to ADC errors is rawMaxAdc.

Table 4.24: Full description of the analogue to digital conversion function.

Figure 4.7 shows implemented ADC errors. On the left image, Figure 4.7(a), two curves are plotted, the ideal and the real quantisation characteristic. Latter includes offset, gain and integral non-linearity errors. These errors are first applied. A positive offset error is here applied as the curve is shifted via the x-axis to the left. The negative gain error can be seen in the slope difference and the integral error leads to a curved characteristic. Here, all errors are chosen far higher than they would be in a real application to see a difference in the plot. The last error, differential non-linearity, is applied at the end. This error leads to a variable width of the ADC stairs which map a voltage range to a fixed numerical value. The variable stair width is evenly distributed over the Full Scale Range. In Figure 4.7(b) it can be seen for an extract of the input range.

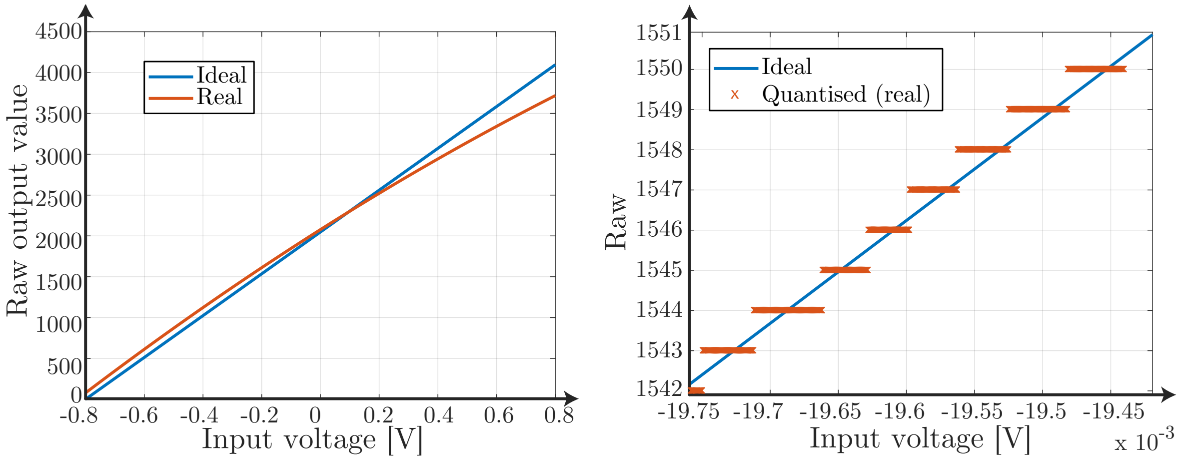

(a) (b)

Figure 4.7: The ideal versus the implemented ADC quantisation characteristic curve. Latter includes offset, gain and integral non-linearity errors (a). The differential non-linearity error is shown in (b).

4.2.16 Depth calculation

A distance is calculated with the help of Equation 2.2 and Equation 2.6 using raw values of the ADC. Speed of light and the respective modulation frequency is further necessary. A saturation matrix is used to set wrong measurements to a distance value of zero. Pixel and ADC saturation can happen, the matrix combines these two saturation origins. The calculated distance includes an offset that differs with the modulation frequency. Furthermore, the amplitude is calculated as well as the phase unwrapped to circumvent the unambiguity problem.

Input	**Fields**	**Description**
pc	c	See Section 4.2.1.1.
scene	d	See Section 4.2.1.3.
signalParams	f_mod	See Section 4.2.1.6.
modeled	raw, saturation	See Section 4.2.15 and 4.2.11.
Output	**Fields**	**Description**
modeled	distMOffset, amplitude, distMUnwrappedOffset	The calculated distance which is a synonym for depth including an offset represents the field *distMOffset*, the one with unwrapped phase is *distMUnwrappedOffset*. The field *amplitude* contains amplitude values in raw data format.

Table 4.25: Full description of the distance calculation function.

4.2.17 Plot results

This function generates various plots of gathered simulated data. It uses the calculated distance (depth), number of electrons regarding signal and noise and simulation parameters for visualization. For each plot there is a boolean switch whether to show it or not. Furthermore, the possibility to show a plot belongs to the sweep configuration. Table 4.26 shows parameters and return values of the plot results function.

Input	**Fields**	**Description**
scene	sweep, d, t_integration, E_v	See Section 4.2.1.3.
pixel	n_subFrames	See Section 4.2.1.5.
illuWave	f_mod, unambiguityRange	See Section 4.2.1.6.
modeled	distMOffset, distMUnwrappedOffset, amplitude	See Section 4.2.16.
n_electrons	signal, resetNoise, holdNoise, photonShotNoise, darkShotNoise, readNoise	See Section 4.2.9.
V_integrated	–	See Section 4.2.9.
plots	–	All boolean parameters are used according to Section 4.2.1.9.

Table 4.26: Full description of the plot results function.

4.3 Graphical user interface

The implemented GUI can be seen in Figure 4.8 to 4.11. The first figure shows the main tab when starting the app. Here, the background light and the sweep configuration can be selected. The following sweep configurations are available:

- Distance
- Background light
- Integration time

When selecting a sweep its corresponding parameters are taken from the two boxes *from* and *to* while from the unused sweep configurations the *nominal* values are taken. The number of iterations is a matter of precision regarding the noise level. On the right side a set of checkboxes are available where the necessary result plots can be ticked. Ones that do not relate to the selected sweep configuration are deactivated. The simulation is started when pressing the *Calculate* button, then the ready lamp turns into red and back to green again when it is finished. The simulation time gives information how long the simulation took which primarily depends on the number of iterations and the number of samples. This means when selecting the distance sweep for example, it will generate as many distances between the *from* and *to* distance as set in *Samples* and will repeat the noise calculation *Iteration* times.

In Figure 4.9, pixel related parameters can be adjusted. The parameters are limited to define a valid range. Switches guarantee that SBI and noise can be activated or deactivated. The phase measurement algorithm can be changed between two to five phases. An important factor is the ambient temperature. The waveform and the duty cycle of the illumination signal and the internal reference signal has to be chosen. By default a Gaussian waveform with 50% duty cycle is used for both signals only varying in the Gauss order. Another important parameter is the modulation frequency of the illumination signal.

Scene and camera related parameters are visible in Figure 4.10. On the left side is the FoV for the illumination signal and on the right side the one for the camera according to the lens. They are differentiated in order to simulate manufacturer-dependent deviations between these two FoVs. With a switch on the top, a diagonal FoV can be changed to a horizontal / vertical one and vice versa. When using a diagonal FoV the probing function calculates its emitting power on a circular object else on a rectangular object. Focal length and lens diameter are calculated out of the f number and the optical dimension area of the sensor. The lens parameters are always calculated with the diagonal FoV. For the illumination FoV a graphical representation is given on the bottom where the black dot is a point light source. Changing the optical power value also changes the y-axis of the illumination signal, shown in Figure 4.9 on the bottom right.

Figure 4.11 represents the last tab showing the physical constants and ADC parameters. On the right side the parameters of the ADC can be changed. The errors integral non-linearity, differential non-linearity and offset can be adapted in number of LSBs while the gain error is given in percent of FSR.

The generated plots always have the same figure number and they do not close automatically.

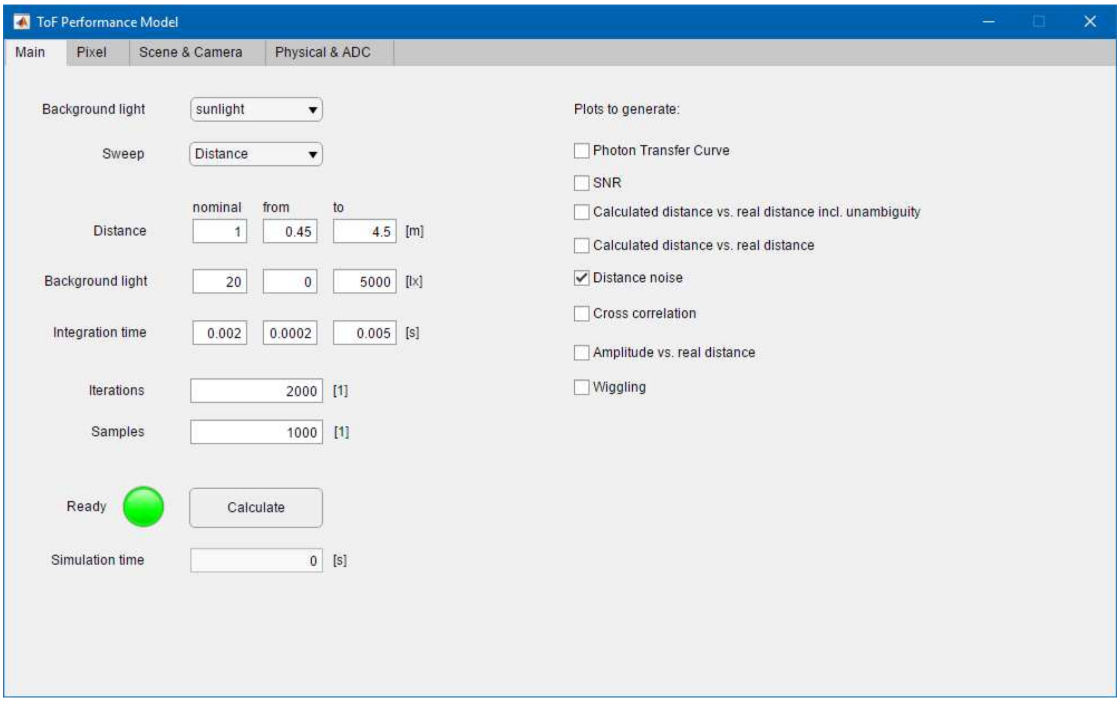

Background light: sunlight

Sweep: Distance

	nominal	from	to	
Distance	1	0.45	4.5	[m]
Background light	20	0	5000	[lx]
Integration time	0.002	0.0002	0.005	[s]

Iterations 2000 [1]

Samples 1000 [1]

Ready ●

Simulation time 0 [s]

Plots to generate:

- ☐ Photon Transfer Curve
- ☐ SNR
- ☐ Calculated distance vs. real distance incl. unambiguity
- ☐ Calculated distance vs. real distance
- ☑ Distance noise
- ☐ Cross correlation
- ☐ Amplitude vs. real distance
- ☐ Wiggling

Figure 4.8: Entry tab of the GUI where the simulation can be started.

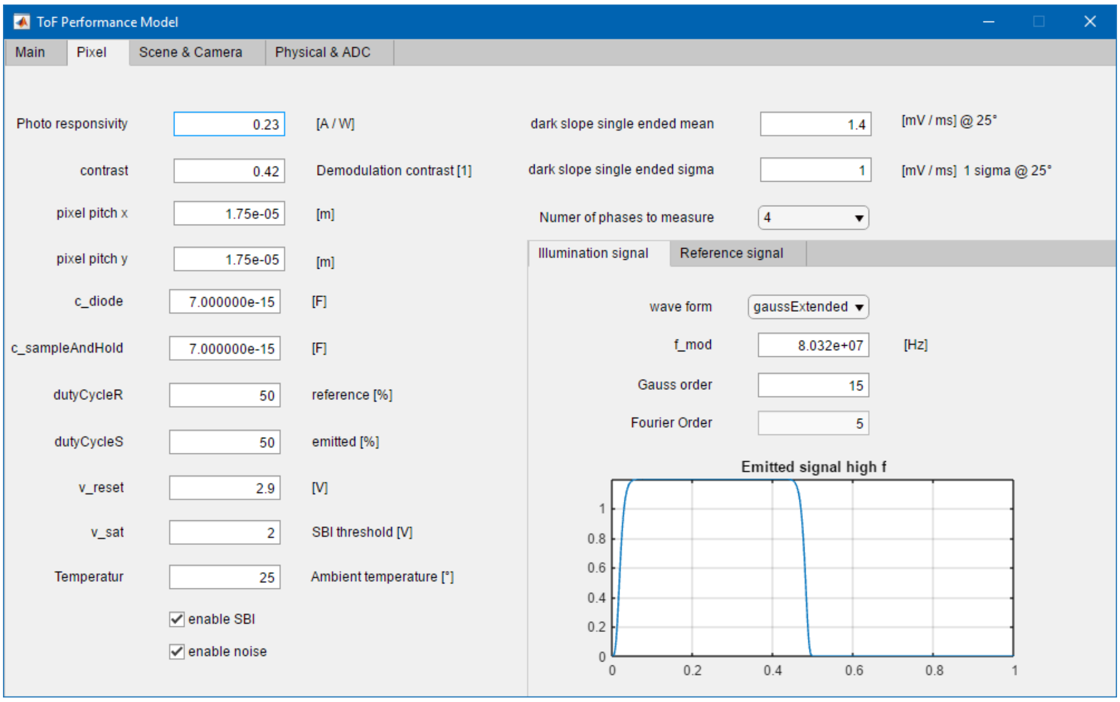

Photo responsivity 0.23 [A / W]

contrast 0.42 Demodulation contrast [1]

pixel pitch x 1.75e-05 [m]

pixel pitch y 1.75e-05 [m]

c_diode 7.000000e-15 [F]

c_sampleAndHold 7.000000e-15 [F]

dutyCycleR 50 reference [%]

dutyCycleS 50 emitted [%]

v_reset 2.9 [V]

v_sat 2 SBI threshold [V]

Temperatur 25 Ambient temperature [°]

☑ enable SBI

☑ enable noise

dark slope single ended mean 1.4 [mV / ms] @ 25°

dark slope single ended sigma 1 [mV / ms] 1 sigma @ 25°

Numer of phases to measure 4

wave form gaussExtended

f_mod 8.032e+07 [Hz]

Gauss order 15

Fourier Order 5

Figure 4.9: All parameters relating to the pixel of the ToF camera are listed here as well as the illumination and reference signal.

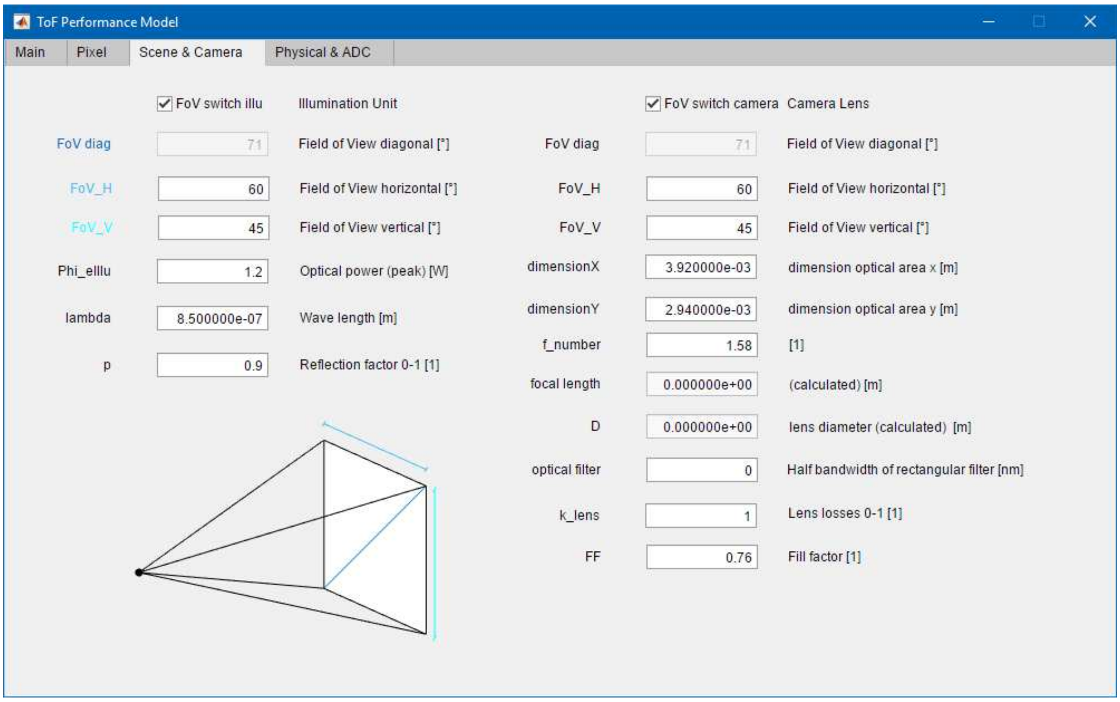

☑ FoV switch illu — Illumination Unit

FoV diag	71	Field of View diagonal [°]
FoV_H	60	Field of View horizontal [°]
FoV_V	45	Field of View vertical [°]
Phi_elllu	1.2	Optical power (peak) [W]
lambda	8.500000e-07	Wave length [m]
p	0.9	Reflection factor 0-1 [1]

☑ FoV switch camera — Camera Lens

FoV diag	71	Field of View diagonal [°]
FoV_H	60	Field of View horizontal [°]
FoV_V	45	Field of View vertical [°]
dimensionX	3.920000e-03	dimension optical area x [m]
dimensionY	2.940000e-03	dimension optical area y [m]
f_number	1.58	[1]
focal length	0.000000e+00	(calculated) [m]
D	0.000000e+00	lens diameter (calculated) [m]
optical filter	0	Half bandwidth of rectangular filter [nm]
k_lens	1	Lens losses 0-1 [1]
FF	0.76	Fill factor [1]

Figure 4.10: Scene and camera related parameters like the FoV are adjusted in this tab.

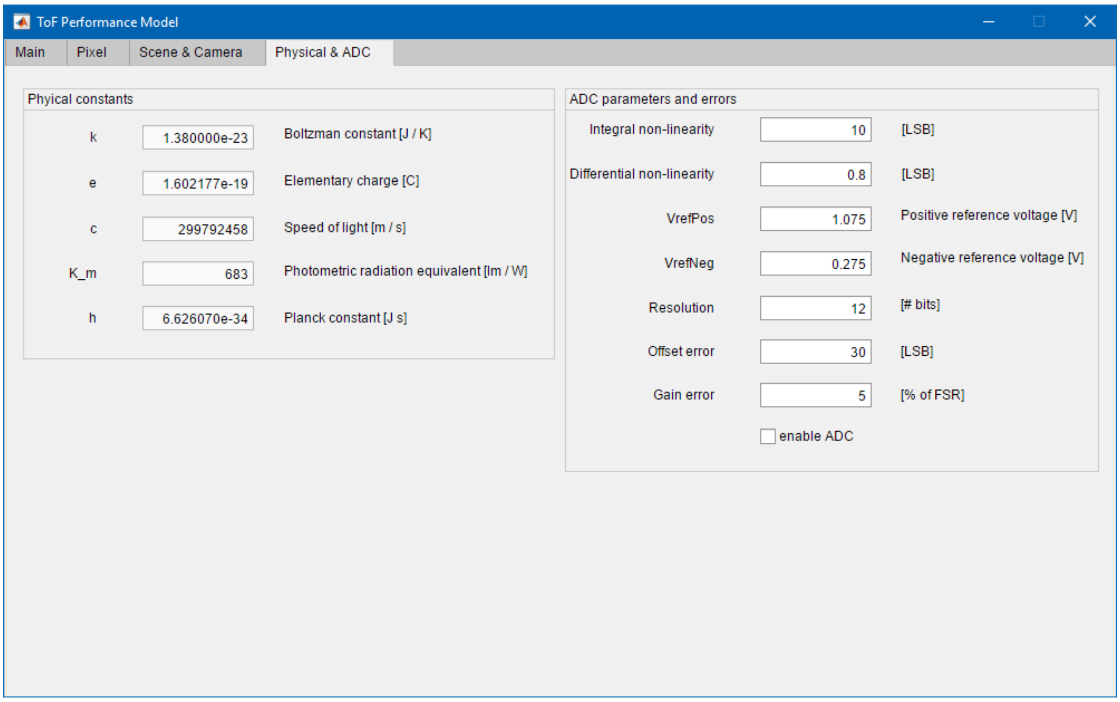

Phyical constants

k	1.380000e-23	Boltzman constant [J / K]
e	1.602177e-19	Elementary charge [C]
c	299792458	Speed of light [m / s]
K_m	683	Photometric radiation equivalent [lm / W]
h	6.626070e-34	Planck constant [J s]

ADC parameters and errors

Integral non-linearity	10	[LSB]
Differential non-linearity	0.8	[LSB]
VrefPos	1.075	Positive reference voltage [V]
VrefNeg	0.275	Negative reference voltage [V]
Resolution	12	[# bits]
Offset error	30	[LSB]
Gain error	5	[% of FSR]

☐ enable ADC

Figure 4.11: The fourth tab relates to physical constants and parameters of the ADC.

4.4 Verification

This section describes which steps are taken to gather data from the ToF sensor and compare them with results of the model.

4.4.1 Gathering data

The class Wiggling of the Python project was extended to a Comma-separated values (CSV) export and amplitude calculation. Depth measurement results are packed together. Furthermore, functions are written to enable a sweep over integration time. It works in a way that the distance to the target is held constant. Several depth pictures are taken, then the integration time of the sensor increased until a specified limit is reached. All results belong to a center pixel. Before data is gathered from the ToF camera it is configured to use a 4 phase measurement setup with 2 ms exposure time, 5 Frames Per Second (FPS) and 25% duty cycle of the illumination signal. The registers of the ToF sensor, which were modified are listed in Table A.1. The table shows the configuration for the sweep over distance.

4.4.2 Analysis of LTS data

This function analyses real data of the LTS and compares it to data of the model. Input parameters of the model are the calculated distance, real distance and the unambiguity range that belongs to the chosen modulation frequency. Data from the LTS are provided in CSV format and include the real distance.

First of all the calculated distance data is plotted over the real distance data from the LTS including a mean line. Other plots compare the amplitude in absolute values and distance noise in relative values. Table 4.27 shows parameters and return values of the analyse LTS data function.

Input	**Fields**	**Description**
pc	c	See Section 4.2.1.1.
scene	d	See Section 4.2.1.3.
illuWave	f_mod	See Section 4.2.1.6.
modeled	distMOffset, distMUnwrappedOffset, amplitude	See Section 4.2.16.
pathToFiles	-	The path to the measured data with the LTS in CSV format.

Table 4.27: Full description of the analyze LTS data function.

Chapter 5

Results

The results of the implemented model are presented in this chapter as well as the verification against real data. When not otherwise stated, the default parameters of the model are used.

5.1 Noise behavior

The introduction of the model results starts with a closer look at the noise sources. Figure 5.1 shows one out of the four integrated noise voltages over the integration time when using a 4-phase measurement setup. The difference of the voltages between tap A and B is calculated, noise applied and then the standard deviation performed. The noise voltage is gathered from this standard deviation calculation over multiple iterations. There is only one voltage visible, as it also represents the others. The sweep starts from 0 ms, which means that no illumination happens, there is already a noise voltage present due to dark current. It refers to dark noise which is independent of integration time. The curve can be split into three parts. In the beginning at small integration times read noise is dominant. Then from certain integration times on, noise starts to be dominated by photon shot noise which is represented by the majority of the figure, showing the root behavior as shot noise increases with the square of incoming photons. The third part shows an increase in the slope of the curve due to additional noise sources caused by the SBI.

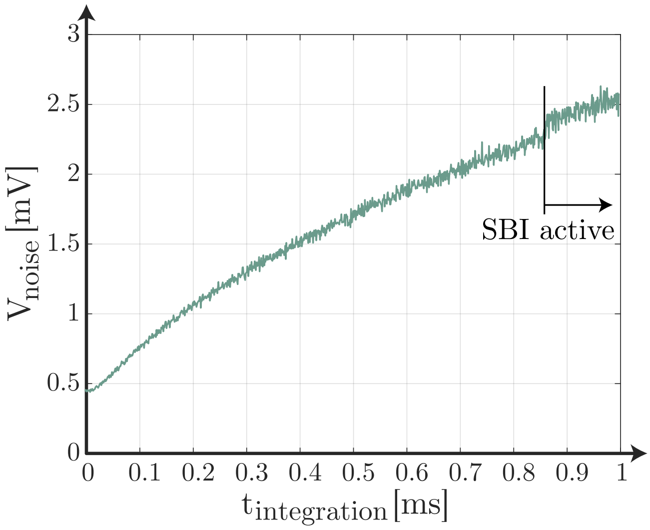

Figure 5.1: Voltage noise with respect to integration time.

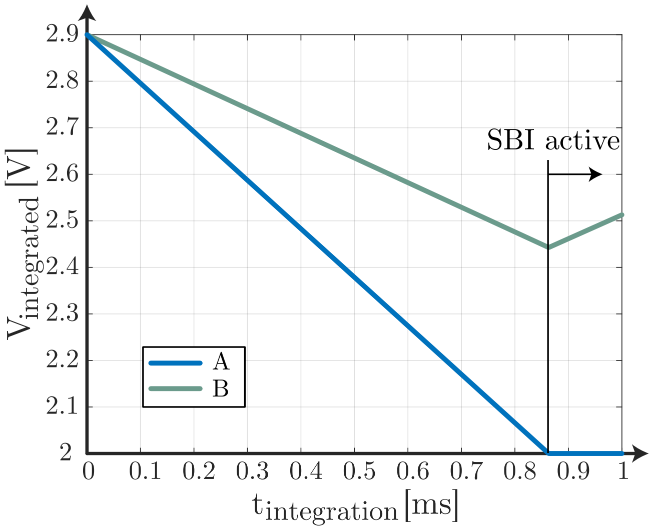

Figure 5.2: Integrated voltages of tap A and B over integration time.

SBI is more closely examined with Figure 5.2. It shows the integrated voltage of the 0° phase over the integration time. The distance was set to 1 meter and a high background light value as well as optical illumination power was chosen. Each sample in the figure shows the completed integration process of the two taps. This means the following: In the reset phase the capacitor is charged to V_{reset} and in the illumination phase charges are collected, a current flows and the capacitors of A and B are discharged. When looking for example at 0.5 ms, the final integrated voltage of A is 2.379 V and of B is 2.635 V. At a specific integration time the SBI starts to get active. This happens when one integrated voltage, here A, has reached the saturation voltage $V_{saturated}$. The other voltage gets integrated in positive direction from this point in time, meaning that the inverted current of A is added to B. This works until B has reached the upper voltage limit V_{reset}.

5.2 Cross correlation

The theoretical cross correlation of a rectangular shaped illumination and reference signal according to literature is already illustrated in Figure 2.6(b) resulting in a triangle cross correlation.

Figure 5.3(a) shows the cross correlation of the model. These signals are input values for the ADC. The default values of the model use a 4-phase measurement setup. That is why four different curves appear here. The integrated voltages are plotted over the distance. The distance is chosen to start from 1.87 to 5 meters. At the start distance the violet and orange signals are zero, the blue one is at maximum and the yellow one at minimum. The x-axis directly correlates with the phase. Here, distances are shown instead of phases for better visualization. The modulation frequency of 80 MHz can also be seen in the figure as the unambiguity range can be derived from it; which is 1.875 m and illustrated for the 270° phase measurement in violet. More details for the unambiguity range are found in Section 2.2. The trend of these signals is not perfect triangular shaped. The reason is, that the number of incoming photons and so the

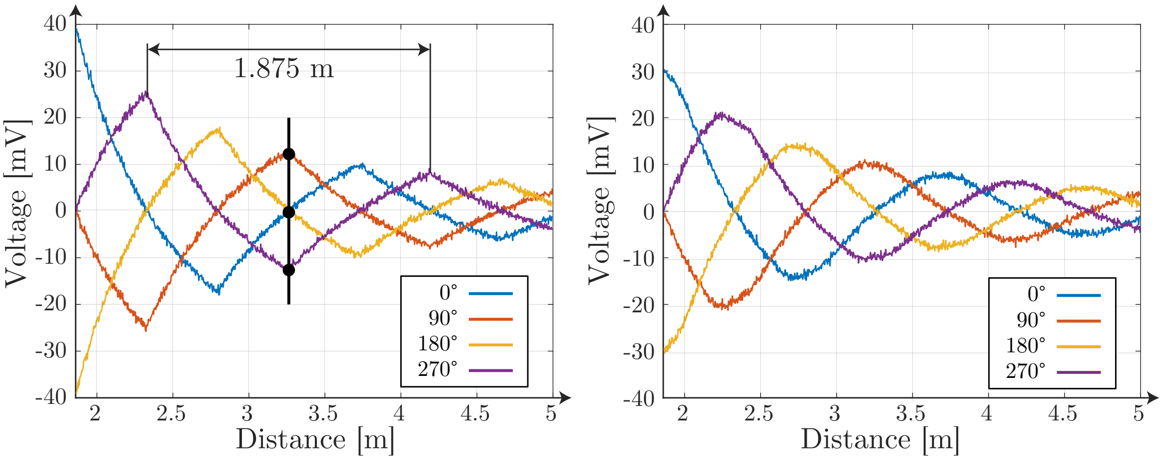

(a)

(b)

Figure 5.3: The cross correlation using a rectangular shaped illumination signal is shown in (a) while the cross correlation using the more realistic shaped signal gaussExtended, see Figure 4.2, is shown in (b).

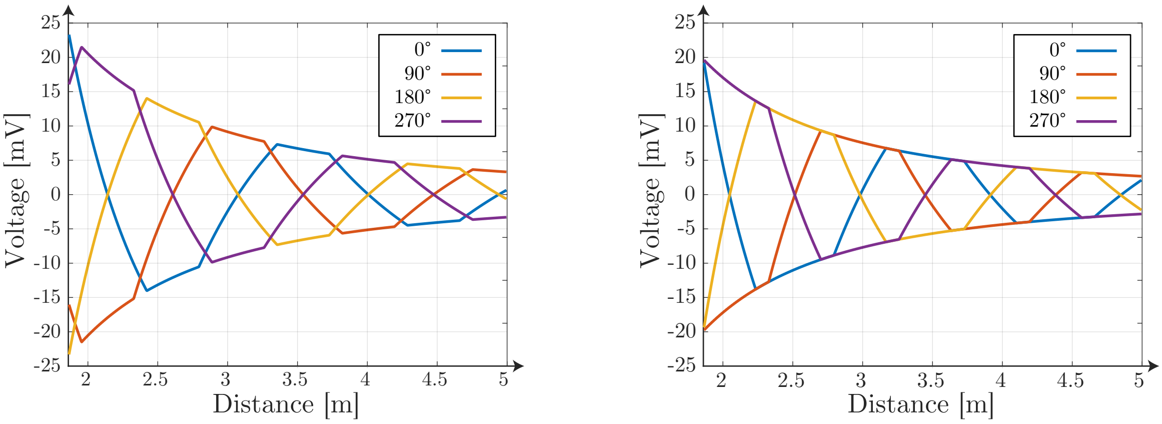

(a)

(b)

Figure 5.4: The correlation signals when using a duty cycle of 30% for the illumination signal (a) and 20% (b) with disabled noise. The duty cycle of the reference signal is constant at 50%.

resulting voltage decreases with larger distances. But at any distance the voltage levels of the four curves have the same proportions to each other. In the figure, it is marked with a black vertical line. A distance is calculated using the atan function of these 4 values. In the second image, Figure 5.3(b), the cross correlation of an illumination signal with a so-called gaussExtended shape is shown. Its shape can be explained to be between a rectangular and sine-shape. The cross correlation appears then to be rounder, more like a sinus-shaped signal.

The duty cycle of both the reference and the illumination signal can be adjusted. By default, a value of 50% is used. When changing the duty cycle of the illumination signal down to 25% only half of the power is illuminated. A value below 50% leads to a flattened shape of the correlation signals, shown in Figure 5.4(a). Reducing the duty cycle below 25% leads to wrong measurements as there are then uncertainties, Figure 5.4(b). A duty cycle of exactly 25% is the point where the flat areas just do not overlap.

5.3 Wiggling

The systematic wiggling error can also be seen with the model. It can be observed best when using a rectangular shaped illumination signal with disabled noise so that just this systematic error appears. The wiggling error is shown in Figure 5.5(a) when using a 4-phase measurements setup. Due to harmonics in the illumination signal the error is oscillating and has a maximum of about 2.3 centimeters with standard settings. The shape of the wiggling error depends on the illumination signal and the reference signal. It can be observed that the frequency of the wiggling error does not correspond to the modulation frequency but to the number of measured phases.

Figure 5.5(b) shows the wiggling error including noise sources. Due to noise errors it seems that the wiggling error is increasing over distance which is not correct. The wiggling effect does not have dependencies over the distance.

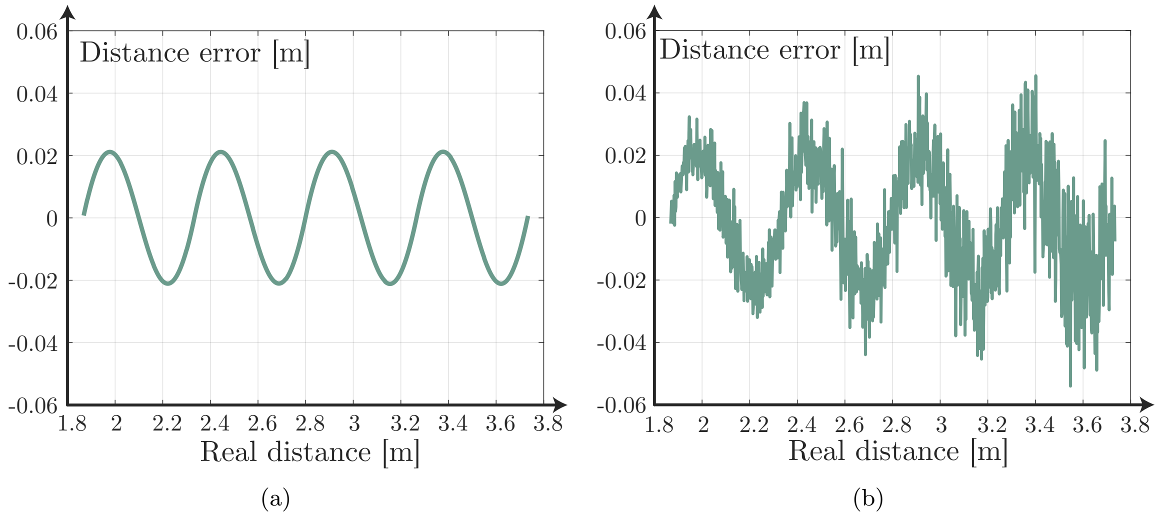

(a)

(b)

Figure 5.5: The wiggling error of a 4-phase measurement without noise (a) and the wiggling error including statistical errors (b).

5.4 Distance error

Figure 5.6(a) shows the calculated distance including noise over the real distance. It is colored in gray and white bars to show the unambiguity range of the used modulation frequency. Each bar has a width of about 1.87 m. In the beginning from 0 to about 25 centimeters the pixel does not deliver valuable data due to saturation. From then on calculated and real distance lie close together except for wiggling error and noise. With increasing distance the distance noise increases which is recognized in the deviation to the real distance. After reaching the unambiguity range about 1.87 meters the calculated distance returns to zero again. This happens because periodic signals are used and the mathematical four-quadrant *arctan* function returns values between $-\pi$ and π resulting in a phase wrap. The phase is unwrapped in Figure 5.6(b). Now a direct relation between calculated and real distance can be observed. The phase unwrap is applied before phases are converted into distances. The phase is changed when a phase jump happens. Therefore, two values are compared, the current and the one before. When the difference is greater than π, the 2π complement is applied.

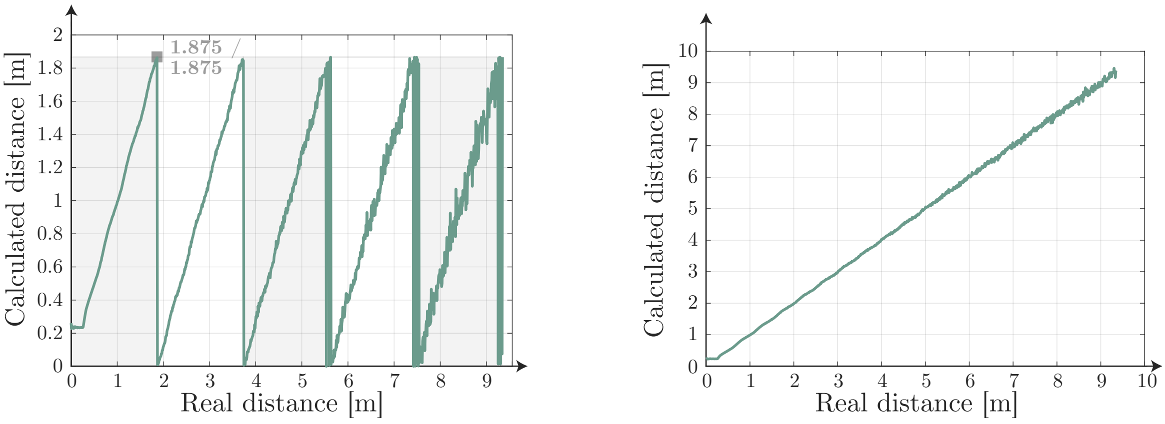

(a)

(b)

Figure 5.6: Calculated distance over the real distance including the unambiguity range using 80 MHz modulation frequency (a). The unwrapped distance over the real distance is shown in (b).

A resulting distance noise of the ToF sensor can be seen in Figure 5.7(a). The error is plotted in meters over the real distance. The green dots represent the calculated standard deviation over 2000 repetitions of the sensor's response function. The simulation was run with 2000 distance samples which is exactly the number of the green dots. The black line is a fitted polynomial line with a degree of four. It ignores the peaks because a robust fitting is used. From the figure it can be observed that the distance noise has an increasing monotone characteristic with larger distances. But there are a lot of outliers that have to be removed. The origin lies in the calculation from raw values to phase values using a arcus tangent function. This four-quadrant trigonometry function can only deliver values between $-\pi$ and π. These values are then further processed to distance values with Equation 2.6. The problem lies in the phase wrap, which happens at multiples of the unambiguity range. The first occurrence is at about 1.875 meters. As noise is applied at those distances it is possible that values are just a bit higher than they should be, which results in a phase wrap down from maximum to minimum. The standard deviation is then very huge and that is the reason for these peaks (outliers) in the figure. Furthermore, it can be observed that at smaller distances, where the noise is smaller, there are less outliers and the width of the gap where the peaks occur is also smaller than at higher distances. The reasons is the uncertainty of the phase wrap occurring with the arctan function is higher with increasing noise level.

Figure 5.7(b) shows the same distance noise behavior with applied algorithm to remove the unwanted peaks. The algorithm takes the phase values and checks through all repetitions of each phase whether there are unwanted phase wraps. It therefore takes the mean of these values to classify whether the phases should have a positive or negative sign. It is a kind of majority voting. Phases that do not meet the requirement of the correct sign are corrected by adding, respectively subtracting 2π. This leads to a monotonic increasing of all calculated standard deviation samples.

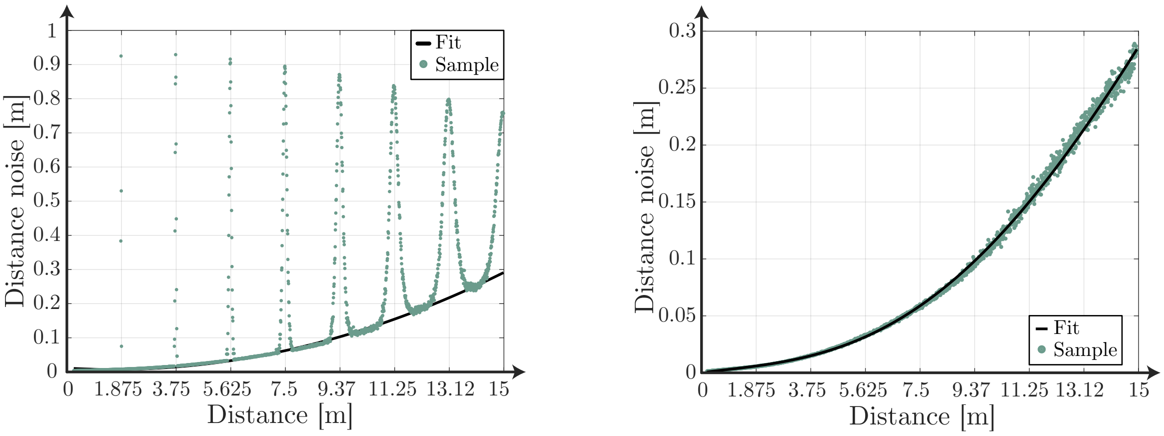

(a) (b)

Figure 5.7: Distance noise over the real distance without ADC, (a) shows the uncorrected distance with outliers and (b) with applied correction.

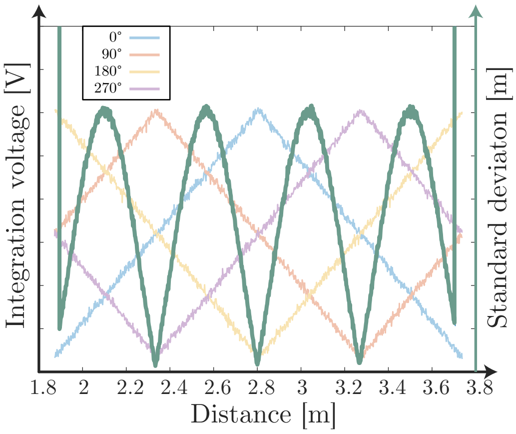

Figure 5.8: Integrated voltages of four phases and standard deviation of distance noise over distance.

When considering a rectangular shaped illumination and reference signal and letting the number of incoming electrons stay constant, the ideal cross correlation curve can be shown in Figure 5.8. 4 cross correlation curves are shown representing four phases which are the integrated voltages of the PMD. Only one sample of each phase is plotted for simplicity. An additional curve is plotted, the distance noise (standard deviation) of the samples after applying the atan function. This shows that the atan operation introduces an oscillating error, which is not recognizable when using a sinusoidal shaped signal and therefore also a sinusoidal shaped cross correlation curve. This error doesn't have anything to do with wiggling, which is shown in Figure 5.5(a). At the unambiguity range the standard deviation becomes very high (here 1.875 and 3.75 m). These peaks are removed with a peak removal function, compare Figure 5.7(a) and 5.7(b).

Figure 5.9 shows the calculated distance over the real distance. The number of curves on the plot correspond to the number of iterations. This one is generated with 20 iterations. The standard deviation of these 20 signals is the noise. The phase unwrap is correct until a distance of about 10 meters are reached. From this point on the errors are too large leading to a wrong phase unwrap. The ToF sensor cannot deliver valuable depth information from then on.

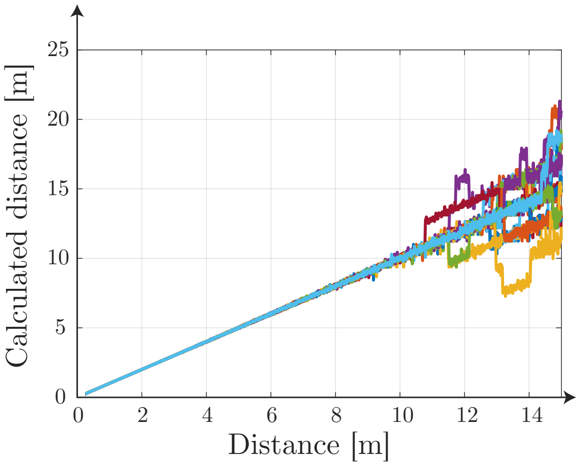

Figure 5.9: Unwrapped calculated distance over the real distance showing a wrong unwrap from a specific distance on.

Another important effect is the usage of a non-perfectly sinusoidal illumination signal. To show the maximum of the wiggling error a rectangular shaped illumination signal is used. Figure 5.10(b) shows this systematic error including noise. Here, the calculated distance is subtracted from the real distance. A similar error can be observed in the depth noise, see Figure 5.10(a). This error, however, does not belong to the wiggling. It is an effect of the atan operation and previously explained with Figure 5.8.

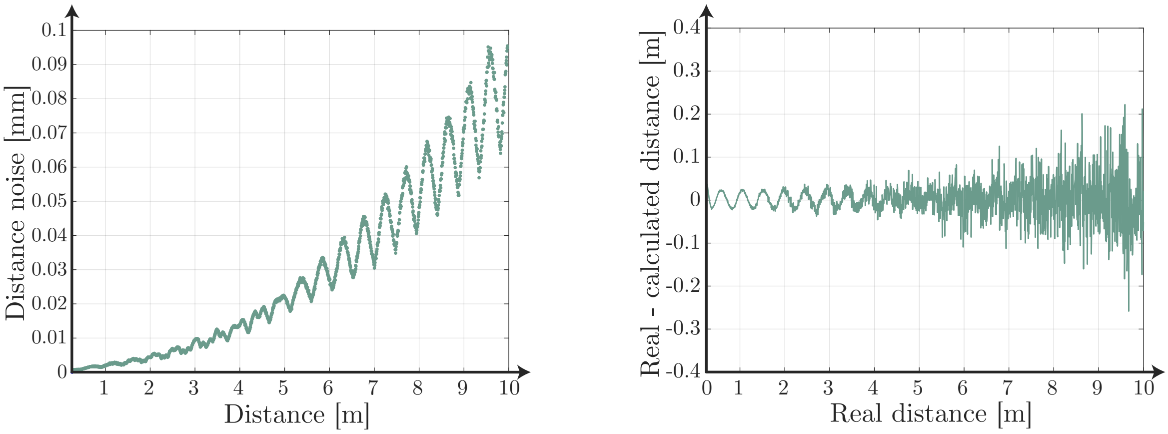

(a)

(b)

Figure 5.10: Oscillating effect on depth noise (a) and the wiggling error (b).

5.5 Verification

This sections shows the verification results between the model and a selected ToF hardware. Three different sweep configurations are compared, sweep over distance, background light and integration time.

5.5.1 Sweep over distance

A very basic sweep is the one over distance without background illumination. The LTS is able to cover a range between 0.4 and 4.5 meters. Nearly the whole distance range is used. The real distance is gathered from the LTS and used as input parameter for the model. So there are exactly the same number of samples that allows a direct comparison. The waveform of the illumination signal in the model is chosen as *gaussExtended* with factor 15, 25% duty cycle and an optical peak power of 1.2 W. Figure 5.11(a) shows the resulting amplitude plots. The green curve is the one of the model and the blue one of the measurement. The amplitude values belong to raw values of a 12 bit ADC. It can be seen that at low distances the amplitude is huge and it decreases very fast with the distance. From about 1 meter on the slope is much smaller than at the beginning. As [Sch05, p. 22] succinctly puts it, the signal power is proportional to $\frac{1}{d^2}$ where d is the distance from the ToF sensor to the target. As the values of the two curves are very similar the optical path can be accepted as correct. It does not exactly match as the model does not consider factors like lens distortion. It is assumed that these factors are small when modeling a center pixel only.

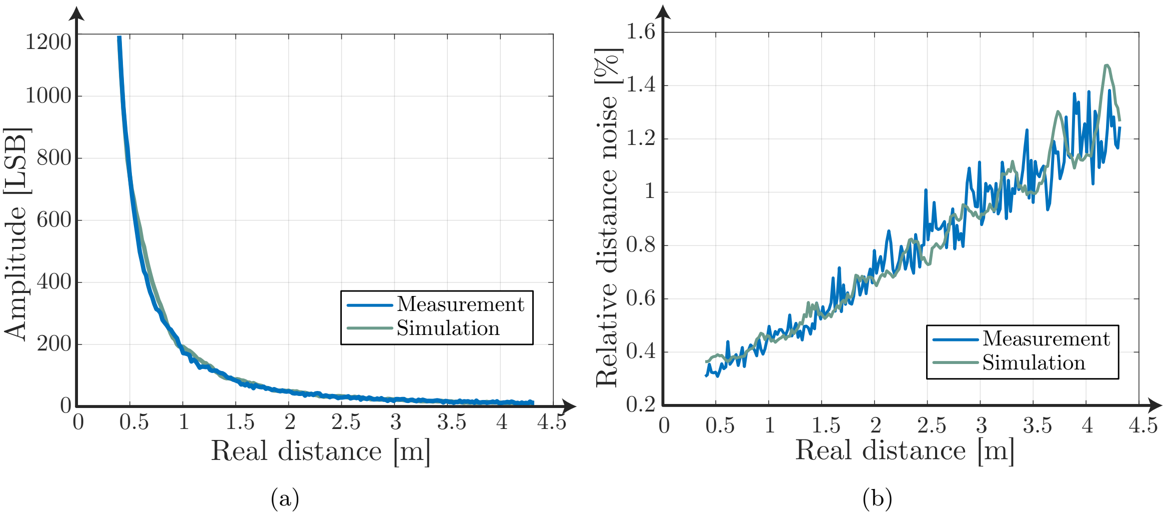

(a)

(b)

Figure 5.11: Absolute amplitude (a) and relative distance noise (b) over the real distance.

Figure 5.11(b) shows the relative distance noise in relation to the x-axis, the real distance. At 1 meter a relative distance error of roughly 0.5% can be seen. The relative distance noise error doubles at approximately 3.5 meters. This means that at 1 meter the absolute error is 0.005 m while at 3.5 meters it is 0.035 m. So the relative plot seems to be linear more or less in this case but the absolute error shows a non-linear behavior. When looking at the amplitude at 4 meters it is very low compared to the beginning of the curve. As a reason, the signal to noise ratio has to decrease over distance as a lower number of photons arrive at the camera.

Amplitude and phase (latter refers to a distance) is the only information gathered with the LTS but the model provides more data to look at. The following two figures use a distance sweep of 0.1 to 10 meters to get a better overview. One of them is the Photon Transfer Curve (PTC), see Figure 5.12(a). It shows signal as well as noise electrons of various noise sources over the signal electrons in a logarithmic way. The smallest noise source is dark current and its shot noise in grey. It contributes with reset noise and hold noise to read noise (orange). Photon shot noise is visible in violet. The total noise can be seen in green, consisting of read noise and photon shot noise. The left side of the figure, marked with I, refers to low light levels. In this region read noise is the dominant noise source. In region II photon shot noise becomes the dominant noise source with an increase in signal electrons, stated as number of light intensity electrons.

Out of the PTC the SNR can already be seen which is the quotient of signal to noise. However, the visualization distorts the SNR. That is why the calculated SNR can be seen in Figure 5.12(b). The x-axis is plotted in reverse order to be comparable to the PTC. As expected, the largest SNR is a lowest distance, meaning that a lot of the illuminated optical power is reflected back to the camera. Using 10^6 signal electrons and 10^3 noise electrons gives an SNR of

$$SNR = 20 \cdot \log\left(\frac{n_{eSignal}}{n_{eTotalNoise}}\right) = 20 \cdot \log\left(\frac{10^6}{10^3}\right) \cong 138dB \tag{5.1}$$

The SNR decreases with larger distances. At the PTC, a small distance between signal and total noise can be observed at the left side.

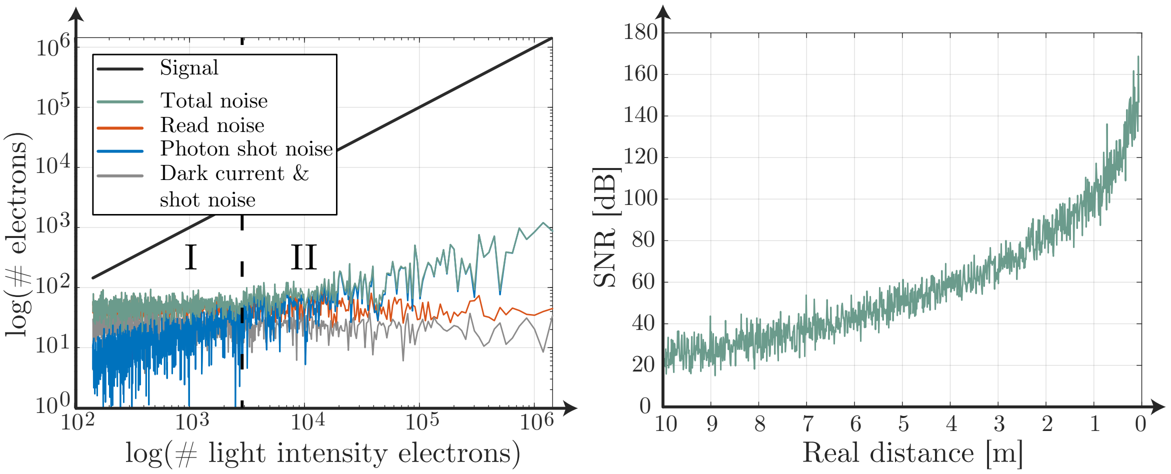

(a) (b)

Figure 5.12: The photon transfer curve of the model with a sweep over distance (a) and the relating SNR (b).

5.5.2 Sweep over background light

This sweep configuration lets the ToF sensor stay at a constant distance of 1 meter to the target. The ToF sensor does not have an optical filter applied. A halogen spotlight is used as background light source. Its voltage is adjustable to control the intensity of the light source. The model and the measurement differ in a way that the position of the light source cannot be exactly in the same position as the camera. The illuminance is measured with a lux meter on the reflection target, approximately at the position where the camera focuses on. Figure 5.13 shows the comparison of the simulation and measurement. The relative distance noise relates to 1 meter distance. There are only a few samples obtained as the light source does not provide a fine graduation in illuminance. A problem with the measurement is that the light source drifted in matter of background illuminance. That is why the blue curve shows 2 points at about 2.6 and 4.5 klx with smaller values. Photon shot noise is the dominant noise source due to the huge number of electrons received by the camera. That is why the curves show a root behavior. At 500 lx the relative distance noise is about 1.3% and it doubles at approximately 3 klx. Their associated absolute values would be 0.013 m and 0.026 m distance noise. At low light levels the slope of the curves is much steeper.

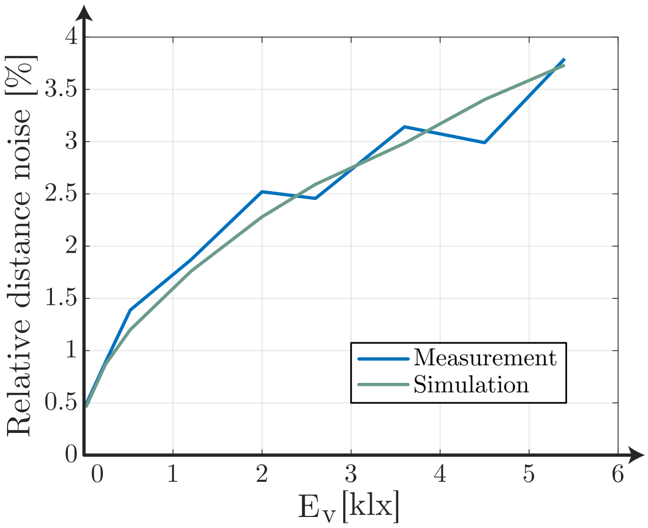

Figure 5.13: Relative distance noise over background illuminance.

A noise listing can be seen in the PTC in Figure 5.14(a). The number of signal electrons is constant since the distance from the sensor to the target is not varied and always exactly the same optical power is emitted. There is no factor that models a variation in optical spread or reflection. The read noise contributors are hold noise and reset noise. Hold noise is a noise source which occurs during the readout phase of the PMD. It is similar to reset noise. Thermal noise in the source follower leads to a variation in number of charges. This fluctuation differs each time a pixel is read out which is modeled as hold noise. The PTC shows that read noise is dominant in the beginning at 10^4 electrons, relating to a background illuminance of 20 lx while with increasing illuminance photon shot noise is the noise source which gets weighted at most. Comparing the PTC to the SNR in Figure 5.14(b) leads to the insight that the SNR decreases with background illuminance at constant distance level.

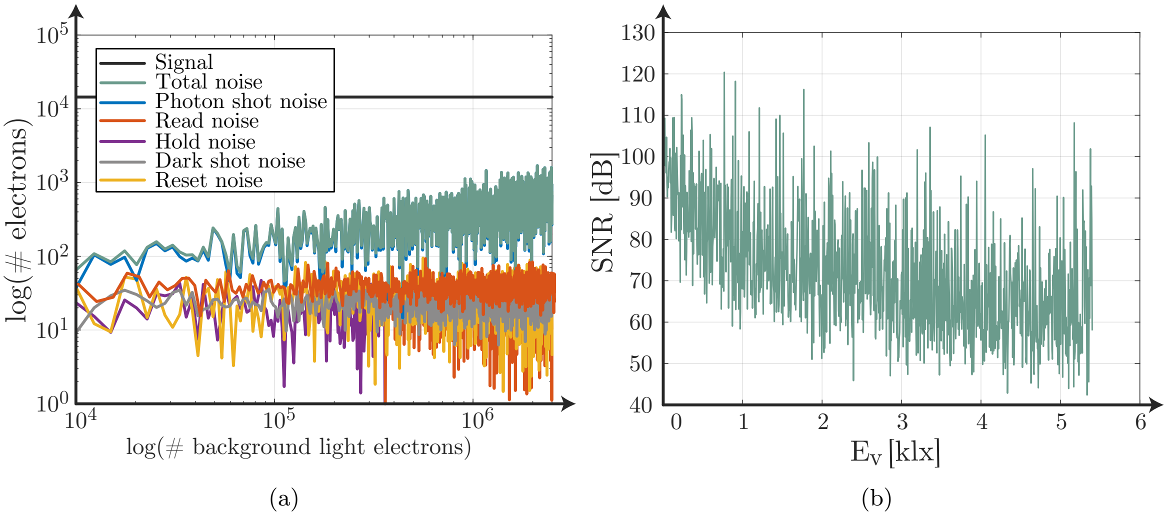

(a) (b)

Figure 5.14: The photon transfer curve of the model with a sweep over background light (a) and the relating SNR over background illuminance (b).

The stronger the illuminance of the background light source, the more charges are generated inside a pixel of the PMD. Charges which have their origin in the background light get equally distributed to A and B which causes a common mode in the resulting integrated voltage as always the difference between A and B voltages contains distance information. The SBI behavior is examined in more detail with Figure 5.15(a). It can be seen that final voltages at the end of the integration process of A and B are parallel to each other until one of them reaches $V_{saturated}$. The cause of this is that the distance from the camera to the object is fixed so the number of charges which gets distributed according to the distance are always the same as background light charges are equally distributed to the taps. When the blue Curve reaches the saturation voltage $V_{saturated}$,

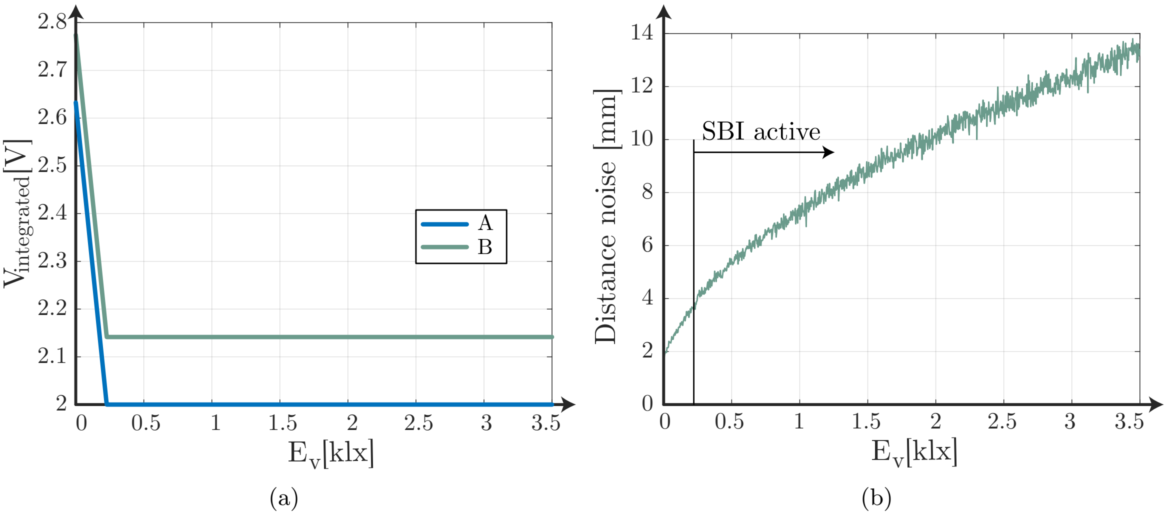

(a) (b)

Figure 5.15: The integrated voltages of A and B are shown in (a) while the absolute distance noise is visible in (b).

the voltage B is integrated in positive direction having a final value of 2.141 V. Further increasing of the illuminance always leads to the same integrated value of B. So the SBI removes the common mode. Figure 5.15(b) shows the noise behavior. The point where SBI starts working is at 230 lx. At this point the slope of the curve is increased.

5.5.3 Sweep over integration time

The last sweep configuration is the one over integration time. The distance from the ToF camera to the reflection target is constant 1 meter. In this configuration no background illumination is used. At the LTS side for each measurement the sensor is reconfigured to use another integration time. The integration time is varied in a range of 500 μs to 4 ms. An integration time of 4 ms is very high as a further increase leads to a power down of the sensor due to eye-safety reasons. This is because the peak power which drives the illumination unit is limited. Figure 5.16(a) shows the amplitude over integration time which has a linear dependency. The measurement at 2 ms gives an amplitude of about 180 which matches with the measurement of the sweep over distance in Figure 5.11(a).

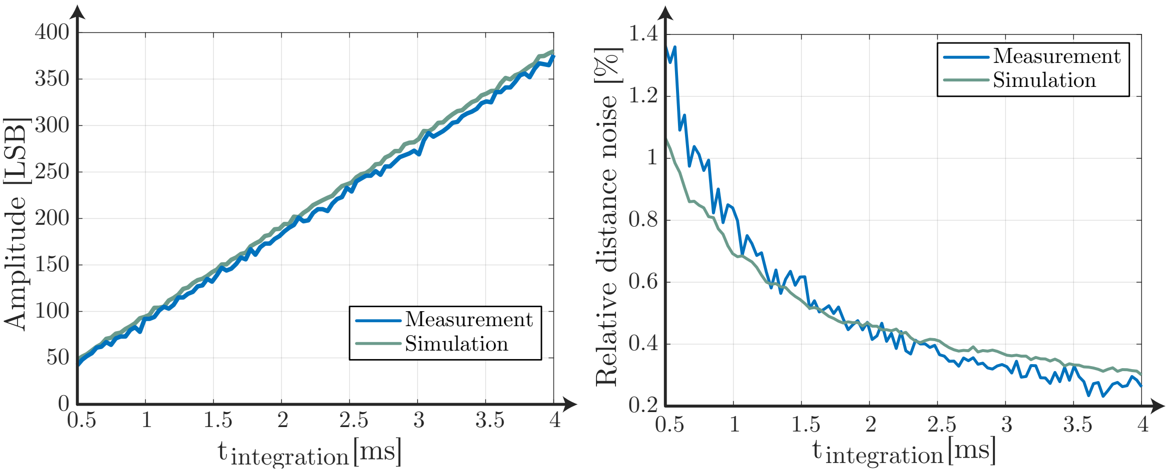

(a)

(b)

Figure 5.16: Absolute amplitude (a) and relative distance noise (b) over integration time.

The relative distance noise relates to 1 meter distance and is shown in Figure 5.16(b). The distance noise decreases with higher integration times. The noise level gets lower due to the fact that the sensor is able to collect more photons, increasing the signal level. When increasing the integration time from about 1 ms to 2.5 ms the relative noise level halves.

The simulation gives information about the noise sources being effective in this sweep configuration, see Figure 5.17(a). Read noise and photon shot noise lie in the same range for low light conditions (at low integration times). This differs from the sweep over background light, where they have different noise levels. With higher integration times photon shot noise is the dominant noise source. As the signal increases with a higher slope the SNR increases as well. This behavior can be seen in Figure 5.17(b).

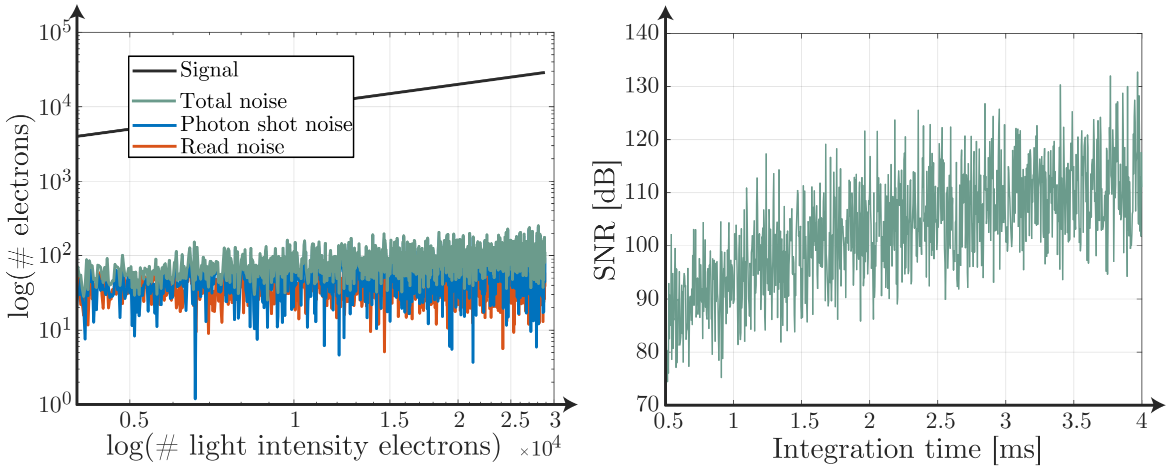

(a) (b)

Figure 5.17: The photon transfer curve of the model with a sweep over integration time (a) and the corresponding SNR over integration time.

5.5.4 Distance noise estimation

According to Perenzoni and Stoppa distance noise can be estimated. It is based on a pulsed wave modulation and its variance is formulated in Equation 5.2 [PS11].

$$\sigma_{zMin} = \frac{c}{4 \cdot \sqrt{2} \cdot \pi \cdot f_{fmod} \cdot SNR_{max}} \tag{5.2}$$

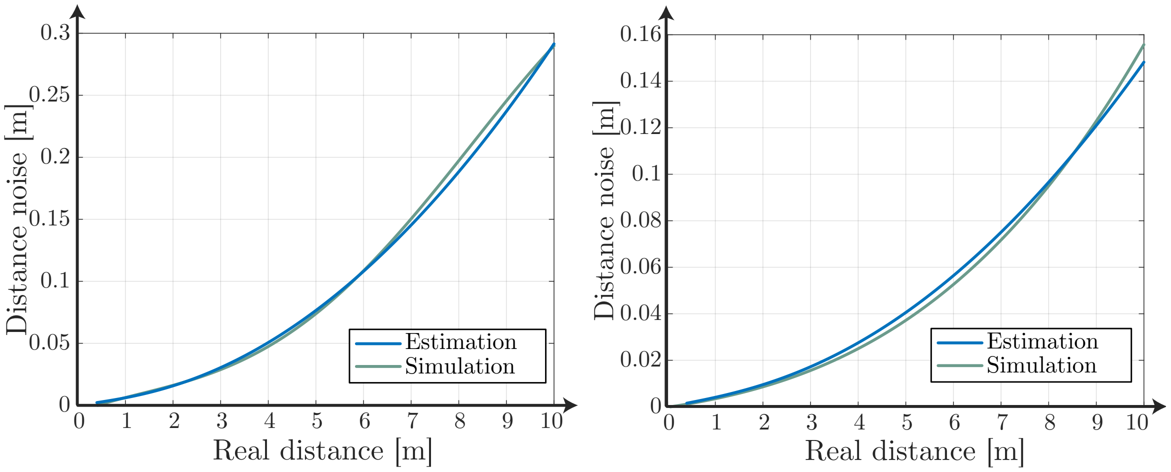

(a) (b)

Figure 5.18: Distance noise over real distance for a duty cycle of 12.5% (a) and 25% (b).

The SNR is the quotient of signal to noise. For the signal the number of electrons which are distributed to their distance and equally distributed in A and B are considered. The signal electrons are adjusted in order to involve 4-phases for a measurement and incorporate the duty cycle of the illumination unit. The noise is characterized to be the quadratic sum of all noise sources including quantization noise, involving channel A and B and numbers of phases.

Figure 5.18 shows the comparison of the model in green (fitted curve) with the noise estimation with the formula above for a duty cycle of 12.5% (a) and 25%. The estimation does not consider the internal behavior of the sensor, the mixing process. It can be seen that the model and the estimation are both very similar. The only limitation is, that it cannot be compared using background light because the model uses a constant illuminance over the whole distance range.

The disadvantage on the formula is that it is just usable with ideal rectangular shaped wave forms so the output differs from real behavior. Additionally, the internal behavior cannot be observed, just the distance noise can be examined.

Chapter 6

Conclusion

The entire thesis is summarized in this chapter. Results are discussed, future work and challenges are outlined.

In the last decade Time-of-Flight imaging technology has become more and more popular in computer vision applications. The number of pixels has increased while the form factor is getting smaller. That is why it is possible to put such cameras into smart phones. Nevertheless, the killer app has not yet been found, but having its application in consumer electronics is expected.

The goal of this thesis is the implementation of a ToF camera model to gather performance analysis and deeper know-how of a ToF camera. The starting point is the optical path, the illumination unit of the camera including reflection and lens properties. The focus, however, lies in the ToF sensor part, where the photo detection and mixing process happens. Noise sources are added in this part of the model which gives performance information after applying post processing steps. A selected ToF hardware using a 4-phase measurement set-up is compared with the model. Three different sweep configurations are compared: Distance, integration time and background illumination. It is shown that the model does not exactly match the measurements but comes very close to it. At strong illumination, photon shot noise is dominant which cannot be eliminated due to physical effects. Reducing the amount of incoming photons to the camera like increasing the distance leads to a domination of read noise. It consists of several noise sources and can be reduced as some depend on the temperature. On the systematic error side the harmonic error (wiggling) is shown. It occurs when selecting a non-sinusoidal signal. The error is oscillating and its magnitude is maximum using a rectangular-shaped signal.

For user convenience a Graphical User Interface is provided. Parameters can be set in a graphical way and the illumination and reference signal are plotted in order to verify the shape of the signals. A number of plots can be selected which get generated after finishing the calculation. With this model ToF camera properties can be examined to unveil bottlenecks and optimizations. It helps to estimate whether a specific parameter configuration leads to a specified performance to fulfill consumer requirements. On the other hand a rough estimate can be achieved with the use of a noise estimation formula so not the whole simulation has to be done.

6.1 Future Work

This section concludes the thesis looking at aspects that were not modeled and are therefore inputs for further improvements and extensions.

6.1.1 Optical path

As all performance data refers to a center pixel of the camera the model can be extended to the whole pixel array. This includes further research in the optical path. The driver circuit for the VCSEL or LED has to be investigated in more detail. The illuminated optical power differs from the center to the edges. Therefore an optical power distribution has to be considered dependent on wave shape and modulation frequency. On the camera side, lens properties can be applied, like distortion and losses. The camera and lens are also displaced. The current Lambert reflector can be replaced to model a more complex reflection to model also absorption and permeability of transparent objects.

6.1.2 Pixel settings

The following list shows some examples of extensions to the current model to get more precise results.

- Asymmetry of the SBI
- Reset and SBI threshold voltage deviation
- Fixed pattern phase noise
- Phase offset error of phase shifting unit
- Inaccuracy of duty cycle
- Wiggling correction
- Usage of a measured illumination and reference signal shape

6.1.3 Applications

An application would be to check multi path problems, one ToF camera facing an edge. Another would be to investigate the impact of several ToF cameras interfering each other.

The sensor response function can be replaced to model direct ToF or coded modulation where complex modulation signals are possible. With coded modulation the unambiguity range directly relates to the length of the used code. Multi ToF camera interference is reduced. Furthermore, the wiggling error could be reduced to a factor where calibration is not required any more. During one exposure different phases have to be used. Another application for modulation coding is that transparent objects can be removed or more precisely, the foreground and background depth image can be obtained according to [Kad+13].

Currently, the model implements phase algorithms using 2 to 5 phases but only 4 phases are compared with real ToF data. Other algorithms can be examined in order to show differences, pros and cons.

The sensor response function can be optimized in terms of the opto-electronic mixing process leading to a shorter computation time.

Additional sweep configurations can be applied to investigate points of interest. These could be temperature, modulation frequency, wavelength, optical power and pixel pitch.

Appendices

Appendix A

Hardware Settings

The modified default register settings of the used ToF camera are shown in Table A.1.

Register name	Address	Value	Reset Value	Description
PLLBGEN	0xA007	0x0001	0x0000	PLL bandgap enable
VMODREG	0xA00A	0x0007	0x0006	VMOD Regulator configuration. Enable regulator for modulation voltage
CFGCNT_PLLCFG3_LUT2	0x9842	0x0BE2	0x0BE3	PLL configuration register 3. Fractional value of the division implemented in the multimodulus divider
ANAIP_DPHYDLANE1CFG1	0xA063	0x01C5	0x1CA	
ANAIP_DPHYDLANE1CFG3	0xA065	0x0206	0x020F	
ANAIP_DPHYDLANE2CFG1	0xA066	0x01C5	0x01C4	
ANAIP_DPHYDLANE2CFG3	0xA068	0x0206	0x020F	
CFGCNT_PLLCFG1_LUT1	0x983D	0x6261	0x8245	80.32 MHz
CFGCNT_PLLCFG2_LUT1	0x983E	0xFC96	0x3D71	80.32 MHz
CFGCNT_PLLCFG3_LUT1	0x983F	0x0BE2	0x030A	80.32 MHz
CFGCNT_PLLCFG1_LUT2	0x9840	0x8245	0x6261	60.24 MHz
CFGCNT_PLLCFG2_LUT2	0x9841	0x3D70	0xFC96	60.24 MHz
CFGCNT_PLLCFG3_LUT2	0x9842	0x030A	0x0BE2	60.24 MHz
ANAIP_PADGPIOCFG0	0xA01C	0x1313	0x1315	GPIO0 tristate
ANAIP_PSPADCFG	0xA084	0x1513	0x1313	MOD_SE_P pad push/pull

`ANAIP_PADGPIOCFG1`	0xA01D	0x1513	0x1313	GPIO3 push/pull
`CFGCNT_CSICFG`	0x9835	0x0092	0x0190	enable superframe
`CFGCNT_S00_EXPOTIME`	0x9800	0x1788	0x4EB5	0.1ms @ 60.24 MHz
`CFGCNT_S00_PS`	0x9802	0x2332	0x000C	pll = 1, ps = grey_off
`CFGCNT_S01_EXPOTIME`	0x9803	0x939C	0x539C	2ms @ 80.32 MHz
`CFGCNT_S01_PS`	0x9805	0x0004	0x0040	pll = 0, ps = 0
`CFGCNT_S02_EXPOTIME`	0x9806	0x939C	0x539C	2ms @ 80.32 MHz
`CFGCNT_S02_PS`	0x9808	0x0048	0x0084	pll = 0, ps = 90
`CFGCNT_S03_EXPOTIME`	0x9809	0x939C	0x539C	2ms @ 80.32 MHz
`CFGCNT_S03_PS`	0x980B	0x008C	0x00C8	pll = 0, ps = 180
`CFGCNT_S04_EXPOTIME`	0x980C	0x939C	0x539C	2ms @ 80.32 MHz
`CFGCNT_S04_PS`	0x980E	0x00C0	0x020C	pll = 0, ps = 270
`CFGCNT_S05_EXPOTIME`	0x980F	0x7AD4	0x539C	2ms @ 60.24 MHz
`CFGCNT_S05_PS`	0x9811	0x0204	0x0240	pll = 1, ps = 0
`CFGCNT_S06_EXPOTIME`	0x9812	0x7AD4	0x539C	2ms @ 60.24 MHz
`CFGCNT_S06_PS`	0x9814	0x0248	0x0284	pll = 1, ps = 90
`CFGCNT_S07_EXPOTIME`	0x9815	0x7AD4	0x539C	2ms @ 60.24 MHz
`CFGCNT_S07_PS`	0x9817	0x028C	0x02C8	pll = 1, ps = 180
`CFGCNT_S08_EXPOTIME`	0x9818	0x7AD4	0x539C	2ms @ 60.24 MHz
`CFGCNT_S08_PS`	0x981A	0x02C0	0x2332	pll = 1, ps = 270

Table A.1: Register settings of the ToF camera.

Symbols

Sign	Description	Unit
A_{Scene}	Circular area on which the illumination unit projects its power	m^2
E	Amplitude of the illuminated signal	LSB
A	Amplitude of the received signal	LSB
c	Speed of light	m/s
$C_{integration}$	Integration capacitor of one tap of the PMD	F
D	Diameter of the lens	m
d	Distance between a time-of-flight sensor and an object	m
d_u	The unambiguity range	m
E_e	Irradiance	W/m^2
$E_{eBackground}$	Irradiance of the background illumination	W/m^2
E_{eScene}	Irradiance of the illumination unit	W/m^2
e	Elementary charge	C
E_v	Background illuminance. The index v ensures that it is a photometric unit	lx = lm/m^2
f_c	Cut-off frequency	Hz
Δf	Bandwidth	Hz
f_{lens}	Focal length of the lens	m

Sign	**Description**	**Unit**
f_{mod}	Modulation frequency	Hz
f_{number}	F number of the lens	
I	Mean intensity	LSB
k	Boltzmann constant	J/K
K	Demodulation contrast	%
k_{lens}	Losses of the lens	
K_m	Luminous efficacy of radiation	lm/W
λ	Wavelength as defined in [87a]	m
μ	Mean / expectation value	
p	Reflection factor	
φ	Phase shift	rad
Φ_{eIllu}	Radiant flux which the illumination unit emits	W
Φ_v	Luminous flux	lm
Q	Electric charge	C
$\eta(\lambda)$	Quantum efficiency	%
R	Resistor	Ω
sel	A selector number for the type of background light	

Sign	**Description**	**Unit**
σ^2	Variance	
$S(\lambda)$	Spectral responsivity	A/W
σ	Standard deviation	
T	Periodic time	s
V_{reset}	Reset voltage of the integration capacitor $C_{integration}$	V
$V_{saturated}$	Pixel saturation voltage and SBI threshold voltage $C_{integration}$	V

Abbreviations

Notation	**Description**
3-D	Three-Dimensional
ADC	Analog Digital Converter
API	Application Programming Interface
BRDF	Bidirectional Reflectance Distribution Function
CIE	Commission Internationale de l'Eclairage
CSV	Comma-separated values
CW	Continuous Wave
FF	Fill Factor
FoV	Field of View
FPN	Fixed Pattern Noise
FPS	Frames Per Second
FSR	Full Scale Range
GUI	Graphical User Interface
IR	Infrared

Notation	**Description**
LED	Light Emitting Diode
LSB	Least Significant Bit
LTS	Linear Translation Stage
LUT	Look-up Table
PDF	Probability Density Function
PMD	Photonic Mixing Device
PTC	Photon Transfer Curve
SBI	Suppression of Background Illumination
SNR	Signal-to-Noise Ratio
ToF	Time-of-Flight
USB	Universal Serial Bus
VCSEL	Vertical Cavity Surface-Emitting Laser

Bibliography

[Alb07] Martin Albrecht. “Untersuchung von Photogate-PMD-Sensoren hinsichtlich qualifizierender Charakterisierungsparameter und -methoden”. University of Siegen, Oct. 19, 2007. URL: `http://dokumentix.ub.uni-siegen.de/opus/frontdoor.php?source_opus=297&la=de` (visited on 11/02/2017).

[Ana+10] T. Anaxagoras, P. Kent, N. Allinson, R. Turchetta, T. Pickering, D. Maneuski, A. Blue, and V. O’Shea. “eLeNA: A Parametric CMOS Active-Pixel Sensor for the Evaluation of Reset Noise Reduction Architectures”. In: *IEEE Transactions on Electron Devices* 57.9 (Sept. 2010), pp. 2163–2175. ISSN: 0018-9383. DOI: `10.1109/TED.2010.2052418`.

[Bas+94] Michael Bass, Eric W. Van Stryland, David R. Williams, and William L. Wolfe. *Handbook of Optics, Fundamentals, Techniques, and Design.* 2nd ed. Vol. I. McGraw-Hill Professional, Jan. 9, 1994. ISBN: 978-0-07-047740-7.

[Bat+10] Sebastiano Battiato, Arcangelo Ranieri Bruna, Giuseppe Messina, and Giovanni Puglisi. *Image Processing for Embedded Devices.* Bentham Science Publishers, Nov. 26, 2010. 388 pp. ISBN: 978-1-60805-170-0.

[Ber08] Kurt Bergmann. *Elektrische Meßtechnik: Elektrische Und Elektronische Verfahren, Anlagen Und Systeme.* 6th ed. Viewegs Fachbücher der Technik. Vieweg+Teubner Verlag, 2008. ISBN: 978-3-528-54080-7. DOI: `10.1007/978-3-663-01616-8`.

[Bur05] Richard Burdett. “Signals in the Presence of Noise”. In: *Handbook of Measuring System Design.* John Wiley & Sons, Ltd, 2005. ISBN: 978-0-471-49739-4. DOI: `10.1002/0471497398.mm395`.

[Büt+05] Bernhard Büttgen, Thierry Oggier, Michael Lehmann, Rolf Kaufmann, and Felix Lustenberger. “CCD/CMOS Lock-in Pixel for Range Imaging: Challenges, Limitations and State-of-the-Art”. In: *In Proceedings of 1st Range Imaging Research Day.* 2005, pp. 21–32.

[Bux+12] Bernd Buxbaum, Bianca Hagebeuker, Robert Lange, and Thorsten Ringbeck. “3D Time-of-Flight (ToF)”. In: *SpringerLink* (2012), pp. 187–197. DOI: `10.1007/978-3-8348-8619-4_15`.

[Cal05] Irene Calizo. “Reset Noise in CMOS Image Sensors”. Master’s thesis. San Jose State University, Jan. 1, 2005. URL: `http://scholarworks.sjsu.edu/etd_theses/2746`.

[Chi+09] Filiberto Chiabrando, Roberto Chiabrando, Dario Piatti, and Fulvio Rinaudo. “Sensors for 3D Imaging: Metric Evaluation and Calibration of a CCD/CMOS Time-of-Flight Camera”. In: *Sensors* 9.12 (Dec. 11, 2009), pp. 10080–10096. DOI: `10.3390/s91210080`.

[Chi10] Yih-Peng Chiou. “Introduction To CMOS Image Sensor Design”. No.1, Sec. 4, Roosevelt Road Taipei, 106 Taiwan: Department of Electrical Engineering, BL617 National Taiwan University, June 15, 2010. URL: `http://ccf.ee.ntu.edu.tw/~ypchiou/Intro_EO/CMOS_Image_Sensor.pdf` (visited on 11/06/2017).

[Cho17] Jihyun Cho. "CMOS Sensors for Time-Resolved Active Imaging". Dissertation. June 14, 2017. URL: `https://deepblue.lib.umich.edu/handle/2027.42/136950?show=full` (visited on 11/06/2017).

[Dec+98] S. Decker, D. McGrath, K. Brehmer, and C. G. Sodini. "A 256 Times;256 CMOS Imaging Array with Wide Dynamic Range Pixels and Column-Parallel Digital Output". In: *IEEE Journal of Solid-State Circuits* 33.12 (Dec. 1998), pp. 2081–2091. ISSN: 0018-9200. DOI: `10.1109/4.735551`.

[Dru+15] N. Druml, G. Fleischmann, C. Heidenreich, A. Leitner, H. Martin, T. Herndl, and G. Holweg. "Time-of-Flight 3D Imaging for Mixed-Critical Systems". In: *IEEE 13th International Conference on Industrial Informatics (INDIN).* July 2015, pp. 1432–1437. DOI: `10.1109/INDIN.2015.7281943`.

[Ebe12] Carina Elisabeth Eberhardt. "High Speed Signal Processing Algorithms for Time-of-Flight Image Sensors". University of applied sciences Hagenberg, Sept. 2012.

[Ett05] Wim Van Etten. *Introduction to Random Signals and Noise.* 1st ed. Chichester, England ; Hoboken, NJ: Wiley, Aug. 5, 2005. 270 pp. ISBN: 978-0-470-02411-9.

[Fah+16] Ludwig Fahrmeir, Christian Heumann, Rita Künstler, Iris Pigeot, and Gerhard Tutz. *Statistik.* Springer-Lehrbuch. Berlin, Heidelberg: Springer Berlin Heidelberg, 2016. ISBN: 978-3-662-50371-3. DOI: `10.1007/978-3-662-50372-0`.

[FAT11] S. Foix, G. Alenya, and C. Torras. "Lock-in Time-of-Flight (ToF) Cameras: A Survey". In: *IEEE Sensors Journal* 11.9 (Sept. 2011), pp. 1917–1926. ISSN: 1530-437X. DOI: `10.1109/JSEN.2010.2101060`.

[Fra+09] Mario Frank, Matthias Plaue, Holger Rapp, Ullrich Köthe, Bernd Jähne, and Fred A. Hamprecht. *Theoretical and Experimental Error Analysis of Continuous-Wave Time-Of-Flight Range Cameras.* Vol. 48. Jan. 1, 2009. 3602 pp. DOI: `10.1117/1.3070634`.

[Fre13] Daniela Freidl. "Efficient Implementation of Novel Time-of-Flight Signal Processing Algorithms". Graz University of Technology, Dec. 2013.

[Für+16] P. Fürsattel, S. Placht, M. Balda, C. Schaller, H. Hofmann, A. Maier, and C. Riess. "A Comparative Error Analysis of Current Time-of-Flight Sensors". In: *IEEE Transactions on Computational Imaging* 2.1 (Mar. 2016), pp. 27–41. ISSN: 2333-9403. DOI: `10.1109/TCI.2015.2510506`.

[GBG16] M. Georgiev, R. Bregović, and A. Gotchev. "Fixed-Pattern Noise Modeling and Removal in Time-of-Flight Sensing". In: *IEEE Transactions on Instrumentation and Measurement* 65.4 (Apr. 2016), pp. 808–820. ISSN: 0018-9456. DOI: `10.1109/TIM.2015.2494622`.

[Gra+10] M. Granados, B. Ajdin, M. Wand, C. Theobalt, H. P. Seidel, and H. P. A. Lensch. "Optimal HDR Reconstruction with Linear Digital Cameras". In: *IEEE Computer Society Conference on Computer Vision and Pattern Recognition.* June 2010, pp. 215–222. DOI: `10.1109/CVPR.2010.5540208`.

[Grü13] Johannes Grünwald. "Investigation of Systematic Errors in Time-of-Flight Imaging". Graz University of Technology, Austria, Jan. 24, 2013.

[Grz+13] Marcin Grzegorzek, Christian Theobalt, Reinhard Koch, and Andreas Kolb, eds. *Time-of-Flight and Depth Imaging. Sensors, Algorithms, and Applications.* Red. by David Hutchison, Takeo Kanade, Josef Kittler, Jon M. Kleinberg, Friedemann Mattern, John C. Mitchell, Moni Naor, Oscar Nierstrasz, C. Pandu Rangan, Bernhard Steffen, Madhu Sudan, Demetri Terzopoulos, Doug Tygar, Moshe Y. Vardi, and Gerhard Weikum. Vol. 8200. Lecture Notes in Computer Science. Berlin, Heidelberg: Springer Berlin Heidelberg, 2013. ISBN: 978-3-642-44963-5. DOI: `10.1007/978-3-642-44964-2`.

[HA11] Uwe Hahne and Marc Alexa. “Exposure Fusion for Time-Of-Flight Imaging”. In: *Computer Graphics Forum* 30.7 (Sept. 1, 2011), pp. 1887–1894. ISSN: 1467-8659. DOI: `10.1111/j.1467-8659.2011.02041.x`.

[Han+13] Miles Hansard, Seungkyu Lee, Ouk Choi, and Radu Horaud. *Time-of-Flight Cameras.* SpringerBriefs in Computer Science. London: Springer London, 2013. ISBN: 978-1-4471-4657-5. DOI: `10.1007/978-1-4471-4658-2`.

[Has14] Samuel W. Hasinoff. “Photon, Poisson Noise”. In: *Computer Vision.* Springer, Boston, MA, 2014, pp. 608–610. DOI: `10.1007/978-0-387-31439-6_482`.

[HK94] G. E. Healey and R. Kondepudy. “Radiometric CCD Camera Calibration and Noise Estimation”. In: *IEEE Transactions on Pattern Analysis and Machine Intelligence* 16.3 (Mar. 1994), pp. 267–276. ISSN: 0162-8828. DOI: `10.1109/34.276126`.

[Her17] Miguel Heredia Conde. *Compressive Sensing for the Photonic Mixer Device.* Wiesbaden: Springer Fachmedien Wiesbaden, 2017. ISBN: 978-3-658-18056-0. DOI: `10.1007/978-3-658-18057-7`.

[HBG14] Ekbert Hering, Klaus Bressler, and Jürgen Gutekunst. *Elektronik Für Ingenieure Und Naturwissenschaftler.* Springer-Lehrbuch. Berlin, Heidelberg: Springer Berlin Heidelberg, 2014. ISBN: 978-3-642-05498-3. DOI: `10.1007/978-3-642-05499-0`.

[11a] *IEC 60050 - International Electrotechnical Vocabulary - Details for IEV Number 113-05-07: "Planck Constant".* Apr. 2011. URL: `http://www.electropedia.org/iev/iev.nsf/display?openform&ievref=113-05-07` (visited on 10/31/2017).

[11b] *IEC 60050 - International Electrotechnical Vocabulary - Details for IEV Number 113-05-16: "Elementary Electric Charge".* Apr. 2011. URL: `http://www.electropedia.org/iev/iev.nsf/display?openform&ievref=113-05-16` (visited on 10/31/2017).

[87a] *IEC 60050 - International Electrotechnical Vocabulary - Details for IEV Number 845-01-14: "Wavelength".* 1987. URL: `http://www.electropedia.org/iev/iev.nsf/display?openform&ievref=845-01-14` (visited on 10/31/2017).

[87b] *IEC 60050 - International Electrotechnical Vocabulary - Details for IEV Number 845-01-22: "Spectral Luminous Efficiency (of a Monochromatic Radiation of Wavelength λ)".* 1987. URL: `http://www.electropedia.org/iev/iev.nsf/display?openform&ievref=845-01-22` (visited on 10/31/2017).

[87c] *IEC 60050 - International Electrotechnical Vocabulary - Details for IEV Number 845-01-24: "Radiant Flux".* 1987. URL: `http://www.electropedia.org/iev/iev.nsf/display?openform&ievref=845-01-24` (visited on 10/31/2017).

[87d] *IEC 60050 - International Electrotechnical Vocabulary - Details for IEV Number 845-01-25: "Luminous Flux"*. 1987. URL: `http://www.electropedia.org/iev/iev.nsf/display?openform&ievref=845-01-25` (visited on 10/31/2017).

[87e] *IEC 60050 - International Electrotechnical Vocabulary - Details for IEV Number 845-01-37: "Irradiance (at a Point of a Surface)"*. 1987. URL: `http://www.electropedia.org/iev/iev.nsf/display?openform&ievref=845-01-37` (visited on 10/31/2017).

[87f] *IEC 60050 - International Electrotechnical Vocabulary - Details for IEV Number 845-01-38: "Illuminance (at a Point of a Surface)"*. 1987. URL: `http://www.electropedia.org/iev/iev.nsf/display?openform&ievref=845-01-38` (visited on 10/31/2017).

[87g] *IEC 60050 - International Electrotechnical Vocabulary - Details for IEV Number 845-01-56: "Luminous Efficacy of Radiation"*. 1987. URL: `http://www.electropedia.org/iev/iev.nsf/display?openform&ievref=845-01-56` (visited on 10/31/2017).

[87h] *IEC 60050 - International Electrotechnical Vocabulary - Details for IEV Number 845-05-67: "Quantum Efficiency (of a Detector)"*. 1987. URL: `http://www.electropedia.org/iev/iev.nsf/display?openform&ievref=845-05-67` (visited on 11/08/2017).

[Ill+15] J. Illade-Quinteiro, V. M. Brea, P. López, and D. Cabello. "Dark Current Optimization of 4-Transistor Pixel Topologies in Standard CMOS Technologies for Time-of-Flight Sensors". In: *2015 IEEE International Symposium on Circuits and Systems (ISCAS)*. May 2015, pp. 353–356. DOI: `10.1109/ISCAS.2015.7168643`.

[Ill+14] J. Illade-Quinteiro, Victor M. Brea, P. Lopez, B. Blanco-Filgueira, D. Cabello, and G. Domenech-Asensi. "Dark Current in Standard CMOS Pinned Photodiodes for Time-of-Flight Sensors". In: IEEE, Apr. 2014, pp. 1–4. ISBN: 978-1-4799-2220-8. DOI: `10.1109/WMED.2014.6818726`.

[JHG99] Bernd Jähne, Horst Haussecker, and Peter Geissler, eds. *Handbook of Computer Vision and Applications: Sensors and Imaging*. Vol. 1. 3 vols. Academic Press, 1999. 670 pp. ISBN: 0-12-379771-3.

[Jai16] U. Jain. "Characterization of CMOS Image Sensor". Delft, Netherlands: Faculty of Electrical Engineering, Mathematics and Computer Science, Delft University of Technology, 2016. URL: `http://resolver.tudelft.nl/uuid:5ea21702-d6fb-484c-8fbf-15c5b8563ff1` (visited on 11/07/2017).

[Jan07] James R. Janesick. *Photon Transfer DN to [Lambda]*. Vol. PM170. SPIE Press, Aug. 14, 2007. 280 pp. ISBN: 978-0-8194-6722-5.

[Jon+10] A. P. P. Jongenelen, D. A. Carnegie, A. D. Payne, and A. A. Dorrington. "Maximizing Precision over Extended Unambiguous Range for TOF Range Imaging Systems". In: *IEEE Instrumentation Measurement Technology Conference Proceedings*. May 2010, pp. 1575–1580. DOI: `10.1109/IMTC.2010.5488178`.

[Jon+12] Adrian Peter Paul Jongenelen, D. G. Bailey, A. D. Payne, D. A. Carnegie, and A. A. Dorrington. "Efficient FPGA Implementation of Homodyne-Based Time-of-Flight Range Imaging". In: *Journal of Real-Time Image Processing* 7.1 (Mar. 1, 2012), pp. 21–29. ISSN: 1861-8200, 1861-8219. DOI: `10.1007/s11554-010-0173-6`.

[Kad+13] Achuta Kadambi, Refael Whyte, Ayush Bhandari, Lee Streeter, Christopher Barsi, Adrian Dorrington, and Ramesh Raskar. “Coded Time of Flight Cameras: Sparse Deconvolution to Address Multipath Interference and Recover Time Profiles”. In: *ACM Trans. Graph.* 32.6 (Nov. 2013), 167:1–167:10. ISSN: 0730-0301. DOI: `10.1145/2508363.2508428`.

[KRI06] Timo Kahlmann, Fabio Remondino, and Hilmar Ingensand. “Calibration for Increased Accuracy of the Range Imaging Camera SwissRangerTM”. In: *Proceedings of the ISPRS Com. V Symposium.* Proceedings of the ISPRS Commission V Symposium 'Image Engineering and Vision Metrology'. Vol. 36. Institute of Photogrammetry and Remote Sensing, Univ. of Technology, 2006, pp. 136–141. URL: `https://www.research-collection.ethz.ch/handle/20.500.11850/46813` (visited on 01/17/2018).

[Kas08] Werner Kast. “Wärme- und Stoffübertragung”. In: *Raumklimatechnik.* Springer, Berlin, Heidelberg, 2008, pp. 259–366. ISBN: 978-3-540-54466-1. DOI: `10.1007/978-3-540-68938-6_7`.

[Kau+04] Rolf Kaufmann, Michael Lehmann, Matthias Schweizer, Michael Richter, Peter Metzler, Graham Lang, Thierry Oggier, Nicolas Blanc, Peter Seitz, Gabriel Gruener, and Urs Zbinden. “A Time-of-Flight Line Sensor - Development and Application”. In: *Proc SPIE.* Sept. 1, 2004, pp. 192–199. ISBN: 978-0-8194-5381-5. DOI: `10.1117/12.545571`.

[KE05] Uwe Kiencke and Ralf Eger. *Messtechnik.* Berlin/Heidelberg: Springer-Verlag, 2005. ISBN: 978-3-540-24310-6. DOI: `10.1007/3-540-27504-5`.

[Kra07] Holger Kraft. “Untersuchung Und Entwicklung Integrierbarer Photomischdetektor (PMD)-Konzepte Auf Halbleiterbasis Zur Realisierung Hochauflösender 3D-Messsysteme”. University of Siegen, Oct. 4, 2007. URL: `http://dokumentix.ub.uni-siegen.de/opus/volltexte/2007/288/` (visited on 11/02/2017).

[Lan06] Robert Lange. “3D Time-of-Flight Distance Measurement with Custom Solid-State Image Sensors in CMOS/CCD-Technology”. Dissertation. University of Siegen, Nov. 13, 2006. URL: `http://dokumentix.ub.uni-siegen.de/opus/volltexte/2006/178/` (visited on 10/31/2017).

[Lan00] Michael Langford. *Basic Photography.* 7th ed. Oxford ; Boston: Elsevier LTD, Oxford, Aug. 23, 2000. 368 pp. ISBN: 978-0-240-51592-2.

[Lef+13] Damien Lefloch, Rahul Nair, Frank Lenzen, Henrik Schäfer, Lee Streeter, Michael J. Cree, Reinhard Koch, and Andreas Kolb. “Technical Foundation and Calibration Methods for Time-of-Flight Cameras”. In: *Time-of-Flight and Depth Imaging. Sensors, Algorithms, and Applications.* Lecture Notes in Computer Science. Springer, Berlin, Heidelberg, 2013, pp. 3–24. ISBN: 978-3-642-44963-5. DOI: `10.1007/978-3-642-44964-2_1`.

[LKR08] M. Lindner, A. Kolb, and T. Ringbeck. “New Insights into the Calibration of ToF-Sensors”. In: *2008 IEEE Computer Society Conference on Computer Vision and Pattern Recognition Workshops.* 2008 IEEE Computer Society Conference on Computer Vision and Pattern Recognition Workshops. June 2008, pp. 1–5. DOI: `10.1109/CVPRW.2008.4563172`.

[Lin10] Marvin Lindner. “Calibration and Real-Time Processing of Time-of-Flight Range Data”. Dissertation. University of Siegen, Dec. 9, 2010. URL: `http://dokumentix.ub.uni-siegen.de/opus/volltexte/2010/473/` (visited on 10/31/2017).

[Lin+10] Marvin Lindner, Ingo Schiller, Andreas Kolb, and Reinhard Koch. “Time-of-Flight Sensor Calibration for Accurate Range Sensing”. In: *Computer Vision and Image Understanding.* Special issue on Time-of-Flight Camera Based Computer Vision 114.12 (Dec. 1, 2010), pp. 1318–1328. ISSN: 1077-3142. DOI: `10.1016/j.cviu.2009.11.002`.

[Lua06] Xuming Luan. “Experimental Investigation of Photonic Mixer Device and Development of TOF 3D Ranging Systems Based on PMD Technology”. Dissertation. University of Siegen, Oct. 31, 2006. URL: `http://dokumentix.ub.uni-siegen.de/opus/volltexte/2006/179/` (visited on 11/02/2017).

[17a] *MathWorks.* 2017. URL: `https://mathworks.com/` (visited on 12/04/2017).

[18a] *Matlab GUI.* 2018. URL: `https://de.mathworks.com/discovery/matlab-gui.html` (visited on 01/29/2018).

[May+09] Stefan May, David Droeschel, Dirk Holz, Stefan Fuchs, Ezio Malis, Andreas Nüchter, and Joachim Hertzberg. “Three-Dimensional Mapping with Time-of-Flight Cameras”. In: *J. Field Robot.* 26 (11-12 Nov. 2009), pp. 934–965. ISSN: 1556-4959. DOI: `10.1002/rob.v26:11/12`.

[Müh14] Thomas Mühl. *Einführung in die elektrische Messtechnik.* Wiesbaden: Springer Fachmedien Wiesbaden, 2014. ISBN: 978-3-8348-0899-8. DOI: `10.1007/978-3-8348-2063-1`.

[Mur09] James Mure-Dubois. “Contributions to Image Processing Algorithms for Advanced 3D Vision Devices”. Switzerland: University of Neuchâtel, Aug. 25, 2009. URL: `http://doc.rero.ch/record/12845` (visited on 01/10/2018).

[Pay+09] Andrew D. Payne, Adrian P. P. Jongenelen, Adrian A. Dorrington, Michael J. Cree, and Dale A. Carnegie. “Multiple Frequency Range Imaging to Remove Measurement Ambiguity”. In: *Optical 3-D Measurement Techniques.* Optical 3-D Measurement Techniques. 2009. URL: `https://researchcommons.waikato.ac.nz/handle/10289/4032` (visited on 01/24/2018).

[PS11] Matteo Perenzoni and David Stoppa. “Figures of Merit for Indirect Time-of-Flight 3D Cameras: Definition and Experimental Evaluation”. In: *Remote Sensing* 3.11 (Nov. 17, 2011), pp. 2461–2472. DOI: `10.3390/rs3112461`.

[18b] *Picofamily.* 2018. URL: `http://pmdtec.com/picofamily/` (visited on 01/24/2018).

[17b] *Pixel Size and Well Capacity.* 2017. URL: `https://www.stemmer-imaging.dk/en/knowledge-base/pixel-size-and-well-capacity/` (visited on 11/09/2017).

[Pla+17] H. Plank, A. Schoenlieb, C. Ehrenhoefer, C. Steger, G. Holweg, and N. Druml. “Synchronization of Time-of-Flight 3D Sensors for Optical Communication”. In: *IEEE International Conference on Communications (ICC).* May 2017, pp. 1–6. DOI: `10.1109/ICC.2017.7996373`.

[17c] *PyCharm: Python IDE for Professional Developers by JetBrains.* 2017. URL: `https://www.jetbrains.com/pycharm/` (visited on 12/04/2017).

[Rap07] Holger Rapp. “Experimental and Theoretical Investigation of Correlating TOF-Camera Systems”. Diploma thesis. University Heidelberg, Oct. 29, 2007. DOI: `10.11588/heidok.00007666`.

[RS13] Fabio Remondino and David Stoppa, eds. *TOF Range-Imaging Cameras.* Berlin Heidelberg: Springer-Verlag, 2013. ISBN: 978-3-642-27522-7. DOI: `10.1007/978-3-642-27523-4`.

[Sch11] Mirko Schmidt. "Analysis, Modeling and Dynamic Optimization of 3D Time-of-Flight Imaging Systems". Dissertation. University Heidelberg, 2011. DOI: `10.11588/heidok.00012297`.

[Sch05] Bernd Schneider. "Der Photomischdetektor Zur Schnellen 3D-Vermessung Für Sicherheitssysteme Und Zur Informationsübertragung Im Automobil". In: (Oct. 25, 2005). URL: `http://dokumentix.ub.uni-siegen.de/opus/frontdoor.php?source_opus=43&la=en` (visited on 12/04/2017).

[Ska+16] Amund Skavhaug, Jérémie Guiochet, Erwin Schoitsch, and Friedemann Bitsch, eds. *Computer Safety, Reliability, and Security: SAFECOMP 2016 Workshops, ASSURE, DECSoS, SASSUR, and TIPS, Trondheim, Norway, September 20, 2016, Proceedings.* Programming and Software Engineering. Springer International Publishing, 2016. ISBN: 978-3-319-45479-5. DOI: `10.1007/978-3-319-45480-1`.

[Smi97] Steven W. Smith. *Scientist and Engineer's Guide to Digital Signal Processing.* San Diego, Calif: Bertrams, Dec. 31, 1997. ISBN: 978-0-9660176-3-2.

[SD15] Lee Streeter and Adrian A. Dorrington. "Simple Harmonic Error Cancellation in Time of Flight Range Imaging". In: *Optics Letters* 40.22 (Nov. 15, 2015), pp. 5391–5394. ISSN: 1539-4794. DOI: `10.1364/OL.40.005391`.

[Tem+06] W. van der Tempel, D. Van Nieuwenhove, R. Grootjans, and M. Kuijk. "An Active Demodulation Pixel Using a Current Assisted Photonic Demodulator Implemented in 0.6 μm Standard CMOS". In: *3rd IEEE International Conference on Group IV Photonics.* Sept. 2006, pp. 116–118. DOI: `10.1109/GROUP4.2006.1708184`.

[97] *The Industrial Electronics Handbook.* May 9, 1997. URL: `https://www.crcpress.com/The-Industrial-Electronics-Handbook/Irwin/p/book/9780849383434` (visited on 10/31/2017).

[Tia00] Hui Tian. "Noise Analysis in CMOS Image Sensors". Dissertation. Stanford University, Aug. 2000.

[Uda14] Neetha Udayakumar. "Visible Light Imaging". In: *Imaging with Electromagnetic Spectrum.* Springer, Berlin, Heidelberg, 2014, pp. 67–86. ISBN: 978-3-642-54887-1. DOI: `10.1007/978-3-642-54888-8_5`.

[vExt] Martin van Exter. *Noise and Signal Processing - Extra Syllabus for (Third-Year) Course Signaalverwerking & Ruis.* URL: `http://molphys.leidenuniv.nl/~exter/SVR/noise.pdf` (visited on 07/01/2018).

[Vas08] Saeed V. Vaseghi. "Noise and Distortion". In: *Advanced Digital Signal Processing and Noise Reduction.* John Wiley & Sons, Ltd, 2008, pp. 35–50. ISBN: 978-0-470-74015-6. DOI: `10.1002/9780470740156.ch2`.

[Vas05] Gabriel Vasilescu. *Electronic Noise and Interfering Signals: Principles and Applications.* Signals and Communication Technology. Berlin Heidelberg: Springer-Verlag, 2005. ISBN: 978-3-540-40741-6. DOI: `10.1007/b137720`.

[You16] Carl Young. *Information Security Science: Measuring the Vulnerability to Data Compromises.* Syngress, June 23, 2016. 408 pp. ISBN: 978-0-12-809646-8.

[Zan+16] Pietro Zanuttigh, Giulio Marin, Carlo Dal Mutto, Fabio Dominio, Ludovico Minto, and Guido Maria Cortelazzo. *Time-of-Flight and Structured Light Depth Cameras: Technology and Applications.* Springer International Publishing, 2016. ISBN: 978-3-319-30971-2. DOI: `10.1007/978-3-319-30973-6`.

[Zha06] Zhigang Zhang. "Untersuchung Und Charakterisierung von PMD (Photomischdetektor)-Strukturen Und Ihren Grundschaltungen". Dissertation. University of Siegen, Oct. 10, 2006. URL: `http://dokumentix.ub.uni-siegen.de/opus/volltexte/2006/90/` (visited on 11/02/2017).

[ZZN15] Albrecht Zwick, Jochen Zwick, and Xuan Phuc Nguyen. *Signal- und Rauschanalyse mit Quellenverschiebung.* Berlin, Heidelberg: Springer Berlin Heidelberg, 2015. ISBN: 978-3-642-54037-0. DOI: `10.1007/978-3-642-54037-0`.